

The co-evolution of star-forming galaxies and their supermassive black holes across cosmic time

João Calhau



Physics

Department of Physics

Lancaster University

November 2019

A thesis submitted to Lancaster University for the degree of
Doctor of Philosophy in the Faculty of Science and Technology

Supervised by: Dr. David Sobral

Abstract

It is now generally accepted that galaxies host supermassive black holes in their centres. Observational evidence for a correlation between the supermassive black hole and the host galaxy properties are numerous, such as the relation between the mass of the black hole and the mass of the galaxy's bulge ($M_{\text{BH}}\text{-}M_{\text{bulge}}$ relation) and between the black hole mass and the velocity dispersion of a galaxy ($M_{\text{BH}}\text{-}\sigma$ relation). However, attempts at correlating the growth of galaxies (star formation rate - SFR) with the growth of their supermassive black holes (black hole accretion rate - BHAR) yield conflicting results, depending on the properties of the selected sample. Furthermore, most samples used when studying the activity of SMBHs are taken from AGN-selected populations, which may introduce biases by restricting the studies to only high luminosity/high accreting sources.

This thesis takes an alternative approach and probes the relation between the SFR and BHAR for samples of star-forming galaxies across cosmic time from $z \sim 0.4$ to $z \sim 6$. It makes use of the High Redshift Emission Line Survey (HiZELS) and the Slicing COSMOS with 4000 Lyman- α emitters (SC4K survey) to select a large sample of line-emitting star-forming galaxies (672 $\text{H}\alpha$ emitters - HAEs - at $z = 0.4\text{--}2$ for HiZELS and 3700 Lyman- α emitters - LAEs - at $z = 2\text{--}6$ for SC4K). Making use of stacking and SED fitting techniques, as well as direct source extraction by using the publicly available data in the X-rays, radio and FIR bands for the COSMOS field, this work estimates the BHARs and SFRs of star-forming galaxies and provides additional information on the SMBH/SF processes of star-forming galaxies across cosmic time.

The results show that most star-forming galaxies at $z < 2$ do not have AGN activity of note (average BHAR = $0.001 - 0.01 M_{\odot} \text{ yr}^{-1}$) with SFRs ranging from $2 M_{\odot} \text{ yr}^{-1}$ at $z = 0.4$ to $40 M_{\odot} \text{ yr}^{-1}$ at $z = 2.23$, which means HAEs grow approximately 1000 times faster than their SMBHs. This BHAR/SFR ratio shows little to no evolution with redshift and has very little dependence on galaxy mass.

$\text{Ly}\alpha$ emitters at higher redshifts ($z = 2 - 6$) are also shown to be mostly star-forming galaxies with only $\sim 6.8\%$ being detected in the X-rays. The X-ray luminosity of LAEs correlates with $\text{Ly}\alpha$ luminosity, suggesting $\text{Ly}\alpha$ acts as a tracer of black hole accretion. However this only happens for X-ray detected LAEs and most LAEs do not show this correlation. Most LAEs ($\sim 93\%$) are not detected in the X-rays, even when stacking, and have BHAR $< 0.017 M_{\odot} \text{ yr}^{-1}$. Only $\sim 3\%$ of LAEs are detected in the radio and their 1.4 GHz luminosity is consistent with AGN sources. However, no correlation with $\text{Ly}\alpha$ is found. In further contrast with the X-ray results, there are significant detections ($> 3\sigma$) when stacking in the radio while excluding direct detections, allowing for the use of radio as an additional SFR estimator. The results from radio are found to be consistent with FIR and $\text{Ly}\alpha$ results (total median SFR $\sim 7.2 M_{\odot} \text{ yr}^{-1}$).

The BHAR/SFR ratio of LAEs ($\log_{10}(\dot{M}_{\text{BH}}/\text{SFR}) < -2.7$) is comparable to that of lower redshift HAEs ($\log_{10}(\dot{M}_{\text{BH}}/\text{SFR}) = -3.3$) and sets a trend where star-forming galaxies grow approximately 1000 times faster than their SMBHs. This thesis results are therefore consistent with a scenario of co-evolution between supermassive black holes and their host galaxies.

To my Father, Mother and Sister. A long time has passed between
looking up at stars from the scaffolding in our backyard to the
completion of this thesis.

Acknowledgements

There would be no thesis, indeed no PhD, were it not for my supervisor David Sobral. The first acknowledgement must go to him, for all the help, guidance and patience he's shown throughout this endeavour. He never gave up on trying to help me improve, even when I kept getting sidetracked or lost in some self-created problem. I am particularly thankful for all the observational opportunities he provided during my PhD, including a trip to the Very Large Telescope in Chile, which remains the highlight of my short career and the fulfilling of a life-long dream. Thank you for giving this opportunity to a country-boy with no concept of what being a scientist really was. A special thanks as well to Catarina, for the bus rides to the University and for always receiving me so well whenever David and her invited me to their home.

I also wish to thank the Lancaster University's Observational Astrophysics group for accepting me for the PhD and for the great experience that was working there. I have never before felt more welcome in a research group and the good-natured fun and discussions during the many group lunches and tea-meetings helped me cementing the idea that science is fun. Thanks in particular to Professor Isobel Hook and Steven Williams for helping me settle in the University and the UK life in general, especially in first year. And of course to Drs. John Stott, Brooke Simmons and Julie Wardlow who, in conjunction with the previously mentioned Professor Hook and Dr. Sobral, put up with my antics in good fun.

Thank you as well to my PhD siblings in the office and outside of it. Sergio Santos gets a special mention for sharing the rent of a house with me and managing not to go insane in the three years it took for me to finish the PhD. He is a good friend. Also thanks to Ana Afonso,

Jorryt Matthee, Andra Stroe and Ali Khostovan, now doctors themselves, for the support, discussions and fun provided during the PhD and for letting me tag along in observation runs. Thanks to Veronica Ferreiros Lopez for all the fashion advice and support - will use the white shirt for the thesis defence. Thanks as well to Nick Amos, John Carrick and Matthew Chan for vital information brought to my attention, ridiculousness of rubber duck armies and the difference between deep learning and machine learning. Thanks also to Heather Wade for her love of puns and for being wrong on just about any twitter discussion where she did not agree with me.

I wish to further acknowledge the help of members of the HiZELS team for putting up with my inexperience and guiding me through the process of writing my first first-author paper. They are Philip Best, Ian Smail, Bret Lehmer, Chris Harrison and Alasdair Thomson. Thank you for all the advice and patience on how to turn my ramblings into text sensible people are able to read. Thanks also to Nicholas Ross and Richard Bower for the interesting discussions across several DEX meetings on the evolution of galaxies and the importance and contribution of AGN. Further thanks to Francesca Civano, Francesca Fornasini and the *Chandra* team for all the comments, suggestions and discussions and for making the X-ray data and exposure maps used in this work fully available to me.

A special thanks goes to my family, especially my father, mother and sister, for all the support they gave me, even if sometimes the songs were in poor taste or the chicken soup only had onions. You have been with me from the very beginning and that is impossible to repay. Obrigado.

I also am grateful to the Isaac Newton Telescope and the ING group in La Palma, for being there whenever I went on an observing run. The many nights spent there observing with the soundtrack of Dire Straights and the company of Joseph and the Amazing Technicolor Dream Coat were some of the best experiences of my life.

Finally, I wish to acknowledge the *Chandra*, VLA and COSMOS teams for assembling and making public the tremendous amount of data available for the COSMOS field and used in this thesis. I further wish to thank the Lancaster University for the PhD Studentship that made all of this possible.

Declaration

This thesis is my own work and no portion of the work referred to in this thesis has been submitted in support of an application for another degree or qualification at this or any other institute of learning.

The research presented in this thesis has been published in the relevant scientific journals in paper format, specifically Chapter 2, which is published in Calhau et al. (2017, MNRAS, 464, 1), and Chapters 3, 4 and 5 in Calhau et al. (2020, MNRAS, 493, 3).

*“Somewhere, something incredible is waiting to be known.
We’re made of star stuff. We are a way for the cosmos to know itself.”*

Carl Sagan

*“If people sat outside and looked at the stars each night, I’ll bet they’d
live a lot differently.”*

Bill Waterson

Contents

List of Figures	xii
1 Introduction	1
1.1 Observational techniques: Emission lines and wavelengths in this study	2
1.1.1 Hydrogen lines - $H\alpha$ and $Ly\alpha$ as selectors of star forming galaxies	2
1.1.2 X-ray emission - AGN selection and estimation of black hole accretion rates	5
1.1.3 Radio emission - AGN selection and SFR estimation	8
1.1.4 Far-infrared emission - SFR estimation	9
1.1.5 Narrow band selection of sources	9
1.1.6 Lyman Break technique	11
1.2 Galaxy formation and evolution across cosmic time	14
1.2.1 Galaxy formation in the Λ CDM Universe	14
1.2.2 The first stars	15
1.2.3 Supermassive Black Holes: origin and growth	17
1.2.3.1 Supermassive black holes as the powering engines of AGN	20
1.2.4 The black hole-host galaxy connection	22
1.2.4.1 The $M_{\bullet} - L_{\text{bulge}}$ relation	22
1.2.4.2 The $M_{\bullet} - \sigma$ relation	23
1.2.5 The regulation of galaxy growth	24
1.2.5.1 Stellar feedback	24

1.2.5.2	AGN feedback	25
1.3	The growth of galaxies and supermassive black holes across cosmic time	26
1.3.1	Cosmic Star-formation History	26
1.3.2	AGN Accretion history	28
1.4	This thesis	29
2	The growth of typical star-forming galaxies and their super massive black holes across cosmic time since $z \sim 2$	31
2.1	Introduction	33
2.2	Data and sample	36
2.2.1	Data: X-rays, radio & FIR	36
2.2.1.1	X-rays: C-COSMOS	36
2.2.1.2	Radio: VLA-COSMOS	36
2.2.1.3	Far-infrared: Herschel	36
2.2.2	The sample of H α emitters at $z = 0.4 - 2.23$	37
2.3	AGN selection	38
2.3.1	X-ray detections	38
2.3.2	Radio detections	40
2.4	Stacking analysis: \dot{M}_{BH} and SFR	42
2.4.1	Radio stacking: SFR	42
2.4.2	FIR stacking: SFRs	42
2.4.3	X-ray stacking	45
2.4.3.1	Black hole accretion rate from X-ray luminosity	49
2.5	Results	51
2.5.1	The cosmic evolution of black hole accretion rates	51
2.5.2	The dependence of \dot{M}_{BH} /SFR on stellar mass	51
2.5.3	Relative black hole-galaxy growth and its redshift evolution	53
2.6	Conclusion	56

3	The X-ray activity of typical and luminous Lyα emitters from z\sim2 to z\sim6	59
3.1	Introduction	61
3.2	Data and sample	63
3.2.1	The sample of Ly α emitters at $z = 2.2 - 5.8$	63
3.2.2	X-ray data: <i>Chandra</i> COSMOS-Legacy	64
3.3	Methodology	64
3.3.1	X-ray analysis	65
3.3.1.1	Source detection	65
3.3.1.2	Background and net count estimation	65
3.3.1.3	X-ray Flux estimation	66
3.3.1.4	Hardness ratio estimation	68
3.3.1.5	X-ray luminosity estimation	68
3.3.1.6	Black Hole Accretion Rates	69
3.3.1.7	Stacking	70
3.3.1.8	SFR contribution to the X-ray emission	71
3.4	The X-ray properties of LAEs at $2 < z < 6$	71
3.4.1	The hardness ratio of X-ray LAEs	75
3.4.2	X-ray luminosity of LAEs as a function of redshift	77
3.4.3	X-ray luminosity vs Ly α luminosity	83
3.4.4	\dot{M}_{BH} of LAEs vs \dot{M}_{BH} of HAEs	85
3.5	Conclusions	85
4	The radio activity of typical and luminous Lyα emitters from z\sim2 to z\sim6	87
4.1	Introduction	89
4.2	Radio data: 1.4 GHz and 3 GHz VLA-COSMOS	90
4.3	Methodology	91
4.3.1	Radio analysis	91
4.3.1.1	Source detection: 3 GHz	91
4.3.1.2	Source detection: 1.4 GHz	91
4.3.1.3	Background estimation	92

4.3.1.4	Radio flux and spectral index estimation	92
4.3.1.5	Radio luminosity estimation	94
4.3.1.6	Radio stacking	94
4.4	The radio properties of LAEs at $2 < z < 6$	95
4.4.1	Radio spectral index and Ly α luminosity	96
4.4.2	Radio luminosity of LAEs as a function of redshift	98
4.4.3	Radio luminosity vs Ly α luminosity	100
4.5	Conclusions	102
5	The growth of typical and luminous Lyα emitters and their supermassive black holes from $z \sim 2$ to $z \sim 6$	104
5.1	Introduction	106
5.2	Methodology	108
5.2.1	SFRs of LAEs	108
5.2.1.1	FIR SFRs and upper limits	108
5.2.1.2	Radio SFRs	109
5.2.1.3	Ly α SFRs	109
5.2.1.4	Estimating the Ly α escape fraction from EW $_0$ and radio	109
5.3	The SFRs of LAEs	110
5.3.1	FIR SFRs	110
5.3.2	Radio SFRs	110
5.3.3	Ly α SFRs	111
5.3.4	SFR comparison and Ly α escape fraction from radio SFR	111
5.4	Is there a BH-galaxy co-evolution in LAEs? AGN fractions, SFRs and BHAR/SFR	113
5.4.1	AGN fraction and its redshift evolution	115
5.4.2	The AGN fraction dependence on Ly α luminosity	115
5.4.2.1	Global AGN fraction: global rise with Ly α	115
5.4.2.2	X-ray and radio AGN fractions as a function of Ly α	117
5.4.2.3	The rise of the LAE AGN fraction with Ly α evolves with redshift	118
5.4.3	The black hole-to-galaxy growth of LAEs	119

5.5	Conclusions	120
6	Conclusion	123
6.1	The evolution of SMBH and their star-forming host galaxies since $z \sim 2$	123
6.2	The SMBH activity of star-forming galaxies from $z \sim 2$ to $z \sim 6$ - the X-ray perspective	124
6.3	The SMBH activity of star-forming galaxies from $z \sim 2$ to $z \sim 6$ - the radio perspective	125
6.4	The global perspective: Is there a SMBH-galaxy co-evolution for star forming galaxies?	125
6.5	Closing remarks and future work	126
	Appendix A Appendices	129
A.1	Public Catalogue of SC4K LAEs and Stacking tables	129
	References	135

List of Figures

1.1	Galactic SED overview	3
1.2	Example of Ly α emission	4
1.3	Direct imaging of M87's black hole	6
1.4	M87's relativistic jets	7
1.5	HiZELS filters	10
1.6	Selection criteria for Ly α emitters	12
1.7	Lyman-break technique	13
1.8	Dark matter distribution	16
1.9	CR7 galaxy	17
1.10	Possible ways for black holes to grow	19
1.11	AGN emission overview	21
1.12	The $M_{\bullet} - M_{\text{bulge}}$ and $M_{\bullet} - \sigma$ relations	23
1.13	The evolution of SFRD across cosmic time	27
1.14	The AGN accretion history	28
2.1	H α Luminosity distribution HAEs	39
2.2	Radio stacking of radio-undetected HAEs at $z=0.4, 0.8, 1.47$ and 2.2	43
2.3	FIR SED fitting for stacks of HAEs at $z=0.4, 0.8, 1.47$ and 2.2	44
2.4	X-ray stacking of HAEs at $z=0.4, 0.8, 1.47$ and 2.2	46
2.5	The evolution of BHARs from $z = 2.23$ to $z = 0.4$	50
2.6	The black hole-to-galaxy growths of HAEs vs stellar mass	52
2.7	The evolution of SFR and BHAR with stellar mass	53
2.8	The evolution of the BHAR/SFR ratio from $z = 2.23$ to $z = 0$	55

3.1	The distribution of the SC4K LAEs across the COSMOS field and the coverage of the different surveys	62
3.2	Flux comparison between this work and Civano et al. (2016)	67
3.3	The X-ray, radio and optical emission of LAEs SC4K-IA427-65884 and SC4K-IA484-268296	72
3.4	X-ray stacking of non-X-ray-detected LAEs	73
3.5	X-ray hardness ratio of LAEs as a function of Ly α luminosity and redshift	74
3.6	X-ray hardness ratio as a function of X-ray luminosity	76
3.7	The X-ray luminosity of LAEs as a function of redshift. Includes both direct detections and stacking excluding X-ray LAEs	78
3.8	The X-ray luminosity as a function of Ly α luminosity	80
3.9	The BHAR of LAEs as a function of redshift	84
4.1	Flux comparison between the initial radio fluxes in this study and those of Smolčić et al. (2017)	93
4.2	Radio stacking of non-radio-detected LAEs	95
4.3	The radio spectral index as a function of Ly α luminosity	97
4.4	The radio luminosity of LAEs as a function of redshift	99
4.5	The radio luminosity of LAEs as a function of Ly α luminosity	101
5.1	The SFRs of LAEs vs their BHARs	112
5.2	The LAE AGN fraction as a function of Ly α luminosity	114

Relevant Publications by the Author

First author papers

- “The growth of typical star-forming galaxies and their super massive black holes across cosmic time since $z \sim 2$ ”; **Calhau, J.**, Sobral, D., Stroe, A., Best, P., Smail, I., Lehmer, B., Harrison, C., Thomson, A. **2017, MNRAS, 464, 1.**
- “The X-ray and radio activity of typical and luminous Ly α emitters from $z \sim 2$ to $z \sim 6$: evidence for a diverse, evolving population”; **Calhau, J.**, Sobral, D., Santos, S., Matthee, J., Paulino-Afonso, A., Stroe, A., Simmons, B., Barlow-Hall, C. **2019, MNRAS, submitted, arXiv:1909.11672.**

Contributing author

- “CF-HiZELS, an ~ 10 deg² emission-line survey with spectroscopic follow-up: H α , [O III] + H β and [O II] luminosity functions at $z = 0.8, 1.4$ and 2.2 ”; Sobral, D., Matthee, J., N. Best, P., Smail, I., A. Khostovan, A., Milvang-Jensen, B., Kim, J., Stott, J., **Calhau, J.**, Nayyeri, H., Mobasher, B. **2015, MNRAS, 451, 3.**
- “The most luminous H α emitters at $z \sim 0.8-2.23$ from HiZELS: evolution of AGN and star-forming galaxies”; Sobral, D., Kohn, S.A., Best, P.N., Smail, I., Harrison, C.M., Stott, **J.**, **Calhau, J.**, Matthee, J. **2016, MNRAS, 457, 2.**
- “The nature of H-alpha star-forming galaxies at $z \sim 0.4$ in and around Cl 0939+4713: the environment matters”; Sobral, D., Stroe, A., Koyama, Y., Darvish, B., **Calhau, J.**, Afonso, A., Kodama, T., Nakata, F. **2016, MNRAS, 458, 4.**

- “A large H α survey of star formation in relaxed and merging galaxy cluster environments at $z \sim 0.15-0.3$ ”; Stroe, A., Sobral, D., Afonso, A., Alegre, L., **Calhau, J.**, Da Graça Santos, S., Weeren, R.v. **2017, MNRAS, 465, 3.**
- “Stellar Dynamics and Star Formation Histories of z similar to 1 Radio-loud Galaxies”; Barisic, I., van der Wel, A., Bezanson, R., Pacifici, C., Noeske, K., Munoz-Mateos, J.C., Franx, M., Smolcic, V., Bell, E.F., Brammer, G., **Calhau, J.**, Chauke, P., van Dokkum, P.G., van Houdt, J., Gallazzi, A., Labbe, I., Maseda, M.V., Muzzin, A., Sobral, D., Straatman, C., Wu, P. **2017, ApJ, 847, 1.**
- “A 1.4 deg² blind survey for CII], CIII] and CIV at $z \sim 0.7-1.5$. I: Nature, morphologies and equivalent widths”; Stroe, A., Sobral, D., Matthee, J., **Calhau, J.**, Oteo, I. **2017, MNRAS, 471, 3.**
- “A 1.4 deg² blind survey for C II], C III] and C IV at $z \sim 0.7-1.5$: II. Luminosity functions and cosmic average line ratios”; Stroe, A., Sobral, D., Matthee, J., **Calhau, J.**, Oteo, I. **2017, MNRAS, 471, 3.**
- “Stellar Populations of over 1000 $z \sim 0.8$ Galaxies from LEGA-C: Ages and Star Formation Histories from Dn 4000 and H δ ”; Wu, P., Wel, A.v.d., Gallazzi, A., Bezanson, R., Pacifici, C., Straatman, C., Franx, M., Barišić, I., Bell, E.F., Brammer, G.B., **Calhau, J.**, Chauke, P., Houdt, J.v., Maseda, M.V., Muzzin, A., Rix, H., Sobral, D., Spilker, J., Sande, J.v.d., Dokkum, P.v., Wild, V. **2018, ApJ, 855, 2.**
- “Spatially Resolved Stellar Kinematics from LEGA-C: Increased Rotational Support in $z \sim 0.8$ Quiescent Galaxies”; Bezanson, R., Wel, A.v.d., Pacifici, C., Noeske, K., Barišić, I., Bell, E.F., Brammer, G.B., **Calhau, J.**, Chauke, P., Dokkum, P.v., Franx, M., Gallazzi, A., Houdt, J.v., Labbé, I., Maseda, M.V., Muñoz-Mateos, J.C., Muzzin, A., Sande, J.v.d., Sobral, D., Straatman, C., Wu, P. **2018, ApJ, 858, 1.**
- “Slicing COSMOS with SC4K: the evolution of typical Ly α emitters and the Ly α escape fraction from $z \sim 2$ to $z \sim 6$ ”; Sobral, D., Da Graça Santos,

S., Matthee, J., Paulino-Afonso, A., Ribeiro, B., **Calhau, J.**, Khostovan, A.A. **2018, MNRAS, 476, 4.**

- “On the UV compactness and morphologies of typical Lyman- α emitters from $z \sim 2$ to $z \sim 6$ ”; Paulino-Afonso, A., Sobral, D., Ribeiro, B., Matthee, J., Da Graça Santos, S., **Calhau, J.**, Forshaw, A., Johnson, A., Merrick, J., Perez, S., Sheldon, O. **2018, MNRAS, 476, 4.**
- “Star formation histories of $z \sim 1$ galaxies in LEGA-C”; Chauke, P., Wel, A.v.d., Pacifici, C., Bezanson, R., Wu, P., Gallazzi, A., Noeske, K., Straatman, C., Munoz-Mateos, J.C., Franx, M., Barisic, I., Bell, E.F., Brammer, G., **Calhau, J.**, Houdt, J.v., Labbé, I., Maseda, M.V., Muzzin, A., Rix, H., Sobral, D. **2018, ApJ, 861, 1.**
- “The Large Early Galaxy Astrophysics Census (LEGA-C) Data Release II: dynamical and stellar population properties of $z \lesssim 1$ Galaxies in the Cosmos field; Straatman, C.M.S., Wel, A.v.d., Bezanson, R., Pacifici, C., Gallazzi, A., Wu, P., Noeske, K., Barisic, I., Bell, E.F., Brammer, G.B., **Calhau, J.**, Chauke, P., Franx, M., Houdt, J.v., Labbe, I., Maseda, M.V., Munoz-Mateos, J.C., Muzzin, A., Sande, J.v.d., Sobral, D., Spilker, J.S. **2018, ApJ, 239, 2.**
- “The evolution of rest-frame UV properties, Ly α EWs and the SFR-Stellar mass relation at $z \sim 2 - 6$ for SC4K LAEs”, Santos, S.; Sobral, D.; Matthee, J.; **Calhau, J.**; da Cunha, E.; Ribeiro, B.; Paulino-Afonso, A.; Arrabal Haro, P.; Butterworth, J., **2019, MNRAS, submitted, arXiv:1910.02959.**

Chapter 1

Introduction

Astronomy, and later its more encompassing sibling astrophysics, has always been closely related with the growth of humanity, be it from the study of planetary and solar cycles - as well as seasons - to improve plantations and crops, to the use of stars as guiding lights while exploring the world. But beyond the purely practical aspect that drove our initial foray into the study of the Universe, there is the simpler and no less strong desire to simply know *why* and *how*. *How did we get here?*

Our current understanding of our place in the Universe is much different than what we started with. We now know that the Earth does not stand at the centre of the Universe and is not even, in fact, the centre of the Solar System. Instead, we know that our planet and the Sun are part of a much larger collection of stars and other components, such as gas and dust, that have come together in some point in the past to form a giant structure which we call the Milky Way - a galaxy. But the answer to that all consuming question from before still eludes us and to properly understand the creation and the evolution of the Universe - how we got here -, an understanding of the formation and evolution of galaxies is also required.

1.1 Observational techniques: Emission lines and wavelengths in this study

Astronomers are a fortunate kind of researcher in that the laboratory in which we conduct our experiments is the entirety of the Universe, where there is no restriction in the energy used for the experiments or the scale of those experiments. Unfortunately, the drawbacks to that are the distances and timescales involved, which render it impossible for an Astrophysicist to go and directly observe the physical processes in study. We are therefore limited to what we can infer and deduce from the light that reaches us from the objects we study. In Figure 1.1 we show the different wavelengths and lines used in our study, which we expand upon in the coming sections.

1.1.1 Hydrogen lines - $H\alpha$ and $Ly\alpha$ as selectors of star forming galaxies

Hydrogen- α emission ($H\alpha$, $\lambda_0 = 6563 \text{ \AA}$) is part of the Balmer series for Hydrogen, specifically occurring when an electron transitions from the third to second energy levels. It is one of the brightest Hydrogen lines and, up to redshift $z \sim 2 - 3$, is located in the visible range of the electromagnetic spectrum (Sobral et al., 2013). $H\alpha$ is sensitive to massive ($> 8 M_\odot$), very short-lived stars (Kennicutt, 1998). It is also a well-calibrated line with limited dust attenuation (although other lines, such as the Paschen series are even less affected by dust extinction, they are much fainter than the $H\alpha$ line, making it difficult to use them in higher redshift surveys), making it a great line for tracing instantaneous star formation (SF) in galaxies (Garn et al., 2010; Geach et al., 2008; Sobral et al., 2013).

For $z > 2.5$, the $H\alpha$ line shifts to the infrared and becomes impossible to observe from ground based telescopes (although some studies maintain that it might be possible to extend the use of the $H\alpha$ line up to $z \sim 4$ through the use of space telescopes such as *Spitzer* and *JWST*, see e.g. Shim et al., 2011). However, at these redshifts a new line becomes available. Lyman- α ($Ly\alpha$, $\lambda_0 = 1216 \text{ \AA}$) is the strongest emission line in the optical and ultraviolet (UV) (rest-frame, see

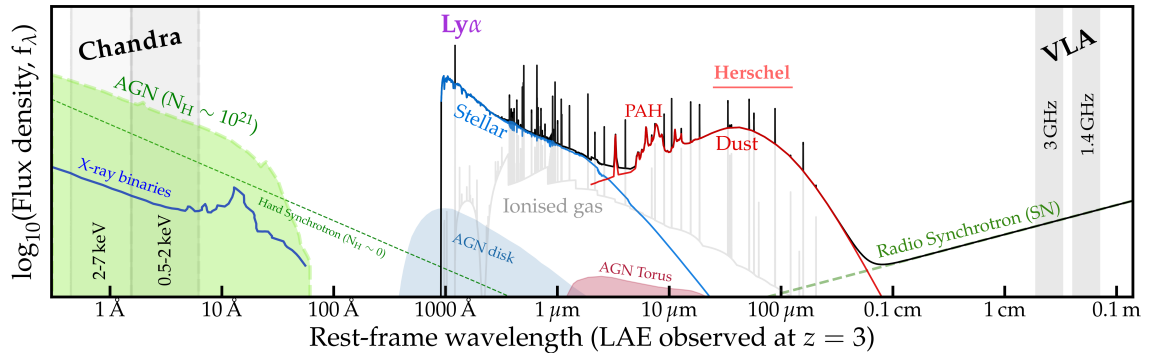


Figure 1.1: An overview of the data used in this study and the mechanisms that originated emission in star-forming galaxies/active galactic nuclei, from X-rays to the radio. From left (lower wavelength) to right (higher wavelength) the plot shows the bandwidth covered by *Chandra*, divided in its hard (2-7 keV) and soft (0.5-2 keV) bands, as well as the expected SED for an active galactic nucleus (AGN) emitting in the X-rays through a column density of $N_H \sim 10^{21} \text{ cm}^{-2}$ (see Hickox & Alexander, 2018) and the contribution of X-ray binaries. A hard X-ray power law is also shown, illustrating the shape of the X-ray SED in the complete absence of absorption. The blue outline identifies the stellar component of the galactic spectra, which includes emission lines such as $H\alpha$ and $\text{Ly}\alpha$, used to select star-forming galaxies. The blue and red shades illustrate the contribution from the different AGN components. The red outline shows the contribution of dust, heated by nearby stars and identified in infrared telescopes like *Herschel* in the form of far-infrared (FIR) radiation. Finally, the power law of radio emission, from synchrotron radiation born in relativistic jets of AGN and supernovae remnants (tracing star formation - SF) is shown, as well as the wavelengths covered by the National Radio Astronomy Observatory’s Very Large Array (VLA) in the surveys used here.

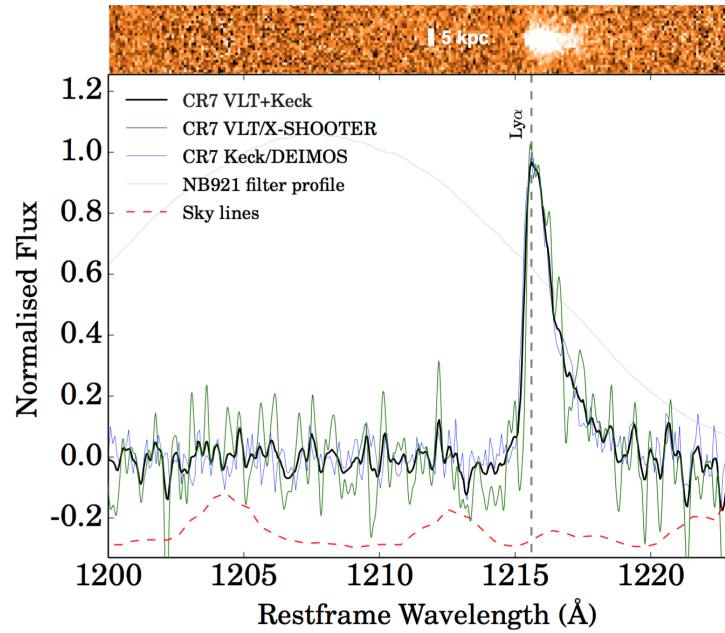


Figure 1.2: The 2D and 1D spectra of the Ly α emission in CR7 (from Sobral et al., 2015). The filter used for this observation has relatively low transmission (50% peak transmission) illustrating Ly α 's clear strength and distinct line profile.

e.g. Pritchett, 1994) and is expected to be emitted by both star-forming galaxies and active galactic nuclei (AGN). On the sources of emission, see e.g. Cowie & Hu, 1998; Ono et al., 2012; Sobral & Matthee, 2019; Sobral et al., 2017). The line is shifted into the optical band at $2 < z < 7$ which, in conjunction with its intrinsic luminosity and characteristic shape (see Figure 1.2), makes it easy to observe with ground-based telescopes.

1.1.2 X-ray emission - AGN selection and estimation of black hole accretion rates

X-rays are particularly important in identifying and characterising AGN activity. AGN are generally much brighter in the X-rays than stars, making them easy to identify. Although star-forming-associated processes (like supernovae explosions) also produce X-ray emission (for example through X-ray Massive Binaries), the luminosities achieved by these processes are usually much lower than the average AGN. Empirical relations have found that typical star formation rates (SFR) of $\sim 5 M_{\odot} \text{ yr}^{-1}$ at $z = 2$ produce an X-ray luminosity of $\sim 10^{41} \text{ erg s}^{-1}$, at least 2 orders of magnitude below the luminosity of the fainter AGN detected by *Chandra* at the same redshift (see Lehmer et al., 2016, and Chapter 3.4).

X-rays have high penetrating power and normal column densities do not reduce the flux of X-ray photons significantly, especially in the hard band ($> 2 \text{ keV}$, see Figure 1.1). They are often produced in the hot corona of the accretion disk through the inverse Compton effect.

The Compton effect is the change of direction of an electron, or another charged particle, due to an energy transfer from a photon. It was discovered by Arthur Compton (Compton, 1923) and is also called Compton scattering.

The photon transfers part of its energy to the charged particle, changing its velocity vector, and a new photon is emitted with the remaining energy in a different direction than the original.

The Compton effect is important in that it is evidence of the dual (particle-wave) nature of light and Compton himself derived the mathematical formula for the process:

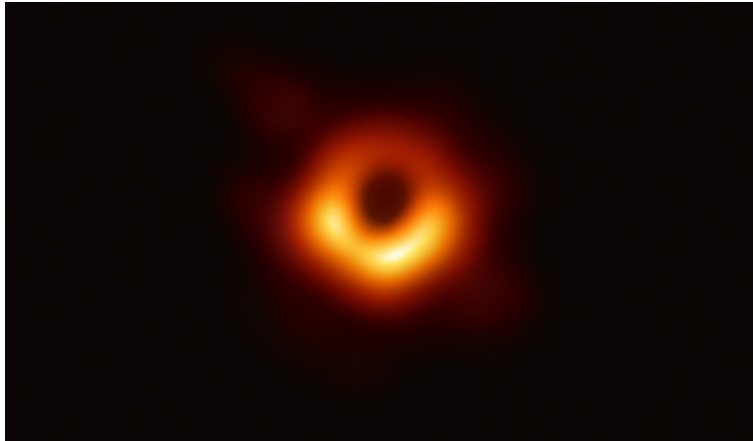


Figure 1.3: The first direct imaging of a supermassive black hole’s accretion disk on the galaxy M87, taken in the radio band at $\lambda = 1.3\text{mm}$ (Event Horizon Telescope Collaboration et al., 2019). X-ray emission is produced through inverse Compton scattering on the hot corona of the accretion disk, directly correlating X-ray luminosity and accretion rate.

$$\lambda' - \lambda = \frac{h}{m_e c} (1 - \cos\theta)$$

where $\frac{h}{m_e c}$ is known as the Compton wavelength ($2.43 \times 10^{-12}\text{ m}$, h is the planck constant, m_e is the electron mass and c is the speed of light).

Compton scattering occurs for X-ray or gamma ray photons and can also occur in the reverse order, where a charged particle transfers energy onto a photon. In Astronomy, it is observed in the photons of the Cosmic Microwave Background (CMB) and also, and of particular interest to us, in the accretion disk of an accreting black hole, where the charged particles in the hot corona of an accretion disk emit X-ray photons through the inverse Compton effect.

X-rays correlate directly to the accretion process, probing the immediate vicinity of the supermassive black hole (SMBH) and it is possible to estimate the accretion rate of a black hole based on its X-ray luminosity and some assumptions regarding the efficiency of the accretion (see Haardt & Maraschi, 1991, and Chapter 3.3.1.6).

In this work we use X-rays both as a probe for the presence of AGN in our star-forming samples of galaxies and as a means to estimate the black hole activity

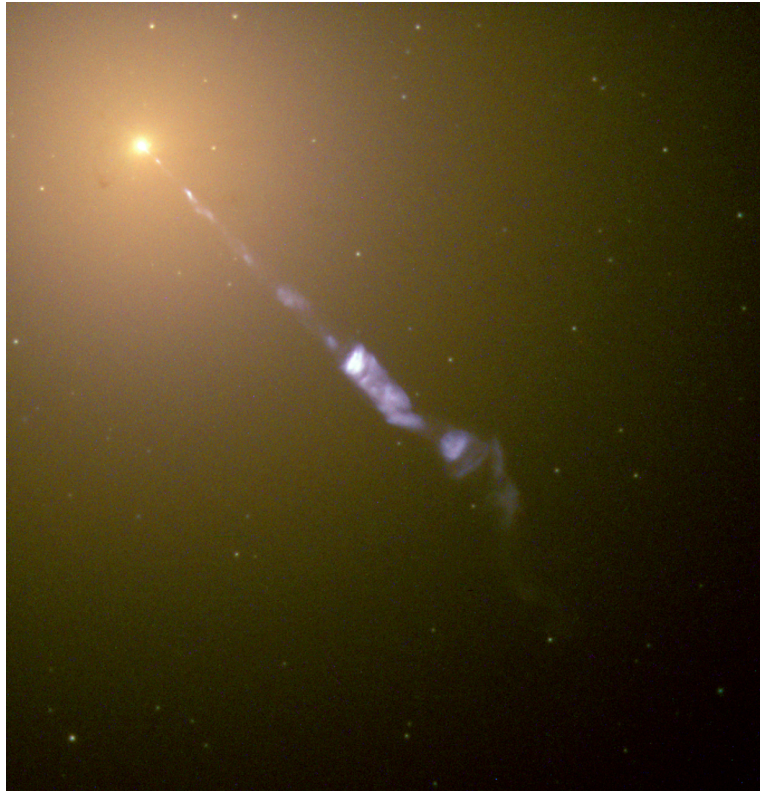


Figure 1.4: A picture of M87 and one of its relativistic jets (composite image of the UV, optical and infrared bands). Charged particles are accelerated through the magnetic field of the supermassive black hole and release photons in a wide range of wavelengths through synchrotron radiation, including the radio. Credit: NASA and The Hubble Heritage Team (STScI/AURA).

of both the directly detected AGN and the typical star-forming galaxy.

1.1.3 Radio emission - AGN selection and SFR estimation

Radio emission from galaxies can have a number of origins. It is often found, for example, in shock fronts from mergers in giant galaxy clusters (radio relics, see Stroe et al., 2013). It can also originate through synchrotron radiation from the activity of AGN (in relativistic jets) and star formation (in supernovae remnants of massive short-lived stars).

Synchrotron radiation is similar to Compton radiation in the sense that they both result from the change in the direction, or velocity vector, of a charged particle. However, Synchrotron radiation differs in that the particles change their velocity due to perpendicular acceleration in the presence of strong magnetic fields. It is characterised by its characteristic polarisation and can be emitted in a broad range of the electromagnetic spectrum, from radio and microwaves to X-rays.

Synchrotron radiation was discovered in 1946 in a synchrotron accelerator (Elder et al., 1947) but it has also been detected in naturally occurring sources, such as pulsar wind nebulae. Supermassive black holes can also emit this kind of radiation through their relativistic jets, where strong magnetic fields accelerate charged particles to relativistic speeds. Its first detection in Nature was made in one of these jets, hailing from Messier 87 (Burbidge, 1956, see Figure 1.4).

Radio luminosity can be used to select AGN similarly to X-rays. It is generally accepted that if a source has a radio luminosity higher than $10^{23} \text{ W Hz}^{-1}$ in the 1.4 GHz band, it is likely to be an AGN (Meurs & Wilson, 1984, although the separation between star-forming processes and AGN is not a clear one - see also Chapter 4.4.2).

Unlike X-rays, radio traces a larger timescale of the SMBH activity and, as such, cannot be used as a tracer of the black hole's accretion rate. Nevertheless, several useful quantities can be derived from radio emission, such as the spectral index α , which can give information on the age of the AGN or the density of the environment (e.g. Athreya & Kapahi, 1998; Khostovan et al., 2019). It can also be used as a relatively independent estimator for the SFR (see, e.g. Yun et al.,

2001), provided the AGN contaminants are retracted from the sample, although we stress that the lack of radio-detected AGN in a sample does not mean there is no contamination from lower luminosity AGN.

1.1.4 Far-infrared emission - SFR estimation

The far-infrared (FIR) can be used as a tracer of obscured star formation, as well as the amount of obscuration in a galaxy. This is due to the fact that ultraviolet and optical photons, emitted by massive stars, are absorbed by the surrounding environment (e.g. dust) and re-emitted in the far-infrared band (Heinis et al., 2013; Lacki et al., 2010). The SFRs estimated from the far-infrared include heavily obscured star formation and the contribution of old stellar populations (Salim et al., 2009).

It is necessary to make sure that there is no AGN contamination when calculating the FIR luminosities used in the estimation of SFRs. FIR emission from cold dust (rest frame $> 40\mu\text{m}$, see e.g. Netzer et al., 2007) should be free of such contamination but, as we progress towards higher redshift extra care should be taken (at redshifts $z > 3$, the $100\mu\text{m}$ band probes the $25\mu\text{m}$ rest-frame, which might be partially contaminated by AGN activity).

1.1.5 Narrow band selection of sources

In order to identify the line emitters, a similar technique was employed for both $\text{H}\alpha$ and $\text{Ly}\alpha$ emitters (HAE and LAE, respectively), at its core consisting of excess flux selection. The targets are imaged with broad band (BB) filters matching narrow band (NB) filters (NB921, NBH NBJ and NBK - see Figure 1.5), in the case of $\text{H}\alpha$ or medium band (MB) filters (e.g. IA464 and IA427), in the case of $\text{Ly}\alpha$ - although NB filters (NB391) were also used for LAEs in this work. For simplicity, we briefly describe the procedure using NB filters, although it should be noted that the procedure is the same when using BB and MB filters.

Potential line emitters are selected according to the significance of the narrow(er)-band excess. True emitters will have $(\text{BB} - \text{NB}) > \Sigma$, where Σ quantifies the excess compared to the random scatter expected of a source with zero colour (see

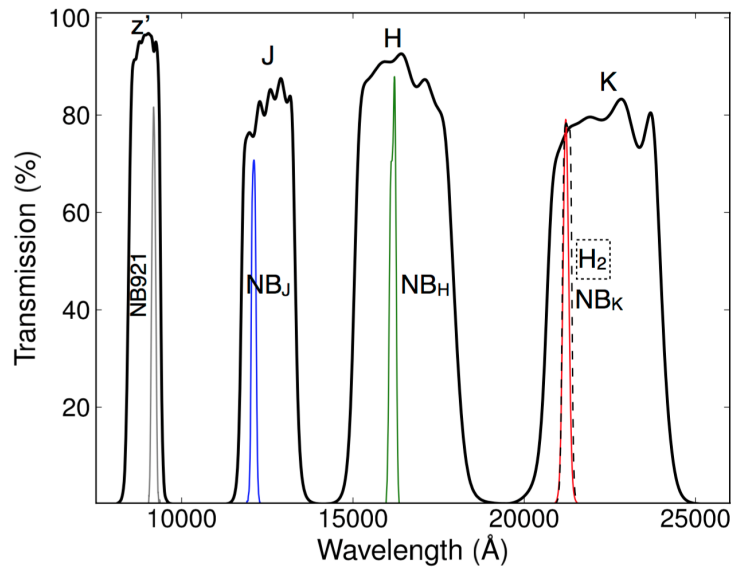


Figure 1.5: The profiles of the broad and narrow band (NB) filters used to trace the redshifted $H\alpha$ line at $z = 0.4, 0.84, 1.47$ and 2.23 in the HiZELS survey (taken from Sobral et al., 2013). The broad band (BB) filters are used to estimate and remove continuum contribution. Because the filters are not necessarily located at the centre of the broad band transmission profile, very blue or red sources may mimic line emitters, introducing the need to correct the NB magnitudes using the BB.

e.g., Bunker et al., 1995; Sobral et al., 2013). The NB magnitudes are corrected with the BB magnitudes in order to ensure that sources with no line emission present $BB - NB \approx 0$, regardless of their continuum color. Otherwise sources with strong blue or red colours could mimic line emitters and contaminate the selection. The excess in colour is defined as

$$\Sigma = \frac{1 - 10^{-0.4(BB-NB)}}{10^{-0.4(ZP-NB)} \sqrt{\text{rms}_{\text{NB}}^2 + \text{rms}_{\text{BB}}^2}} \quad (1.1)$$

where BB and NB are the broad and narrow band magnitudes and ZP is the zero-point of the image (corrections to NB and BB ensure that the ZP is the same for both bands). Sources are considered potential line emitters if $\Sigma > 3$ (see Figure 1.6).

In order to void contamination from other line emitters, the equivalent width (EW) of the line is also measured, with

$$\text{EW} = \Delta\lambda_{\text{NB}} \frac{f_{\text{NB}} - f_{\text{BB}}}{f_{\text{BB}} - f_{\text{NB}} (\Delta\lambda_{\text{NB}} / \Delta\lambda_{\text{BB}})} \quad (1.2)$$

where $\Delta\lambda_{\text{NB}}$ and $\Delta\lambda_{\text{BB}}$ are the full width half-maximums of the narrow and broad band filters and f_{NB} and f_{BB} are the flux densities in the respective bands. To avoid contamination, a limit on the rest-frame EW is applied. For $\text{H}\alpha$ emitters the cut occurs at the common value of $\text{EW}_0 = 25\text{\AA}$ (see, e.g. Ouchi et al., 2008; Sobral et al., 2013). However, because LAE selection makes use of several wider, medium band filters, a stricter cut of $\text{EW} > 50\text{\AA}$ is applied to all medium bands.

1.1.6 Lyman Break technique

The Lyman break is a physical feature that arises in the spectra of galaxies due to the fact that radiation at energies higher than the Lyman limit (the energy required for an electron to free itself from an Hydrogen in the ground state - corresponding to a rest-frame wavelength of $\lambda \sim 912\text{\AA}$) tends to be completely absorbed by the interstellar and intergalactic medium. A galaxy with a Lyman break effectively is “bright” at wavelengths longer than 912\AA and “dim” at shorter wavelengths. Due to redshift, this break shifts from the UV to the optical and

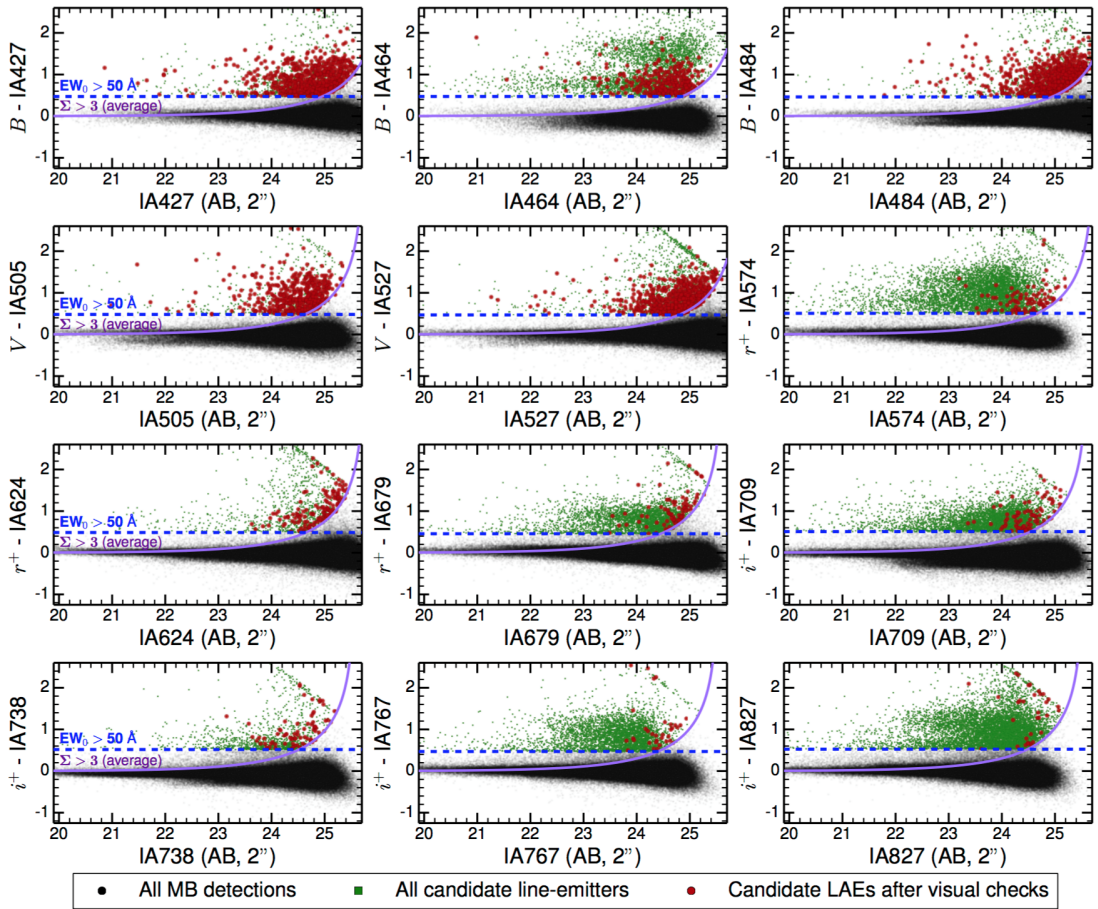


Figure 1.6: The colour-magnitude diagrams used for selecting the line-emitters in SC4K for the medium bands (taken from Sobral et al., 2018a). Sources with high enough EW ($EW > 50\text{\AA}$ for LAEs, 25\AA for HAEs) and with a significant excess ($\Sigma > 3$) are selected as line emitters.

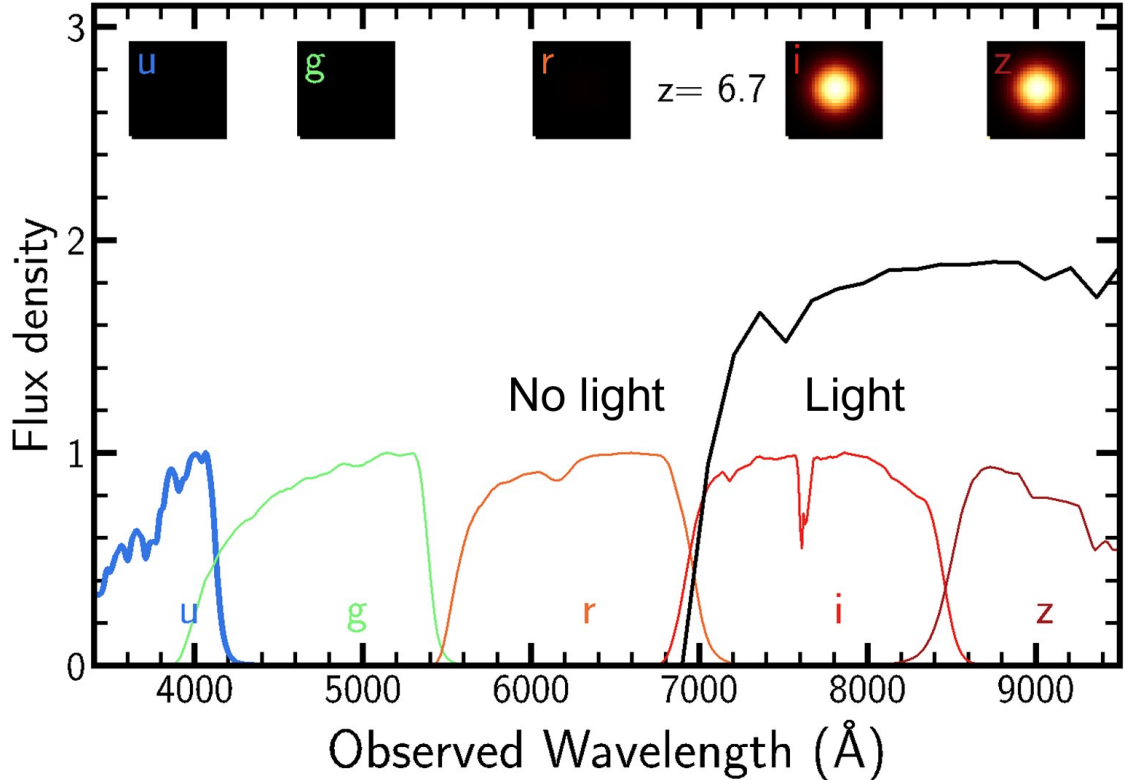


Figure 1.7: Example of the Lyman break technique detecting a galaxy at redshift $z \sim 6.7$ (credit to David Sobral, Heather Wade and the XGAL team). The galaxy is detected on the redder filters (longer wavelength than the target wavelength expected of the Lyman break at that redshift) but not on the bluer filters (shorter wavelength).

infrared bands, making it possible to use it in order to select galaxies at redshifts of $z = 2 - 5$ and higher (see Figure 1.7).

The Lyman break technique effectively makes use of a set of filters centred around the expected wavelength of the break at a target redshift. A “Lyman-break galaxy” will thus be detected in filters that are redder (have longer wavelengths) than the target wavelength and be undetected in the bluer filters (with shorter wavelengths). For this study and the SC4K survey, this amounts to making a colour selection identifying a colour break blueward of the medium band with excess emission (see Section 1.1.5) with no significant detection bluer than that particular filter (see Sobral et al., 2018a, for details on the colour criteria for each filter).

As an added security measure, sources with red colours are also identified and excluded via colour selection (e.g. $B - r > 0.5$ for $z \sim 2.5$, where B and r are the magnitudes for each respective filter. See Sobral et al., 2018a, for the cuts applied to each redshift), in order to avoid contamination by stars or red galaxies with a strong Balmer break ($\lambda \sim 4000\text{\AA}$) which may mimic the Lyman break (see, e.g, Matthee et al., 2014).

1.2 Galaxy formation and evolution across cosmic time

A galaxy can be defined as a system of gas, dust and stars (i.e. baryonic matter) gravitationally bound within a halo of dark matter. The big problem with trying to understand the formation and evolution of these objects is that even the shortest timescales involved are much larger than the average human lifetime. However we can take "snapshots" of galaxies at different times in their lives and try to assemble galaxy evolution that way. This is possible because the speed of light is finite and because of that, the farthest a galaxy is when we observe it, the more into the past we are peering. Comparing the properties of galaxies at different distances therefore equals to comparing those properties at different times of a galaxy's evolution.

1.2.1 Galaxy formation in the Λ CDM Universe

Currently, Cosmology divides the Universe into three main components: baryonic matter (protons, neutrons, the regular matter of our day-to-day lives), dark matter and dark energy (Hildebrandt et al., 2017). Different cosmological models differ in both the nature and abundance of these components. Modern Cosmology specifies the large-scale geometry of the Universe but it also predicts its thermal history and matter content. This is important because the formation of galaxies depends on the content of the Universe, and since we observe galaxies across redshift ranges, i.e. across cosmic time, Cosmology becomes necessary in understanding galaxy evolution.

In the most accepted cosmological model, the energy density of the Universe is $\sim 68.5\%$ due to a cosmological constant (λ) and $\sim 31.5\%$ due to matter (which includes both cold dark matter (CDM) and baryonic matter, that makes up the "visible" Universe - Planck Collaboration et al., 2018). We call this model the λ CDM model.

Classical Cosmology breaks down near singularities, be those of black holes or of the very dense environment of the early Universe. In order to explore these situations, we must incorporate quantum physics into our models. The inclusion of quantum processes in cosmology shows the existence of fluctuations in the vacuum energy of the early Universe's that translate into density perturbations. These density perturbations are the cradle of the Universe's first galaxies. As time progresses these perturbations grow in size and intensity, with slightly denser regions becoming even more over-dense, while less denser regions become even emptier. In λ CDM cosmology each perturbation encases both baryonic and dark matter. As a perturbation grows, it eventually collapses and the dark matter relaxes into a dark matter halo, while the baryonic matter settles at the centre of the halo's potential well. Small dark matter haloes then further merge with each other to form larger structures (Conselice, 2014; Somerville & Davé, 2015).

The baryonic gas then undergoes cooling, which can happen following a variety of processes: electron recombination, radioactive decay and at high redshifts ($z \geq 6$) inverse Compton effect. Cooling is generally more effective in higher density regions because most of the cooling processes require multiple particles to take place. With the effects of cooling, the baryonic matter separates from the dark matter and pools at the centre of the dark matter halo, forming a protogalaxy.

1.2.2 The first stars

The contraction of baryonic matter (hereafter referred simply as "gas") causes baryonic gravity to eventually supersede dark matter gravity. The gas then starts collapsing under its own gravity, which increases both the density and the temperature of the gas, eventually causing the fragmentation of the collapsing gas

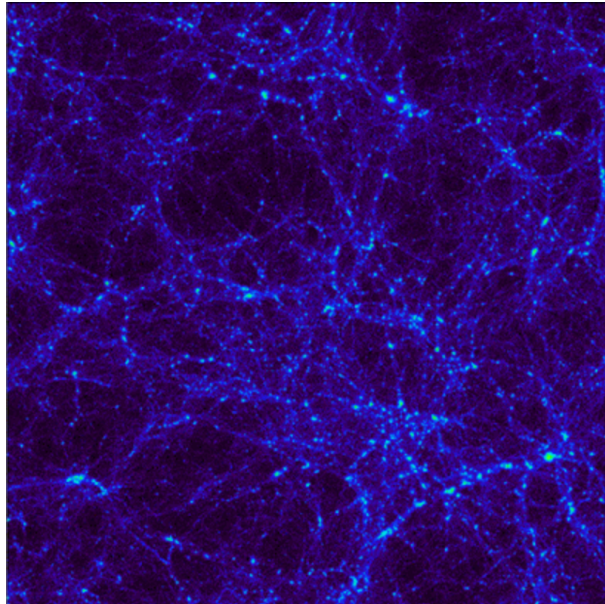


Figure 1.8: The distribution of dark matter in the Universe as obtained by numerical simulations. The brighter clumps in the dark matter network represent the dark matter haloes within which galaxies are hosted. Copyright: The Virgo Consortium/Alexandre Amblard/ESA

cloud into smaller, high density clumps. These clumps eventually coalesce into the first stars (see e.g. Abel et al., 2000; White & Rees, 1978).

These first generation of stars, known as population III stars, are believed to have been composed exclusively of Hydrogen and Helium, pristine gas, without heavier elements (Ostriker & Gnedin, 1996). Simulations of the collapse of primordial gas clouds suggest these stars were very massive (100 to 1000 M_{\odot} , see e.g. Larson, 1999; Nakamura & Umemura, 2000). These stars would, upon their death, be responsible for the chemical enrichment of the environment, although there is evidence that higher mass stars would simply collapse directly into black holes and that the formation of heavy elements was due to stars of $< 260 M_{\odot}$ (Fryer et al., 2001).

Empirical data generally causes us to separate star formation processes into two different modes: quiescent star formation and starbursts. Quiescent star formation occurs naturally from existing molecular gas clouds. Starbursts require large amounts of gas and are characterised by particularly high SFRs condensed



Figure 1.9: The galaxy CR7 (COSMOS Redshift 7, see Sobral et al., 2015), the brightest galaxy discovered in the early Universe and believed to host first generations stars (population III) within it. Artist's impression. Credit: ESO/M. Kommesser.

in relatively small regions. They are generally triggered by dynamical interactions and instabilities, such as galaxy mergers, which would have been expected by the hierarchical galaxy formation of the λ -CDM cosmology (Barnes, 2004; Kim et al., 2009; Schweizer, 2009).

However, the physics behind these processes is still unclear, and many open questions remain unanswered, such as: What fraction of stars is formed by quiescent processes? Do quiescent processes and starbursts produce the same initial mass function (IMF)? How exactly does cold gas transform into stars? How is chemical enrichment processed? To make matters worse, cosmological simulations are generally unable to resolve the scales of molecular gas clouds responsible for star formation and generally restrict themselves to empirical recipes to simulate star formation. Answering these questions requires a deep understanding of the star formation in galaxies and the processes that influence it across cosmic time.

1.2.3 Supermassive Black Holes: origin and growth

The formation of the first stars marks the point when the Universe becomes heterogeneous. The first stars also signal the transition from pristine primordial gas to gas that has become metal enriched, allowing for more effective ways of

cooling than available in the early Universe.

This has opened the way for several different hypotheses on how the first supermassive black holes formed. Observational evidence states that, by redshift $z \sim 7$, there were already quasars with masses of $10^9 - 10^{10} M_{\odot}$ (e.g. Bañados et al., 2018; Mortlock et al., 2012). The problem with this evidence is how to get a black hole (BH) to grow fast enough to reach such masses by those redshifts. One hypothesis is that they formed out of the collapse of massive Pop. III stars (Bromm & Loeb, 2006; Madau & Rees, 2001). These early SMBH seeds would have masses of the order of 10-100 M_{\odot} and would need to grow in time to the sizes normally associated with SMBHs ($\geq 10^6 M_{\odot}$). The problem with this scenario is that the newly formed BHs are, at least at the beginning, in low density environments, due to the solar winds from the massive stellar progenitors clearing away the surrounding gas. Therefore, in order for the early BHs to reach the masses observed in quasars at $z \sim 7$, the BH would need to undergo growth rates that exceed the Eddington rate (see Figure 1.10).

One of the solutions proposed to the growth of stellar BHs as seeds of SMBHs is the idea of a direct collapse black hole. In this case, a large cloud of primordial gas collapses quickly/strongly enough to heat up the gas and excite the Hydrogen atoms from the ground state. Normally, recombination would radiate the excess heat away, especially through atomic Ly α emission, leading to the fragmentation of the cloud and subsequent formation of stars, in which case we would be back in case one. But if the cloud is devoid of molecular Hydrogen (or at least has H₂ in sufficiently small quantities) or heavier elements and dust, it is theorised that the inefficient cooling of the cloud would prevent fragmentation and star formation, leading to the complete collapse of the gas cloud into a SMBH (Begelman et al., 2006).

The other hypothesis for the SMBH formation is that of runaway mergers in dense clusters (Devecchi & Volonteri, 2009). In this scenario, the black hole would start as a normal stellar black hole but, due to the environment in the dense cluster, merge with several other black holes and grow in mass quickly enough to bypass the need of super-Eddington accretion (or at least requiring less time in such conditions).

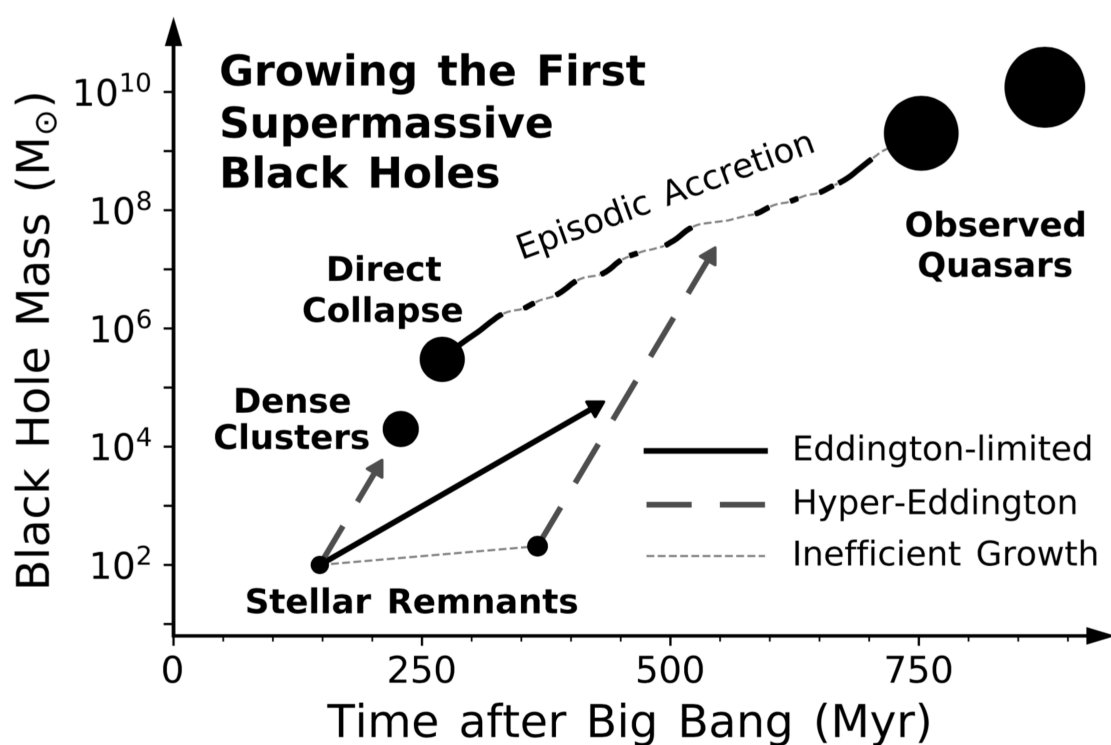


Figure 1.10: The possible seeds for SMBHs in the early Universe and their expected ways of growth in order to reach the observed quasar masses at redshift $z \sim 7$ (taken from Smith & Bromm 2019).

It is likely that the mechanism for the formation of supermassive black holes is some fusion of the three processes but our current knowledge does not allow for us to determine which, if any, is the dominant process or whether or not other processes may be involved.

1.2.3.1 Supermassive black holes as the powering engines of AGN

It is generally accepted that the majority of, if not all, galaxies host a supermassive black hole at their centre (see, e.g. Kormendy & Ho, 2013, and Section 1.2.4). In “normal” galaxies, the presence of this object remains largely unnoticed. However, it was suggested as early as 1964 (Salpeter, 1964) that if enough matter is absorbed by the black hole, the radiative processes associated with its feeding cause the central region to become significantly more luminous than the rest of the galaxy. In these cases, the galaxy is said to have an Active Galactic Nucleus.

Figure 1.11 illustrates the expected components of an AGN, starting from the central “engine“, the supermassive black hole (1). The infall of matter onto a black hole spirals towards the centre and forms an accretion disk (2). Accretion disks are observed in a variety of astrophysical systems, from AGN to protostars. The particles in the accretion disk collide amongst each other and the gravitational and frictional interactions cause the disk to heat up, leading to the emission of radiation (which, in the specific case of AGN happens in the X-ray band, through inverse Compton effect, but the wavelength at which the radiation is emitted depends on the mass of the accreting body). The radiation of energy due to friction causes the angular momentum of the interacting particles to decrease, causing matter to travel to the inner region of the disk (Gurzadian & Ozernoi, 1979). The accretion disk is surrounded by a large torus made up of dust (3), where thermal energy is radiated in the infrared.

The radiation from the accretion disk can also excite gas clouds in the vicinity of the supermassive black hole, which then radiate the extra energy in specific emission lines, giving rise to the broad and narrow-line regions (4 and 5). Ly α emission may come from these clouds, excited by the X-ray radiation emitted from the accretion disk. Furthermore, it is believed that the ionised matter in

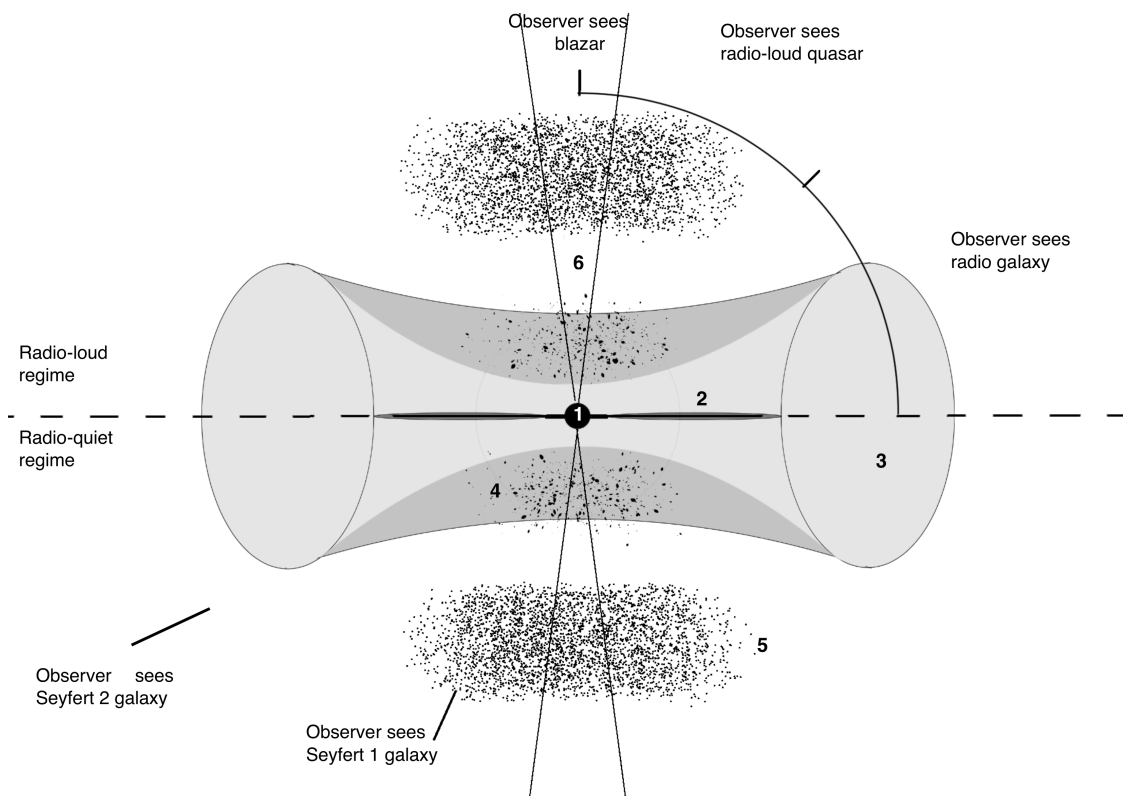


Figure 1.11: An overview of structure of an AGN and the possible origins of the different types of radiation considered in this thesis. 1- Supermassive Black Hole, estimated to have a mass of $10^6 - 10^{10} M_{\odot}$; 2- Accretion disk. UV emission like $\text{Ly}\alpha$ and X-ray emission is originated here, through the Inverse Compton effect. Gamma rays may also be emitted here through this process; 3- Dust Torus. The radiation from the accretion disk and black hole heats up the dusty torus surrounding them, which then gets re-radiated through the Infrared band; 4- Broad band region, estimated to exist at $\sim 0.1 - 0.2 \text{ ly}$ from the supermassive black hole. Broad emission lines get generated here.; 5- Narrow line region, estimated to be situated at $\sim 150 \text{ ly}$ from the supermassive black hole. The gas clouds get excited from the radiation coming from the inner regions and emit narrow emission lines. $\text{Ly}\alpha$ is generally believed to come from these regions; 6- Relativistic jets. Charged particles are accelerated through strong, collimated magnetic fields, leading to Synchrotron radiation emitted in the radio band. Depending on the line-of-sight, an AGN can appear as different types of objects, such as blazars or radio galaxies.

the accretion disk may get caught in the strong magnetic fields that surround the vicinity of the accreting black hole and be expelled at relativistic speeds through polar jets (6). The exact processes through which these phenomena are produced is not yet understood, but relativistic jets from AGN stand as some of the most powerful emissions in astrophysics, emitting in bandwidths from radio to X-rays, often extending far away from their galaxy of origin, even reaching outside the dark matter halo of the host galaxy.

Initial studies into the nature of active galaxies resulted in a plethora of different objects being found, from Seyfert galaxies (first described by Seyfert, 1943) to Quasars and Blazars (Shields, 1999). However, current models generally consider all active galaxies to be the same type of object, powered by a central accreting supermassive black hole, while explaining their observable differences as the result of observing the same object through different angles (see Figure 1.11, although reservations remain about the validity of the unification approach for, for example, radio-quiet AGN, see Antonucci, 1993; Urry & Padovani, 1995).

1.2.4 The black hole-host galaxy connection

There is evidence for the existence of supermassive black holes in at least 85 galaxies, based on spatially resolved stellar kinematics (Kormendy & Ho, 2013), and it is believed that all galaxies host supermassive black holes in their midst. With the detections of separate SMBHs, came the discovery of relations between the SMBH and the host galaxy that pointed to black holes having influence in the way galaxies grew and vice-versa (Booth & Schaye, 2011).

1.2.4.1 The M_{\bullet} – L_{bulge} relation

There are several results which point to the existence of a possible relation between SMBHs and their host galaxies. The first correlation to be found was the correlation between BH masses (M_{\bullet}) and the luminosity of the bulge (L_{bulge}) of a galaxy (Dressler & Richstone, 1988; Kormendy, 1993). This possibility was later confirmed by Magorrian et al. (1998) who also confirmed SMBHs in all

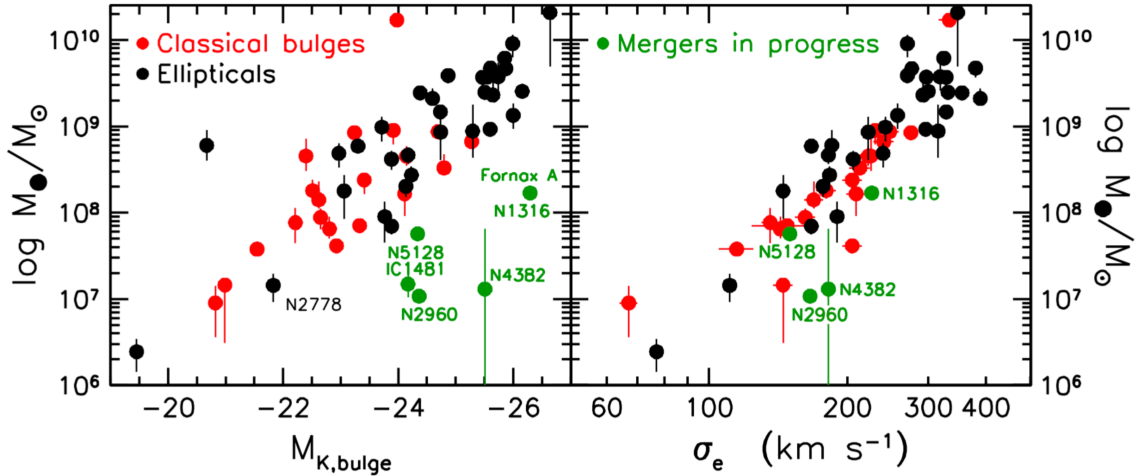


Figure 1.12: The $M_{\bullet} - M_{\text{bulge}}$ (Left) and $M_{\bullet} - \sigma$ (Right) relations (taken from Kormendy et al. 2013).

but 6 galaxies of their sample, setting the stage for today’s belief that all bulges contain SMBH (see also, e.g. Ferrarese & Merritt, 2000; Hopkins et al., 2007).

The correlation between M_{\bullet} and L_{bulge} (or bulge mass, M_{bulge} , as luminosity is connected to the amount of stars available in the bulge), is well established and allows us to infer on which parts of the galaxy co-evolve with AGNs.

1.2.4.2 The $M_{\bullet} - \sigma$ relation

A correlation between the mass of black holes and a galaxy’s velocity dispersion (σ) was found by Ferrarese & Merritt (2000) and Gebhardt et al. (2000). Both teams were quick to point out that the existence of this correlation allowed for the determination of SMBH masses from an easily determinable observable (the galaxy’s velocity dispersion). It also further supported the connection between SMBHs and bulges, first found through the $M_{\bullet} - M_{\text{bulge}}$ relation.

The existence of these relations hinted at a close relationship between the supermassive black holes and their host galaxies, something that became even more apparent when Astrophysicists tried to reproduce the evolution of galaxies through theoretical modelling.

1.2.5 The regulation of galaxy growth

As said before, the details on the process of star formation are not yet well understood and observations have shown that less than 10% of normal baryonic matter in the Universe is in the form of stars. Following the CDM models, it would be expected for most of the gas in the Universe to have been transformed into stars. That this has not happened suggests the existence of mechanisms that regulate the formation of stars in galaxies and prevent runaway scenarios that would have expended the gas reserves in the present Universe.

In the absence of these processes, many observed characteristics of the observed galaxy population cannot be reproduced by our theoretical models: the low percentage ($\sim 10\%$, Fukugita et al., 1998) of the baryonic matter that gets converted into stars (the Overcooling problem), the flattening of the faint end of the luminosity function (Benson et al., 2003; White & Rees, 1978), the cosmic star formation history (White & Frenk, 1991), just to name a few.

The secular, internal processes which influence galaxy evolution are generally called feedback processes. Feedback processes are generally separated into two different categories, based on their originating process: stellar feedback and AGN feedback. Without them, we are unable to explain how galaxies are the way they are today since, given the high rate at which gas cools down within galaxies, current galaxies should have formed many more stars than they are observed to have and should be much more massive and luminous than they are.

1.2.5.1 Stellar feedback

Feedback from star formation (stellar winds, radiation pressure and supernovae) is collectively referred to as stellar feedback. The energy released into the surrounding environment by these processes can eject material from the galaxy via outflows (Veilleux et al., 2005).

Beyond affecting the production of stars in a galaxy, it is possible that stellar feedback can also significantly constrain the growth of supermassive black holes in the galaxy, especially in sub $\sim L_*$ galaxies, where the stellar feedback produces effective outflows and starves the inner regions of the galaxy of fuel for the black hole. The point at which this feedback begins to lose effectiveness is thought

to be at the first meaningful period of black hole growth of the galaxy, but the exact moment it happens, the mass scale at which it occurs and the triggering mechanism for this loss of effectiveness is still uncertain and open to debate.

1.2.5.2 AGN feedback

For $> L_*$ galaxies, the feedback from stellar processes has little impact on their evolution. It is thought that an amount of energy up to 20-50 times higher than provided by stellar feedback is needed for these massive galaxies and a possible energy source is AGN feedback. Including AGN feedback in the picture of galaxy evolution solves the “overcooling problem” and also forges a relation between the SMBH and the host galaxy. Therefore, AGN feedback is also used to explain the observed correlation between SMBH and galaxy mass or stellar velocity dispersion. If a BH is massive enough, outflows from its centre will eventually drive the gas from the galaxy, regulating star formation and galaxy growth.

There are essentially two modes of AGN feedback: quasar mode and radio mode. In the first one, the SMBH accretes large amounts of matter and tends to produce strong radiative winds that expel gas out of the host galaxy, leading to the quenching effects alluded to in the last paragraph. In the second one, the BH accretes at a lower rate and forms relativistic jets that heat the galactic halo and medium, preventing cooling of gas in the massive haloes and causing the bright end of the observed luminosity functions. This mode is responsible for keeping a galaxy quenched and is therefore also referred to as “maintenance” mode (Weinberger et al., 2018).

The regulation of star formation explains the bimodal distribution of galaxy colours: massive, early-type galaxies are red and dead, quenched by the SMBH activity. Schawinski et al. (2007) found observational evidence of this, where star-forming, early-type galaxies with AGN were shown to be significantly closer to the red sequence than those without AGN. However, just as it happens with star formation, AGN feedback does not only impact galaxy growth negatively. Instances of positive feedback from AGN activity also exist, where the AGN outflows compress dense gas clouds and trigger star formation or relativistic jets

hit protogalactic clouds and cause them to collapse. The enhanced pressure of the AGN feedback accelerates molecular hydrogen cloud formation and is therefore responsible for instigating star formation and galaxy growth.

1.3 The growth of galaxies and supermassive black holes across cosmic time

By studying a galaxy's formation of stars and the accretion onto the central black holes of galaxies at different epochs in the Universe, Astrophysicists are able to construct a general overview of how galaxies and SMBHs grow across cosmic times. These are the Cosmic Star-Formation and the AGN Accretion Histories.

1.3.1 Cosmic Star-formation History

The cosmic Star Formation History (SFH), the global star formation rate density (SFRD) of galaxies as a function of cosmic time, is one of the primary goals of observational astrophysics. The objective being that knowing how SFR evolves with redshift will eventually allow us to, at least, facilitate the full understanding of the events that lead from the formation of the first stars to present-day galaxies and stellar populations.

However, modelling the SFH is not a trivial undertaking, due to the many physical processes involved. An alternative approach consists in looking at the emission of the entire galaxy population, from the far-ultraviolet (FUV) to the FIR. This method relies on some basic properties of stellar populations and is independent of the complex evolution of individual galaxies.

With the use of these techniques, astronomers are able to map the transformation of gas into stars, as well as the reionization of the Universe, from the cosmic dark ages to present-time. A consistent picture emerges where the SFRD peaks at $z \sim 2,5$ (~ 3.5 Gyrs after the Big-Bang) and then drops for $z < 2$ (Figure 1.13 - see also Madau & Dickinson, 2014). The results effectively show that stars formed nine times faster in the past than they do today, with only 25% of the present-day stellar mass density (SMD) having been formed in the last 6 Gyrs.

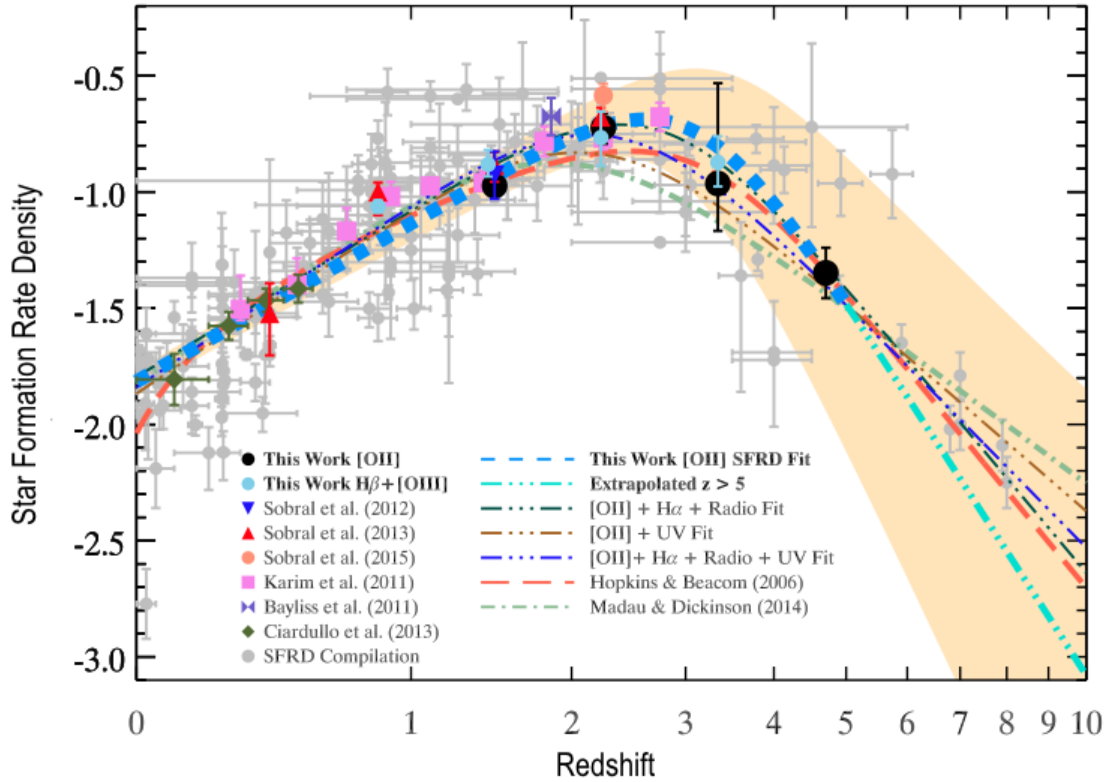


Figure 1.13: The evolution of O[II] dust and AGN corrected SFRD across cosmic time by Khostovan et al. (2015). The blue dashed line represents the best fit, based solely on the measurements by Khostovan et al. (2015). The light blue dashed-dotted line shows the extrapolation of the evolution of the SFRD into higher redshifts. The shaded golden regions represent the 1σ uncertainty region. Also included are data points and fits from other studies employing different datasets and wavelengths. The plot shows that SFRD peaks at $z = 2 - 3$, having been decreasing since then.

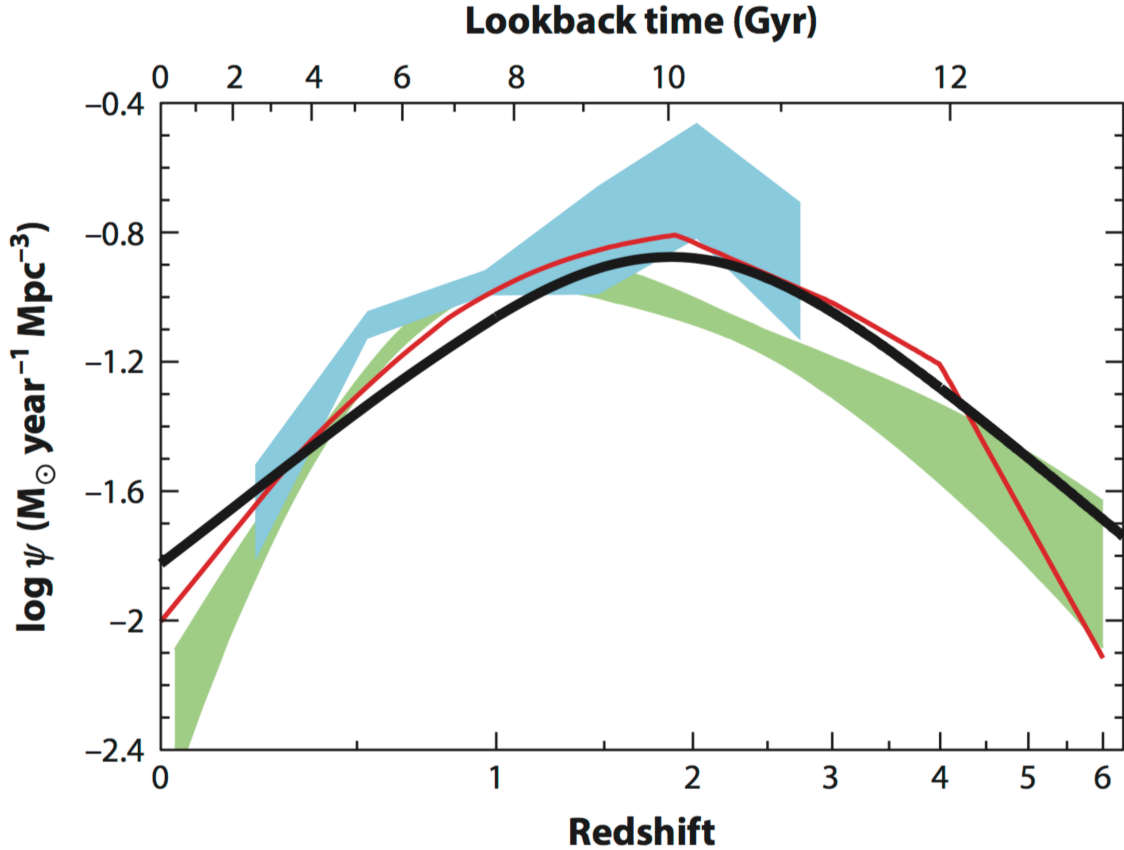


Figure 1.14: The AGN accretion history (from Madau & Dickinson 2014). Red line and green shade is data from X-rays (shades are all 1σ). Blue is from infrared and the black solid curve is the best fit star-formation history.

1.3.2 AGN Accretion history

We do not know whether the scaling relations of SMBHs and host galaxies originated in the early Universe and were simply maintained through cosmic time or even what physical processes are responsible for such relations in the first place. It is also not understood whether quasar mode has an impact on the overall galaxy or if it affects just the nuclear region of the host. However there is a different perspective on the link between SMBHs and their host galaxies to be considered and that is the relationship between BH accretion and SFH.

The cosmic accretion history of SMBHs can be inferred from the Soltan argument (Soltan, 1982, which relates the bolometric luminosities of quasars and

the accretion rate of the BHs). This allows us to estimate the evolution of the accretion of mass onto SMBHs and compare it with the cosmic SFRD (see Figure 1.14 and Heckman & Best, 2014; Madau & Dickinson, 2014). The accretion rate peaks at slightly lower redshift than the SFRD and declines more rapidly from $z \sim 1$ to 0. However, AGN luminosity is usually determined from single bandwidths (X-ray, Radio, etc) and the usage of bolometric luminosities shows a closer agreement between the SFRD and the BH accretion history, suggesting a close link between SFR and BHAR at all redshifts.

However, there are also studies that suggest differences between the two accretion histories (e.g. Shankar et al., 2009) and it must be taken into account that the majority of these studies are made from AGN-selected populations (e.g. Stanley et al., 2015), as it is easier to detect AGN and measure accretion from these sources than it is for other populations. In this work, I endeavour to extend this research into purely star formation-selected samples of galaxies and probe at the joint evolution of BHs and star-forming host galaxies.

1.4 This thesis

This thesis focuses on work attempting to contribute to the understanding of the evolution of galaxies across cosmic time. In particular, it studies how these galaxies grow in comparison to the supermassive black holes they host, by characterising the X-ray and radio properties of the host galaxies and measuring and comparing the SFRs and BHARs of star-forming line-emitting galaxies at different epochs of the Universe. This thesis is organised in the following way: Chapter 2 presents the initial work on the co-evolution of SMBHs and their star-forming host galaxies by making use of the HiZELS survey to study the SMBH and SF activity of H α emitters (HAEs) at redshifts from $z = 0.4$ to $z = 2.23$ in the COSMOS field. We make use of the existing wealth of data available for the COSMOS field both through catalogue matching and stacking techniques in order to estimate the BH accretion rates and SFRs of HAEs and compare their growth across cosmic time. Chapter 3 introduces the follow up to that work by presenting the X-ray properties of star-forming galaxies at higher redshifts ($2 < z < 6$) as well

as AGN activity. Chapter 4 presents the radio properties of these same galaxies, also including AGN activity. Chapter 5 is dedicated to the SFRs of LAEs and how these relate with the SMBH and AGN activity explored before (Chapters 3 and 4), as well as connecting the results obtained at $z = 2 - 6$ to those from $z = 0.4 - 2$ (Chapter 2). Finally, Chapter 6 closes with the overall conclusions as well as perspectives for future venues of research and open questions.

This work uses a Chabrier initial mass function (Chabrier, 2003) and the following flat cosmology: $H_0 = 70 \text{ km s}^{-1} \text{ Mpc}^{-1}$, $\Omega_M = 0.3$ and $\Omega_\Lambda = 0.7$.

Chapter 2

The growth of typical
star-forming galaxies and their
super massive black holes across
cosmic time since $z \sim 2$

Abstract

Understanding galaxy formation and evolution requires studying the interplay between the growth of galaxies and the growth of their black holes across cosmic time. Here we explore a sample of H α -selected star-forming galaxies from the HiZELS survey and use the wealth of multi-wavelength data in the COSMOS field (X-rays, far-infrared and radio) to study the relative growth rates between typical galaxies and their central supermassive black holes, from $z = 2.23$ to $z = 0$. Typical star-forming galaxies at $z \sim 1 - 2$ have black hole accretion rates (\dot{M}_{BH}) of $0.001\text{-}0.01 M_{\odot} \text{yr}^{-1}$ and star formation rates of $\sim 10\text{-}40 M_{\odot} \text{yr}^{-1}$, and thus grow their stellar mass much quicker than their black hole mass (3.3 ± 0.2 orders of magnitude faster). However, $\sim 3\%$ of the sample (the sources detected directly in the X-rays) show a significantly quicker growth of the black hole mass (up to 1.5 orders of magnitude quicker growth than the typical sources). \dot{M}_{BH} falls from $z = 2.23$ to $z = 0$, with the decline resembling that of star formation rate density or the typical SFR (SFR*). We find that the average black hole to galaxy growth ($\dot{M}_{\text{BH}}/\text{SFR}$) is approximately constant for star-forming galaxies in the last 11 Gyrs. The relatively constant $\dot{M}_{\text{BH}}/\text{SFR}$ suggests that these two quantities evolve equivalently through cosmic time and with practically no delay between the two.

Calhau, J., Sobral, D., Stroe, A., Best, P., Smail, I., Lehmer, B.,
Harrison, C., Thomson, A., 2017, MNRAS, 464, 1

2.1 Introduction

Understanding how galaxies form and evolve is a very challenging task, as there are a range of complex processes and quantities that need to be taken into account and that usually cannot be studied in isolation, such as gas abundances, dust, supernovae, radiative winds and relativistic jets (e.g. Genel et al., 2014; Schaye et al., 2015). Both the star formation history (e.g. Karim et al. 2011; Lilly et al. 1996; Sobral et al. 2013) and the black hole accretion history (BHAH; Brandt & Alexander 2015) are strongly influenced by the feedback effects of both star formation and black hole (BH) accretion, as they affect the ability of the host galaxy to convert molecular gas into stars. For example, an active galactic nucleus is the result of the accretion of matter into the central supermassive black hole of a galaxy. A growing, massive BH releases copious amounts of energy so, provided that there is a strong coupling between radiation and the mechanical output of the BH and surrounding gas, the AGN may be able to disrupt the environment and in principle even quench the SF happening in the host galaxy (e.g. Bower et al., 2006; Silk & Rees, 1998). This may happen mainly in two ways: i) radiatively-driven winds and ii) relativistic jets.

Current studies cannot establish whether or not radiatively-driven winds have a significant effect on a galactic scale. Integral field unit (IFU) observations provide evidence for outflowing gas in local Seyferts (e.g. Davies et al., 2009; Schnorr Müller et al., 2011; Storchi-Bergmann et al., 2010) on scales of 10 – 100 pc. Conversely, spectro-polarimetry of low redshift quasars shows high-velocity outflows close to the accretion disk (e.g. Ganguly & Brotherton, 2008; Young et al., 2007). However, these winds are only observed along the line of sight and there are no direct constraints on the distribution of the outflowing gas, which makes it difficult to get a clear picture of how they affect the galaxy (e.g. Dunn et al., 2010; Harrison et al., 2012; Tremonti et al., 2007).

Relativistic jets are known to influence gas on a galactic scale, even reaching outside of the dark matter haloes of galaxies and, in addition, interact strongly with virialised hot atmospheres (e.g. Best et al., 2005; McNamara et al., 2009, 2011; Nesvadba et al., 2006, 2007, 2008). The accretion of matter into the central black hole leads to the emission of radiation from both the accretion disk and

the relativistic jets and thus, in conjunction with star formation processes and gas dynamics, AGN are thought to be responsible for regulating the evolution of galaxies - but it may well be that AGN feedback mostly works as a maintenance mode (e.g. Best et al., 2005, 2006) rather than be responsible for the actual quenching process.

Stellar feedback also plays a major role in regulating star formation. This can happen through extreme events like strong stellar winds or shock waves of supernovae explosions (Geach et al., 2014). Typical outflows from star formation involve only small fractions of the molecular gas in Milky Way type galaxies (but are much more important for very low mass galaxies) and thus stellar feedback is generally considered to be insufficient for the regulation without the contribution of an AGN.

In order to understand how galaxies evolve, it is particularly important to understand how key properties such as the star formation rate and the black hole accretion rate (\dot{M}_{BH}) in active galactic nuclei evolve as a function of cosmic time. This can be done by examining the star formation and black hole accretion histories of galaxies. The latest surveys show that star formation activity peaks at $z \sim 2$ (e.g. Madau & Dickinson, 2014; Sobral et al., 2013) and then declines until today. As for the black hole accretion rates, the peak may happen at slightly lower redshifts than the peak of star formation, but the black hole activity may also decline more rapidly from $z \sim 1$ to 0 (e.g. Aird et al., 2010). However, studies taking into account the bolometric luminosity functions of AGN (e.g. Delvecchio et al., 2014) show that black hole accretion tracks the evolution of SF more closely, peaking at $z \sim 2$.

Most studies on the evolution of SF and BH accretion tend to focus on AGN selected samples. Stanley et al. (2015), for example, found that while there is a strong evolution of the average SFR with redshift, the relation between SFR and AGN luminosity seems relatively flat for all redshifts. The authors interpreted this as being due to the effect of short time-scale variations in the mass accretion rates, which might erase any relation that might exist between the SFR and AGN luminosity. Nevertheless, there are also studies with star-forming selected samples: Delvecchio et al. (2015) analysed the relation of AGN accretion and SFR for star-forming galaxies up to $z \sim 2.5$ and found that the ratio between the

\dot{M}_{BH} and the SFR evolves slightly with redshift, and has a lower value compared to what one would need to obtain the local $M_{\text{BH}}-M_{\text{Bulge}}$ relation. Lehmer et al. (2013) also investigated the $\dot{M}_{\text{BH}}/\text{SFR}$ ratio using galaxy samples from both the field and a high-density structure (super-cluster of QSO from the 2QZ survey) at $z \sim 2.23$. Lehmer et al. (2013) found that $\text{H}\alpha$ emitting galaxies in this structure have a relatively high fraction of AGN activity, leading to average $\dot{M}_{\text{BH}}/\text{SFR}$ which are closer to what is typically measured for AGN. For more typical “field” $\text{H}\alpha$ emitters, the $\dot{M}_{\text{BH}}/\text{SFR}$ was found to be typically an order of magnitude lower than for AGN and for $\text{H}\alpha$ emitters in the higher density region at $z \sim 2$. These results suggest that SF galaxies are generally situated below the local relation (at least at redshifts of $z \sim 2$) and that the activity of the AGN causes the ratio to rise high enough so that the galaxies approach a growth mode that could easily result in the observed local relation. However, much is still unknown, for typical, star-formation selected samples, regarding the relative growth of the black hole and the host galaxies, and particularly how such relative growth may vary with time, from the peak of the star formation history, at $z \sim 2.5$ to $z \sim 0$.

In this paper we explore a sample of “typical” star-forming galaxies from HiZELS in the COSMOS field, selected in four different redshift slices in a self-consistent, homogenous way. We explore the wealth and variety of exquisite data in the COSMOS field to study the relative growth between the central black holes and their host galaxies, and how that varies across cosmic time. This paper is organised as follows: Section 2 presents the data and sample. Section 3 provides an overview of our selection of potential AGNs. Section 4 presents our stacking analysis in different bands. Section 5 presents the results: the relative supermassive black hole/galaxy growth and in section 6 we present the conclusions. In this paper, we use a Chabrier IMF (Chabrier, 2003) and the following cosmology: $H_0=70 \text{ km s}^{-1} \text{ Mpc}^{-1}$, $\Omega_M=0.3$ and $\Omega_\Lambda=0.7$.

2.2 Data and sample

2.2.1 Data: X-rays, radio & FIR

2.2.1.1 X-rays: C-COSMOS

The *Chandra* Cosmos Survey (C-COSMOS; Elvis et al., 2009; Puccetti et al., 2009) imaged the COSMOS field (Scoville et al., 2007) with an effective exposure time of ~ 180 ks and a resolution of $0.5''$. The limiting source detection depths are $1.9 \times 10^{-16} \text{ erg s}^{-1} \text{ cm}^{-2}$ in the soft band (0.5-2 keV), $7.3 \times 10^{-16} \text{ erg s}^{-1} \text{ cm}^{-2}$ in the hard band (2-10 keV), and $5.7 \times 10^{-16} \text{ erg s}^{-1} \text{ cm}^{-2}$ in the full band (0.5-10 keV). The data allows us to track X-ray emission from processes like Bremsstrahlung and inverse Compton scattering, and thus to identify which sources are AGN based on their X-ray emission. C-COSMOS only covers the relatively central area of COSMOS (0.9 deg^2), and thus we restrict our analysis to that region.

2.2.1.2 Radio: VLA-COSMOS

The VLA-COSMOS Survey (Bondi et al., 2008; Schinnerer et al., 2004, 2007) used the National Radio Astronomy Observatory's Very Large Array (VLA) to conduct deep ($\sigma_{1.4} \sim 10 \mu\text{Jy}/\text{beam}$), wide-field imaging with $\approx 1.5''$ resolution at 1.4 GHz continuum of the 2 square-degree COSMOS field. With this band, we track the radio emission of AGN via synchrotron radiation from SMBH relativistic jets and estimate SFRs from the synchrotron radiation due to supernovae explosions (Schmitt et al., 2006).

2.2.1.3 Far-infrared: Herschel

COSMOS was imaged with the *Herschel* telescope as part of the *Herschel* Multi-tiered Extragalactic Survey, HerMES (Oliver et al., 2012). HerMES is a legacy program that mapped 380 deg^2 of the sky - *Herschel*-SPIRE ($250 \mu\text{m}$, $350 \mu\text{m}$ and $500 \mu\text{m}$, with a PSF FWHM of $18.1''$, $24.9''$ and $36.6''$, respectively; Griffin et al., 2010). We additionally make use of the *Herschel* PACS Evolutionary Probe program (PEP: $100 \mu\text{m}$ and $160 \mu\text{m}$, with PSFs of $7.2''$ and $12''$; Lutz

et al., 2011) and the observations of the Submillimeter Common-User Bolometer Array 2 (SCUBA2) on the James Clerk Maxwell Telescope, at $850\mu\text{m}$, for the COSMOS Legacy Survey (Geach et al., 2013). These bands cover the peak of the redshifted thermal spectral energy distribution from interstellar dust for galaxies in the redshift range ($z \sim 0.4 - 2.2$) for the entire COSMOS field. The bands therefore capture optical and UV radiation that has been absorbed and re-emitted by dust.

2.2.2 The sample of $\text{H}\alpha$ emitters at $z = 0.4 - 2.23$

The High Redshift Emission Line Survey (HiZELS; Best et al., 2013; Geach et al., 2008; Sobral et al., 2009a,b, 2012, 2013) has surveyed some of the best-studied extragalactic fields for $\text{H}\alpha$ emitters at various narrow redshift ranges, from $z = 0.4$ to $z = 2.23$ (see Sobral et al., 2013). HiZELS used a set of narrow-band filters in the near-infrared J , H and K bands and the Wide Field CAMera (WFCAM, Casali et al., 2007) on the United Kingdom Infrared Telescope (UKIRT), coupled with a filter in the z' band (NB921; Sobral et al., 2012, 2013) mounted on Suprimecam on the Subaru telescope, to cover roughly 5 deg^2 of extragalactic sky. While it is true that using only $\text{H}\alpha$ as a tracer for star formation may cause us to miss obscured star formation, the use of bluer bands for the detection of star-forming galaxies (UV or bluer emission lines) would result in missing a much more significant part of the population. In addition, Oteo et al. (2015) showed that an $\text{H}\alpha$ selection is able to recover $\sim 100\%$ of star-forming galaxies (including the most dusty ones), and *Herschel* is then ideal to recover the full SFRs of such highly obscured galaxies (e.g. Ibar et al., 2013). Although HiZELS covers various fields, in this work we focus only on the COSMOS field due to the availability of deep data from the *Chandra* Observatory, on which we rely in order to measure the X-ray luminosities in our samples. HiZELS obtained large samples of $\text{H}\alpha$ selected galaxies at redshifts $z = 0.4$, $z = 0.84$, $z = 1.47$ and $z = 2.23$ in the COSMOS and UDS fields (Sobral et al., 2013). The $\text{H}\alpha$ emitters were selected using a combination of broad-band colours (colour-colour selections) and photometric redshifts. It is expected that the sample presents contamination (mainly due to $\text{H}\beta$, O[III] and O[II] emitters at higher redshifts) of $\sim 5\%$ for $z = 0.4 - 1.47$

and $< 10\%$ for $z = 2.23$. Spectroscopically confirmed sources are included in the sample and the sources confirmed to be other emission line emitters are removed. We refer the interested reader to Sobral et al. (2013) for the detailed explanation of the process of selection for the $H\alpha$ emitters. Furthermore, we note that while the HiZELS sample at $z = 0.4$ (obtained with the Subaru telescope) probes down to significantly lower $H\alpha$ luminosities and stellar masses (see Sobral et al., 2014) than those at higher redshift, it also covers a significantly smaller volume, and thus misses massive, bright sources (see Figure 2.1). In an attempt to make the $z = 0.4$ sample more comparable to those at higher redshift, we apply a mass cut of $M > 10^9 M_{\odot}$. As we will rely on *Chandra* data for deep X-ray data (§2.2.1.1), we also need to restrict our analysis to the area in COSMOS with deep *Chandra* coverage. Thus, our final sample is composed of 35, 224, 137 and 276 $H\alpha$ emitters at $z = 0.40$, $z = 0.84$, $z = 1.47$ and $z = 2.23$. These are the sources restricted by *Chandra* coverage but include both the ones detected in the C-COSMOS survey and the ones without detectable X-ray emission. We present the distribution of $H\alpha$ (observed luminosities) in Figure 2.1.

2.3 AGN selection

2.3.1 X-ray detections

X-rays are one of the best ways to search for AGN. As matter falls into the black hole, it heats up, leading to the emission of radiation in the X-rays through inverse-Compton scattering of UV emission coming from the accretion disk. As the X-ray luminosity is expected to scale with the accretion rate, we can use X-ray luminosities to not only identify AGN, but also to obtain an estimate of the SMBH growth rates.

We cross-correlate our sample of $H\alpha$ emitters with the *Chandra* X-ray catalogue with a $1''$ matching radius, in order to find which of our sources are directly detected in the X-rays and thus likely AGN. We find one direct detection at $z = 0.4$ ($2.9 \pm 1.7\%$ of the total sample at this redshift. All fraction errors were estimated by taking the binomial counting errors.), seven at $z = 0.84$ ($3.1 \pm 1.8\%$),

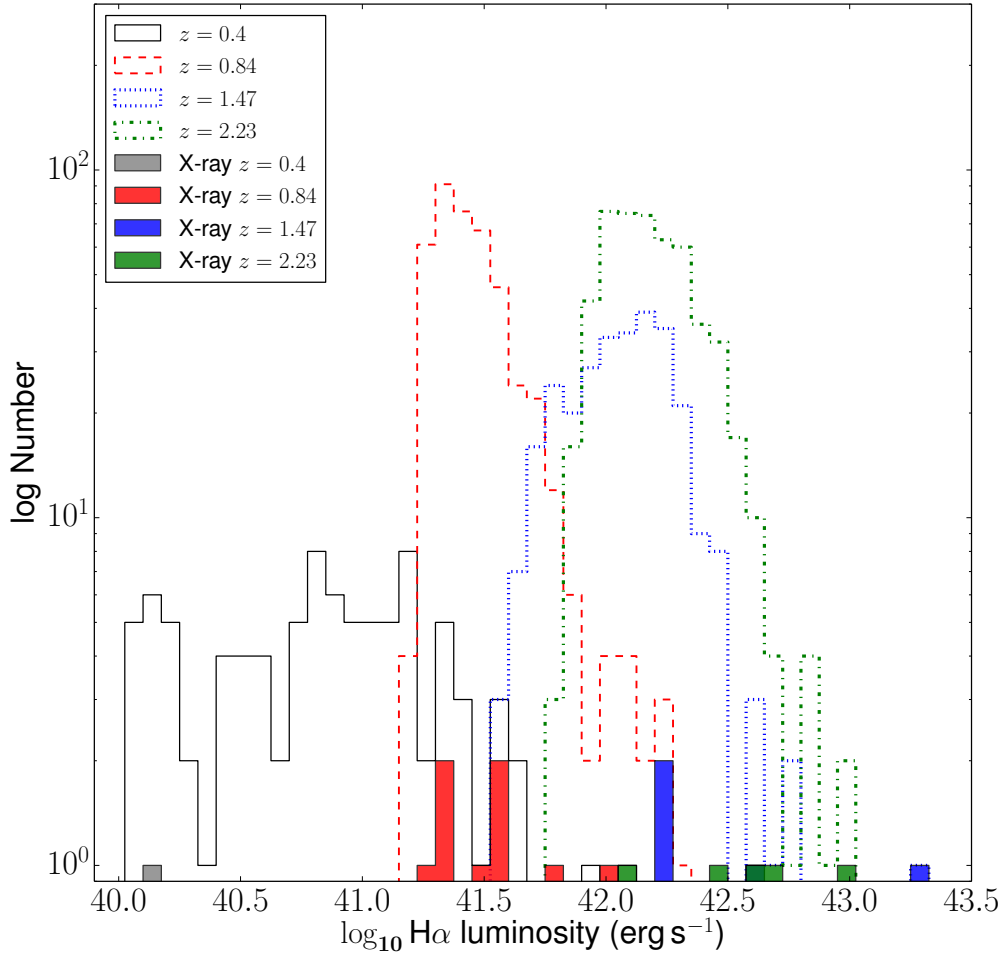


Figure 2.1: $H\alpha$ luminosity distribution of the sample of $H\alpha$ emitters that are used in this paper (after the application of a stellar mass cut, see §2.2.2) and those with individually detected X-ray emission (filled histograms). X-ray detected $H\alpha$ emitters have ‘typical’ to high $H\alpha$ luminosities. Note that the $z = 0.40$ sample covers a much smaller volume than those at higher redshift, thus missing luminous and rarer sources.

four at $z = 1.47$ ($2.9 \pm 1.7\%$) and five at $z = 2.23$ ($1.8 \pm 1.3\%$) in the C-COSMOS catalogue. The results are presented in Table 2.1. The directly detected sources possess X-ray luminosities of the order of $\geq 10^{42}$ erg s $^{-1}$, which are typical of the luminosities expected from AGN in this band. Our results are consistent with a non-evolving fraction of X-ray AGN within H α selected samples over the last 11 Gyrs of cosmic time (since $z \sim 2.2$), although we have low number statistics. In Figure 2.1 we present the H α luminosity distribution of the directly detected AGN, finding that they have preferentially higher than average H α luminosities, raising the possibility that our sources might be contaminated in the H α by AGN.

2.3.2 Radio detections

We cross correlated the VLA-COSMOS deep catalogue with our H α emitters. Our match between the VLA-COSMOS and our sources resulted in: i) one source is detected at $z = 0.4$ ($2.9 \pm 1.7\%$, with the errors taken from the binomial errors), 11 radio sources for $z = 0.84$ ($4.9 \pm 2.2\%$), 7 sources for $z = 1.47$ ($5.1 \pm 2.3\%$) and 9 for $z = 2.23$ ($3.3 \pm 1.8\%$). We estimated the (rest-framed) radio luminosities by using:

$$L_{1.4\text{GHz}} = 4\pi d_L^2 S_{1.4\text{GHz}} 10^{-33} (1+z)^{\alpha-1} (\text{WHz}^{-1}), \quad (2.1)$$

where d_L is the luminosity distance (in cm), $S_{1.4\text{GHz}}$ is the flux density in mJy and α is the radio spectral index - assumed to be 0.8, the characteristic spectral index of synchrotron radiation. 0.8 is a good average value for SF-dominated galaxies (e.g. Thomson et al., 2014), although it is not clear if this value is the best choice if the sample contains a large quantity of AGN. Our SF-selected sample should not have too many AGN (see Table 2.3) so $\alpha = 0.8$ should be appropriate. Within our H α emitters, the radio sources have radio luminosities of the order of $\sim 10^{21}$ WHz $^{-1}$ at $z = 0.40$, $\sim 10^{23}$ WHz $^{-1}$ for $z = 0.84 - 2.23$. It is possible for radio detect up emission from a population of supernova remnants as well. However the emission from these sources have lower luminosity than the AGN we are tracing and should not contaminate the measurements.

Table 2.1: The luminosity in the X-rays and central \dot{M}_{BH} for the sources directly detected by the C-COSMOS survey (all sources directly detected have luminosities higher than 10^{41} erg s $^{-1}$). Errors were computed using standard error propagation from the flux errors provided in the C-COSMOS survey catalogue (Elvis et al., 2009).

* - These sources were taken directly from the tables of the HiZELS survey. In order to get the HiZELS designation for each galaxy, one should add "HiZELS-COSMOS-NB# DTC" to the beginning of the source's name, where # stands for the number or letter identifying the filter.

Source ID* (S13)	Redshift	$\log_{10} L_{H\alpha}$ [erg s $^{-1}$]	$\log_{10} L_X$ [erg s $^{-1}$]	\dot{M}_{BH} [M_{\odot} yr $^{-1}$]
S12-93079	0.40	40.1	41.97 \pm 0.09	0.003 \pm 0.0008
S12-22675	0.84	41.3	43.32 \pm 0.04	0.074 \pm 0.008
S12-33061	0.84	41.6	43.77 \pm 0.03	0.207 \pm 0.016
S12-26956	0.84	42.0	43.89 \pm 0.03	0.273 \pm 0.02
S12-11275	0.84	41.4	42.76 \pm 0.09	0.02 \pm 0.004
S12-6454	0.84	41.6	42.85 \pm 0.07	0.024 \pm 0.005
S12-4541	0.84	41.5	42.96 \pm 0.08	0.032 \pm 0.007
S12-2436	0.84	41.2	42.69 \pm 0.14	0.017 \pm 0.006
S12-23041	1.47	42.2	43.93 \pm 0.04	0.3 \pm 0.032
S12-19279	1.47	43.3	44.88 \pm 0.01	2.69 \pm 0.074
S12-20593	1.47	42.6	43.40 \pm 0.07	0.087 \pm 0.016
S12-44372	1.47	42.2	42.96 \pm 0.14	0.032 \pm 0.013
S12B-1528	2.23	43.0	43.67 \pm 0.08	0.16 \pm 0.033
S12B-1073	2.23	42.6	43.48 \pm 0.11	0.106 \pm 0.032
S12B-9274	2.23	42.7	43.66 \pm 0.10	0.098 \pm 0.042
S12B-1139	2.23	42.5	43.38 \pm 0.14	0.085 \pm 0.032
S12B-2306	2.23	42.0	43.45 \pm 0.13	0.1 \pm 0.035

2.4 Stacking analysis: \dot{M}_{BH} and SFR

2.4.1 Radio stacking: SFR

After rejecting all strong radio sources within our $\text{H}\alpha$ selected samples, we can stack the remaining sources, and use radio luminosities as a dust-free star-formation indicator (although some contribution of lower luminosity AGN will still be present, thus likely biasing results towards high star formation rates). We follow the same stacking procedure as for our X-ray stacking (see section 2.4.3) and find high signal-to-noise ratio (S/N) detections of our mean radio stacks in every redshift (see Figure 2.2). We find radio luminosities of $4.6 \times 10^{21} \text{ W Hz}^{-1}$, $3.3 \times 10^{22} \text{ W Hz}^{-1}$, $2.0 \times 10^{23} \text{ W Hz}^{-1}$ and $1.0 \times 10^{23} \text{ W Hz}^{-1}$ for $z = 0.4, 0.84, 1.47$ and 2.23 respectively.

To convert the luminosities to SFR, we adopted the conversion determined by Yun et al. (2001) converted to a Chabrier IMF (e.g. Karim et al., 2011):

$$\text{SFR}_{1.4\text{GHz}} = 3.18 \times 10^{-22} L_{1.4\text{GHz}} (\text{M}_{\odot} \text{yr}^{-1}). \quad (2.2)$$

Where $L_{1.4\text{GHz}}$ is the radio luminosity at 1.4 GHz in W Hz^{-1} . The conversion is suitable for radio luminosities up to, and including, $10^{24} \text{ W Hz}^{-1}$ and thus expected to yield reasonable results. We find SFRs of $\approx 1.5 \text{ M}_{\odot} \text{yr}^{-1}$, $10.5 \text{ M}_{\odot} \text{yr}^{-1}$, $62 \text{ M}_{\odot} \text{yr}^{-1}$ and $21 \text{ M}_{\odot} \text{yr}^{-1}$ at $z = 0.4, 0.84, 1.47$ and 2.23 respectively (see Table 2.2).

2.4.2 FIR stacking: SFRs

When estimating the SFR, it is important to make sure that there is no contamination to the luminosities by the activity of the AGN. FIR emission from the cold dust (rest frame 40-500 μm Netzer et al., 2007; Rowan-Robinson, 1995; Schweitzer et al., 2006) should have little to no such contamination.

Cross-correlating our sample with the HerMES catalogue with a 1" matching radius resulted in 2 sources being directly detected for $z = 0.4$, 10 for $z = 0.84$, 5 for $z = 1.47$ and 7 galaxies directly detected for $z = 2.23$ (See also Ibar et al.,

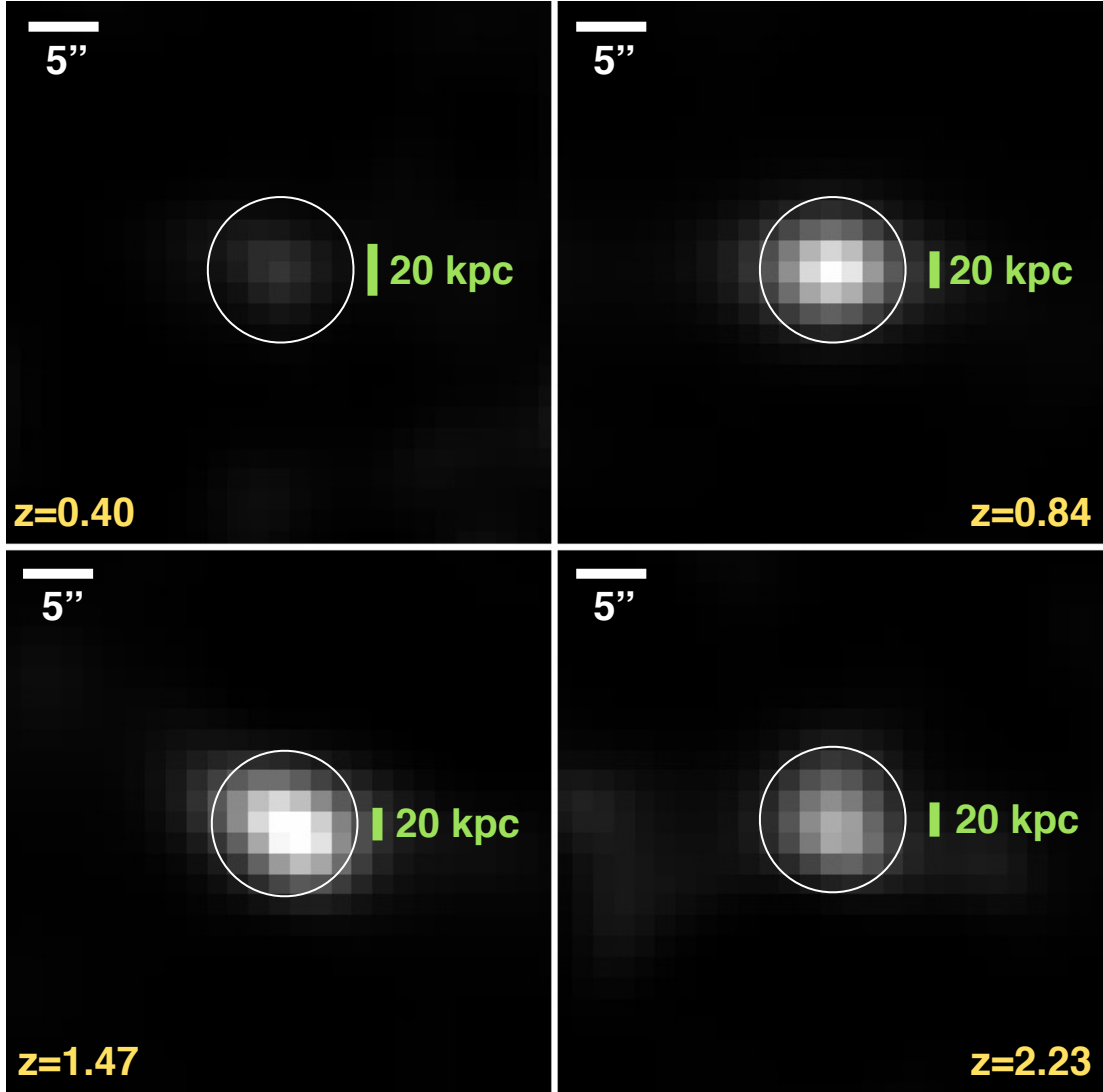


Figure 2.2: Stacking in the radio (1.4 GHz) for our non-radio AGN sources, at each redshift. We find strong detections at every redshift with luminosities of $\approx 10^{21-23} \text{ W Hz}^{-1}$, corresponding to SFRs of $\sim 1.5 - 63 M_{\odot}$. The images were smoothed for easier inspection.

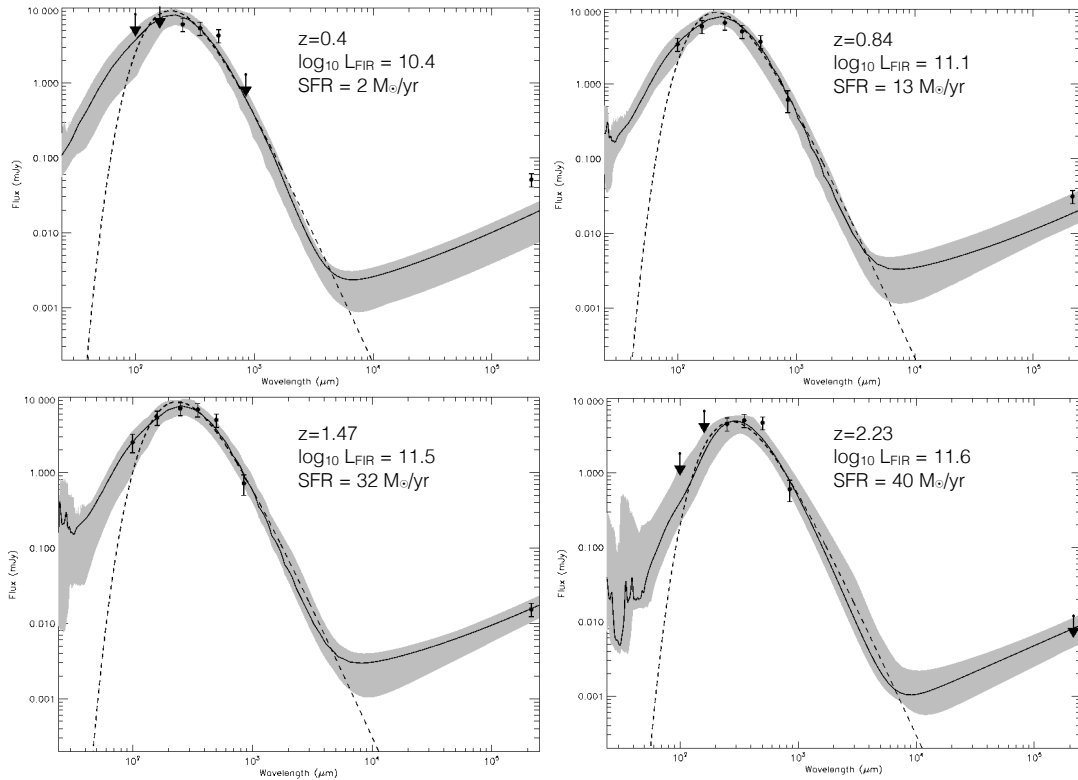


Figure 2.3: SED fitting for each redshift slice in the far-infrared bands. The data points were obtained in each band by stacking the entire sample for each redshift using mean statistics. The IR luminosity was estimated by fitting modified black-body templates to the $100\mu\text{m} - 850\mu\text{m}$ data points and integrating the best fit between $8\mu\text{m}$ and $1000\mu\text{m}$.

2013; Oteo et al., 2015). As expected, most of the sample, made of much more “typical” star-forming galaxies, is below the depth of *Herschel*, or SCUBA-2, in COSMOS. However, by the means of stacking, one can reach much lower flux limits, and thus detect the mean star-forming galaxy at each redshift. In order to obtain the necessary SFRs we make use of the results achieved by Thomson et al. (2016). The stacks were obtained through mean statistics accounting for background emission and confusion noise. Aperture corrections were applied for the PACS 100 μm and 160 μm bands, as specified in the PACS PEP release notes. In the SPIRE 250, 350 and 500 μm , the fluxes were taken from the peak value in each stack.

The IR luminosities were then estimated by fitting modified black-body (grey-body) templates to the 100 μm – 850 μm data points and integrating the best fit between 8 μm and 1000 μm (see 2.3). We refer the interested reader to Thomson et al. (2016) for the description of the complete procedure.

We use the total FIR luminosity to compute SFRs (Chabrier IMF) by using:

$$\text{SFR} = L_{\text{IR}} \times 2.5 \times 10^{-44} \text{ (M}_{\odot}\text{yr}^{-1}\text{)}. \quad (2.3)$$

This translates to a SFR ranging from 2 – 38 $\text{M}_{\odot} \text{ yr}^{-1}$ at $z = 0.4 - 2.23$ (see Table 2.2).

2.4.3 X-ray stacking

The vast majority of our H α emitters ($\sim 98\%$) are undetected in the X-rays for the current C-COSMOS flux limit. This is expected given that the *Chandra* sensitivity limit is $> 10^{-16} \text{ erg s}^{-1} \text{ cm}^{-2}$. Thus, only relatively luminous AGN are expected to be X-ray detected, while our sample is strongly dominated by typical star-forming galaxies. However, we can rely on stacking in order to study the overall population of typical H α selected galaxies below the X-ray detection limit and recover much lower black hole accretion activity. In order to stack our samples of H α emitters, per redshift, we use the full energy band of C-COSMOS (0.5-7 keV) and start by cutting-out a square of $10'' \times 10''$ centred on each source. We adopt a stacking radius of $2''$ (the area radius from which we extract the

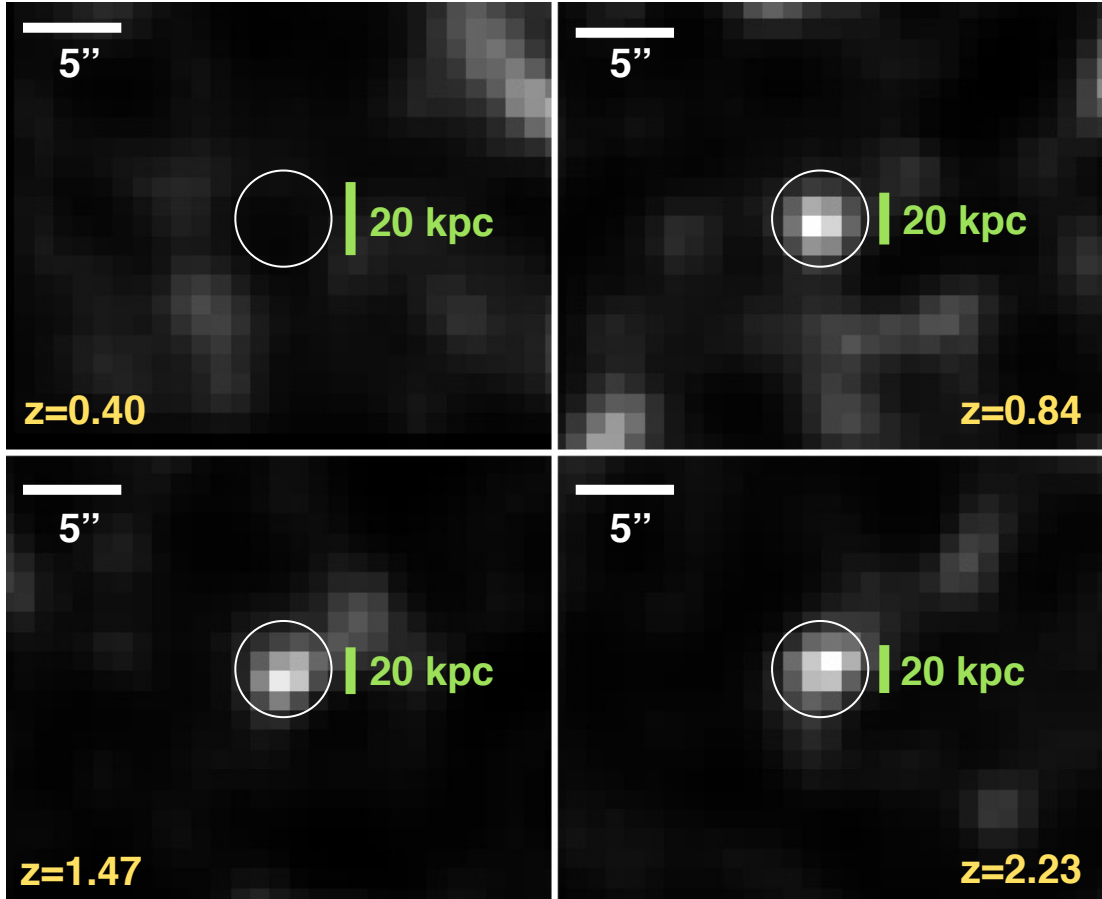


Figure 2.4: Stacking in the X-rays (*Chandra*'s full band) for all our $\text{H}\alpha$ sources within the C-COSMOS coverage, in each our redshift slices. The results show high S/N detections at every redshift except for $z = 0.4$. It is worth noting, however, that the sample at $z = 0.4$ is much smaller and has much lower stellar mass and SFR on average than the other redshifts considered, and fails to encompass the rare luminous objects like AGN (see Figure 2.1), since it comes from a much smaller volume than the samples at higher redshifts. The images in this figure have been smoothed for easier inspection.

counts for the fluxes). These values were obtained by going through different values for the radius, selecting the ones that maximised the signal-to-noise (S/N) ratio (see Lehmer et al. 2007 for details) and taking the mean. When stacking, we use all sources (both detected and non-detected), allowing us to include the entire population. *Chandra*'s PSF changes with the distance to the pointings, causing deformation of sources. However, the effect of the changing PSF is minimal when compared with the error bars and uncertainties inherent to the FIR analysis. As such we did not apply a correction to this effect and instead estimated the background contribution by taking the standard deviation of the pixel counts in a randomised number of areas of the same size of the stacking area, making sure these would fall outside the vicinity of the stacking radius, in order to counter the possible presence of sources distorted by the changes in *Chandra*'s PSF.

To convert background subtracted counts into fluxes we divided them by the mean exposure time multiplied by the conversion factor ($CR \times 10^{-11} \text{ erg cm}^{-2} \text{ s}^{-1} (\text{counts s}^{-1})^{-1}$, where CR is the count rate) assuming a power law of photon index $\Gamma = 1.4$ and a Galactic absorption $N_H = 2.7 \times 10^{20}$ as in Elvis et al. (2009). A photon index of 1.4 is appropriate for faint galaxies (see Alexander et al., 2003), as we expect star-forming galaxies to be. Finally, all images were background subtracted. The estimation of the luminosities was done following:

$$L_X = 4\pi d_L^2 f_X (1+z)^{\Gamma-2} (\text{erg s}^{-1}), \quad (2.4)$$

where d_L is the luminosity distance, f_X is the flux in the X-ray band, z is the redshift and Γ is the photon index, assumed to be 1.4.

Figure 2.4 shows the results of the stacking for the four redshifts. There are clear detections for $z = 0.84$, $z = 1.47$ and $z = 2.23$. For $z = 0.4$ the S/N is much lower. This is not surprising, as i) this is the smallest sample and particularly because ii) the sources in the $z = 0.4$ (due to the much smaller volume probed, see §2.2.2) are typically much lower luminosity and have lower stellar masses than those at higher redshift.

Table 2.2: Quantities estimated for the stacked sources. Fluxes and luminosities in the X-ray band and estimated black hole accretion rates from these quantities were estimated from C-COSMOS. SFR estimated from the FIR luminosities as determined by Thomson et al. (2016) and from radio data from VLA-COSMOS. Errors were estimated by taking the variance of the fluxes and applying standard error propagation in the subsequent derivations.

Source ID/Filter	z	log Flux (X-rays) $\text{erg s}^{-1} \text{cm}^{-2}$	log Luminosity (X-rays) erg s^{-1}	log Luminosity IR (FIR) (L_{\odot})	SFR (FIR) $M_{\odot} \text{yr}^{-1}$	SFR (Radio) $M_{\odot} \text{yr}^{-1}$	\dot{M}_{BH} $M_{\odot} \text{yr}^{-1}$	$\log [\dot{M}_{\text{BH}} / \text{SFR}]$ (FIR) (X-rays)
NB921	0.4	< -15.4	< 41.25	10.4 ± 0.26	$2^{+1.6}_{-0.9}$	$1.5^{+0.5}_{-0.2}$	< 0.0006	< -3.55
NBJ	0.85	-15.26 ± 0.12	42.12 ± 0.12	11.1 ± 0.23	$13^{+8.8}_{-5.2}$	$10.5^{+0.7}_{-0.6}$	0.004 ± 0.001	-3.51 ± 0.3
NBH	1.47	-15.06 ± 0.07	42.83 ± 0.07	11.5 ± 0.23	$32^{+21.7}_{-13.4}$	$62^{+3}_{-2.7}$	0.02 ± 0.004	-3.20 ± 0.28
NBK	2.23	-15.33 ± 0.12	42.94 ± 0.12	11.6 ± 0.42	$40^{+64.7}_{-24.9}$	$21^{+1.4}_{-1.3}$	0.03 ± 0.01	-3.10 ± 0.3

2.4.3.1 Black hole accretion rate from X-ray luminosity

We use the X-ray luminosity to estimate the rate at which the supermassive black hole at the centre of galaxies is accreting matter:

$$\dot{M}_{\text{BH}} = \frac{(1 - \epsilon)L_{\text{bol}}^{\text{AGN}}}{\epsilon c^2} (\text{M}_{\odot} \text{yr}^{-1}), \quad (2.5)$$

where \dot{M}_{BH} is the accretion rate of the black hole, ϵ is the accretion efficiency, $L_{\text{bol}}^{\text{AGN}}$ is the bolometric luminosity of the AGN, obtained by multiplying the X-ray luminosity by 22.4 (Lehmer et al., 2013; Vasudevan & Fabian, 2007), and c is the speed of light. We find that our typical star-forming galaxies have accretion rates that rise with increasing redshift, from $\approx 0.004 \text{ M}_{\odot} \text{yr}^{-1}$ at $z = 0.84$ to $\approx 0.03 \text{ M}_{\odot} \text{yr}^{-1}$ at $z = 2.23$. When extracting the accretion rates from the X-ray luminosities, we estimated the correction that would have to be taken into account from the contribution to the X-ray emission by SF. This correction was estimated following Lehmer et al. (2016):

$$\log L_X = A + B \log(\text{SFR}) + C \log(1 + z) \quad (2.6)$$

where A, B and C have the values 39.82 ± 0.05 , 0.63 ± 0.04 and 1.31 ± 0.11 respectively. The correction turned out to be at most $\sim 0.05\%$ of the total BH accretion, much less than the uncertainties in quantities like SFR and actual BHAR and, as such, we do not take it into account. It also seems to evolve with galactic stellar mass, growing as the mass grows and following $L_X = 1.44(\text{SFR}) - 0.45$ with $\chi^2 = 1.8$ when fitted to a linear relation through the least-squares method. This evolution of the contribution to the X-rays from stars is not surprising, as the SFR also grows with stellar mass (see 2.5.2 and 2.7).

Table 2.3: Number of H α emitters classified as possible and likely AGN according to the selections mentioned in Section 2.3. The errors in the fractions are binomial errors.

Method	$z = 0.4$	$z = 0.84$	$z = 1.47$	$z = 2.23$	Total
X-ray Counterpart (C-COSMOS)	1	7	4	5	18
X-ray AGN Fraction	$3 \pm 2\%$	$3 \pm 2\%$	$3 \pm 2\%$	$2 \pm 1\%$	$3 \pm 2\%$
Radio Counterpart (VLA-COSMOS)	1	11	7	9	28
Sources retained for stacking (X-rays)	35	224	137	276	672
Sources retained for stacking (Radio)	35	214	132	268	649
Sources retained for stacking (FIR)	35	224	136	276	671

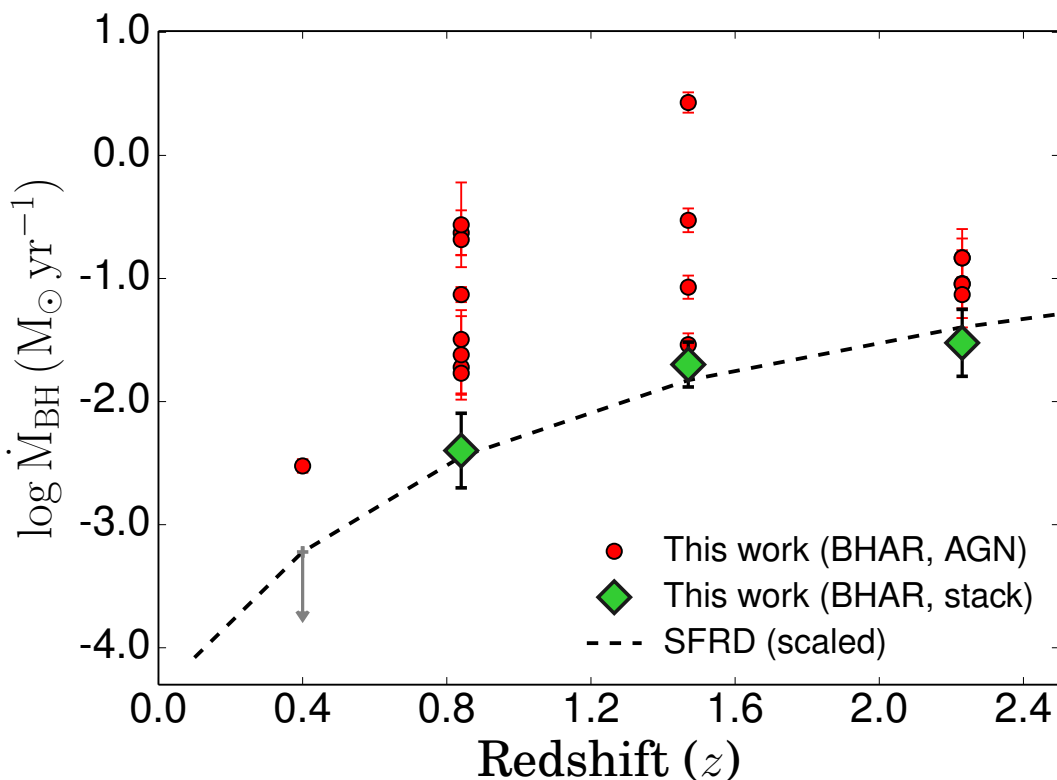


Figure 2.5: The evolution of black hole accretion rates (\dot{M}_{BH}), for individually detected (in the X-rays) AGNs and for the stacks of the full samples. We compare those with a scaled evolution of the star formation rate density, SFRD (Sobral et al., 2013). The SFRD has been scaled to coincide with the \dot{M}_{BH} at $z = 0.4$. The results show that the \dot{M}_{BH} grows with redshift, starting to plateau at $z \sim 2.23$ and that the SFRD evolves in a very similar way to the accretion rate of the BHs, starting to stabilise at around the same redshifts. The grey down arrow represents a non-detection for the $z=0.4$ stack.

2.5 Results

2.5.1 The cosmic evolution of black hole accretion rates

We find that \dot{M}_{BH} rises with increasing redshift as shown in Figure 2.5. However, from $z = 1.47$ to $z = 2.23$, even though the accretion rate still rises, it does so less steeply. This is consistent with the results in the literature: Aird et al. (2010) finds the peak of AGN luminosity density to be at $z = 1.2 \pm 0.1$. We compare this redshift evolution with the evolution of the star formation rate density, also shown in Figure 2.5. We use the results from Sobral et al. (2013, 2014) and scale them arbitrarily to look for any potential differences and/or similarities between the evolution of SFRD and \dot{M}_{BH} across cosmic time. Our scaling clearly reveals that star-forming galaxies form stars at a much higher rate than they grow their black holes (~ 3.3 orders of magnitude faster), but the relative evolution seems to be the same across redshift. We explore this further in Section 2.5.3. We also show the accretion rates computed for each individual X-ray AGN, which reveal large scatter (likely due to the high variability of AGN), but that generally agree with the trend of the global population.

2.5.2 The dependence of $\dot{M}_{\text{BH}}/\text{SFR}$ on stellar mass

Using the results from the FIR analysis we are able to estimate SFRs which should be independent of AGN activity. We use those to determine the ratio between the black hole accretion rate and SFR ($\dot{M}_{\text{BH}}/\text{SFR}$). Figure 2.6 shows how $\dot{M}_{\text{BH}}/\text{SFR}$ depends on stellar mass (stellar masses computed in Sobral et al., 2014) for the three different redshifts where we can easily split our samples. We find that a linear relation with a slope of -0.45 provides the best fit (see Figure 2.6). We find that both \dot{M}_{BH} and SFR increase with stellar mass, but SFR seems to rise slightly faster with stellar mass than \dot{M}_{BH} (see Figure 2.7). However, our results are still fully consistent with a completely flat relation (only $\sim 1\sigma$ away from a flat relation). This may be a sign that the BH accretion and SF of our typical star-forming galaxies evolve at equivalent rates across cosmic time, as we do not find any strong evidence for evolution with cosmic time either.

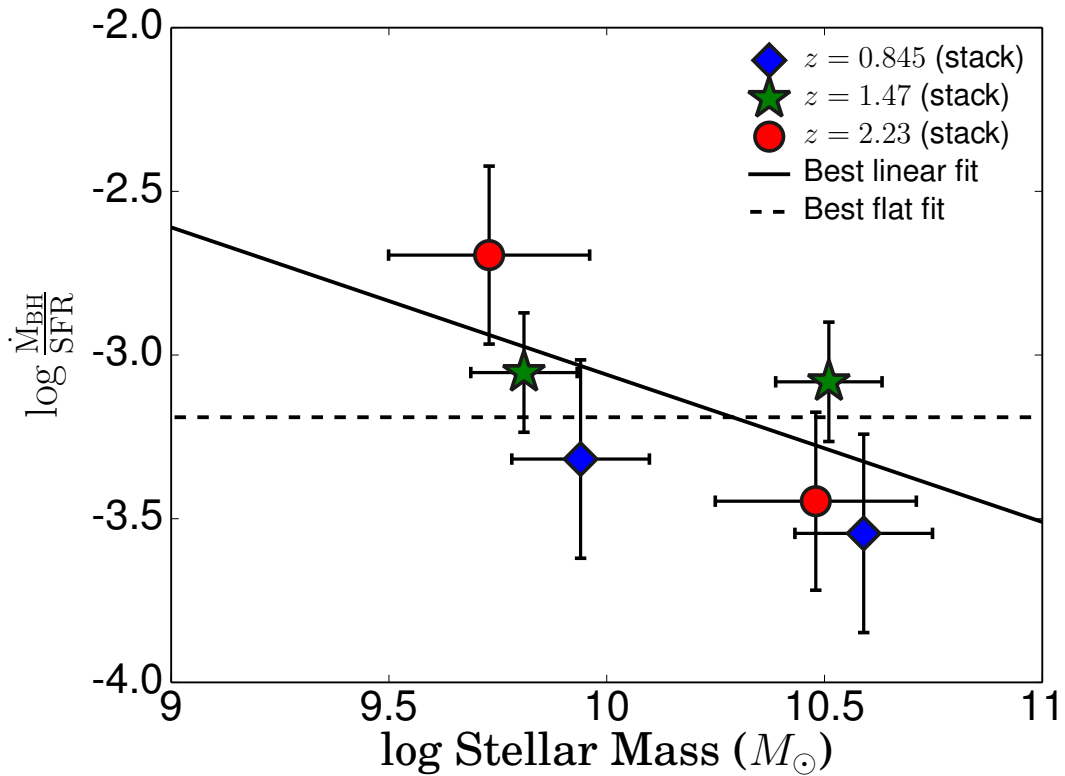


Figure 2.6: The black hole accretion rate/SFR ratio ($\dot{M}_{\text{BH}}/\text{SFR}$) vs stellar mass for typical star-forming galaxies. The $\dot{M}_{\text{BH}}/\text{SFR}$ ratio seems to generally decrease with stellar mass, indicating that more massive star-forming galaxies grow faster than their black holes compared to the least massive ones. The solid black line represents the best linear regression fit for ($\log(\dot{M}_{\text{BH}}/\text{SFR}) = -0.45 \log(M) + 1.44$; reduced $\chi^2 = 1.8$), estimated by using the PYTHON package *Scipy.optimize*. The dashed line represents the best fit for a flat relation (reduced $\chi^2 = 2.8$).

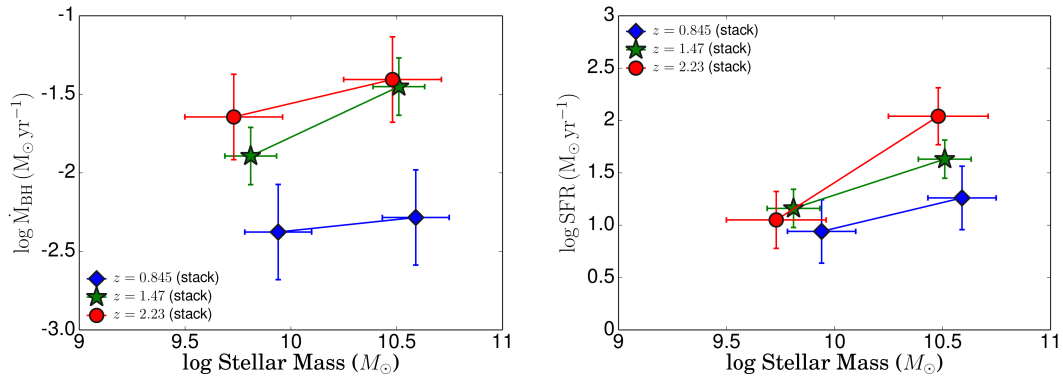


Figure 2.7: The evolution of the black hole accretion rates and star formation rates with stellar mass for each of the redshift slices in this work. The SFR grows faster than the BHAR, which results in the overall ratio decreasing with stellar mass.

Given that the peak of BH and SF activity is thought to occur at redshifts between $z \sim 1 - 2$, this constancy seems to support the idea that the central supermassive BHs and SF mechanism form a single way of regulating galaxy growth, as opposed to one mechanism taking over the other at set intervals in time. It should be noted, however, that other works, such as Kormendy & Ho (2013) and Rodighiero et al. (2015), have found a different evolution of the ratio with stellar mass with the ratio increasing with the stellar mass, with Rodighiero et al. (2015) finding that the ratio between the X-ray luminosity and SFR scales as $\log(L_X/SFR) \propto M_*^{0.43 \pm 0.09}$.

2.5.3 Relative black hole-galaxy growth and its redshift evolution

Figure 2.8 shows how the ratio between the black hole accretion rate and SFR evolves across cosmic time (see also Table 2.2). We find that the ratio between black hole and galaxy growth is very low and is surprisingly constant across redshift, $\sim 10^{-3.3}$. We thus find little to no evolution from $z = 2.23$ to $z = 0$. We investigate a potential linear fit and compare it to a flat relation (no evolution in redshift). Our results prefer a slope that is completely consistent, within less

than 1σ with a flat relation (see Figure 2.8). This is consistent with previous results: Mullaney et al. (2012b) find a flat, non-evolving relation between SFR and \dot{M}_{BH} , also maintaining a ratio of $\sim 10^{-3}$ for redshifts of $0.5 < z < 2.5$. This was interpreted as a sign that the SFR and \dot{M}_{BH} evolve equivalently throughout cosmic history, in tight relation with one another and with practically no “lag” between the two, a conclusion supported by Chen et al. (2013), who found an almost linear correlation between the \dot{M}_{BH} and SFR of star forming galaxies for redshifts $0.25 < z < 0.8$.

We can only provide lower limits for the X-ray AGN, but those provide evidence for strong scatter, likely driven by strong AGN variability. Such scatter/variability may well be higher at $z \sim 1 - 2$ than at lower redshifts. Not only is the BH more active in the X-ray AGN, with accretion rates at least an order of magnitude higher than the stacked sources (compare Tables 2.1 and 2.2), but the AGN activity itself may be having an effect on the SFR. We note that our results are consistent with those presented by Lehmer et al. (2013). The stacked sources show an accretion rate/SFR ratio typical of star forming galaxies, while the directly detected sources present a ratio in line with AGN (Figure 2.8). This is expected: throughout their lives, galaxies are thought to move above or below the local ratio depending on their AGN activity and SFR.

We note that our results do not depend on the choice of SFR indicator. Particularly, the SFRs obtained from e.g. the radio are in line with those determined with infrared luminosity ($\sim 1 M_{\odot} \text{ yr}^{-1}$ for $z = 0.4$ and $\sim 20 M_{\odot} \text{ yr}^{-1}$ for $z = 2.23$), and are also similar to those derived from $\text{H}\alpha$. However, we use FIR SFRs because they should be less affected by AGN activity than the radio (and $\text{H}\alpha$). Even though we excluded radio sources more luminous than $10^{22} \text{ W Hz}^{-1}$ (when obtaining radio SFRs), we may still get some AGN contamination. Furthermore, even though SF-related radio emission has its origins in the supernovae of massive stars (whose life-times are comparable to the duration of the star formation period), the electrons responsible for the radiation continue emitting for periods of time that reach up to ~ 100 million years after the original stars exploded. While this “persistence” of emission depends on factors like the density of the surrounding environment, it means that SFRs from the radio trace timescales that are longer than those from FIR and $\text{H}\alpha$.

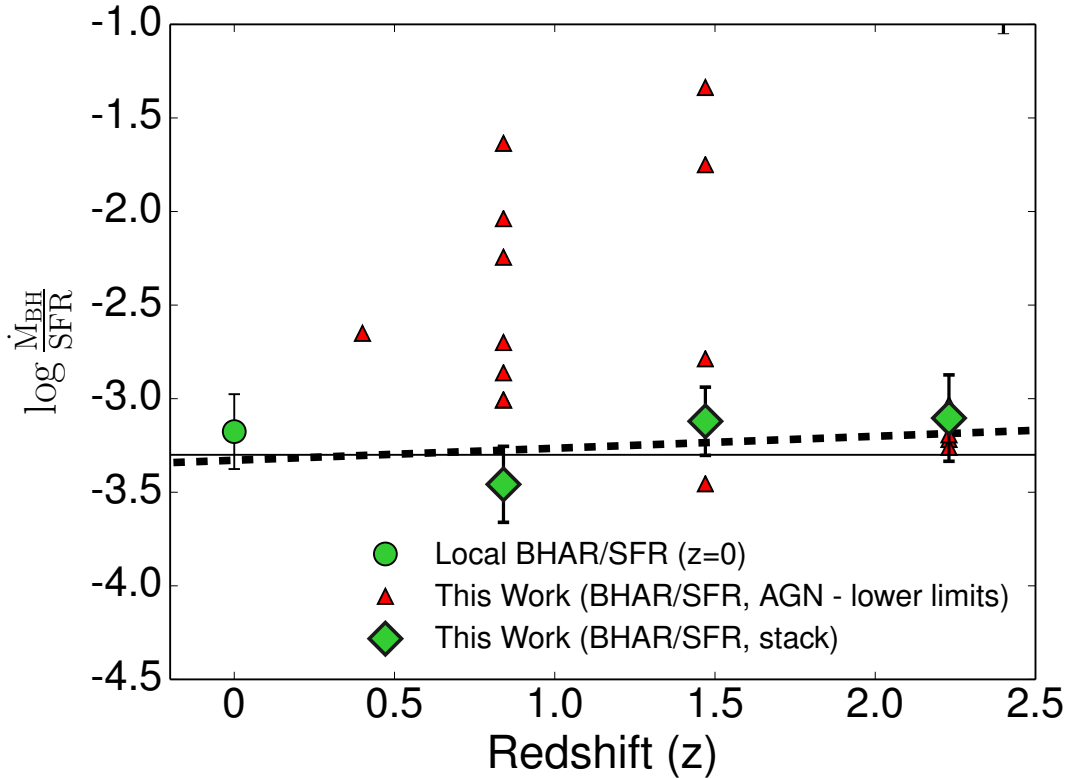


Figure 2.8: The evolution of the black hole accretion rate/SFR ratio ($\dot{M}_{\text{BH}}/\text{SFR}$) from $z = 0$ to $z = 2.23$. Our results show little to no evolution in $\dot{M}_{\text{BH}}/\text{SFR}$ over the last 11 Gyrs of cosmic time. The grey line represents a constant relation, while the dashed line is the best linear regression fit (less than 1σ away from a flat relation), estimated using *Scipy.optimize*. The ratio for the stacking remains approximately the same for all redshifts (-3.3 ± 0.2), being consistent with the measured $\dot{M}_{\text{BH}}/\text{SFR}$ value for the local Universe. This seems to show that typical star-forming galaxies form stars much faster than their BHs grow, with such difference being approximately constant across cosmic time. We also show lower limits for individual sources detected in the X-rays there; these show a large scatter with a potential peak at $z \sim 1 - 1.5$.

2.6 Conclusion

We have investigated the relative growth of H α -selected star-forming galaxies and their supermassive black holes across a redshift range of $0.4 \leq z \leq 2.23$ by making use of the HiZELS sample and the wealth of data available for the COSMOS field. We determined the black hole accretion rate of galaxies from their X-ray luminosities and their SFR from their luminosity in the far-infrared. In this manner, we were able to estimate the $\dot{M}_{\text{BH}}/\text{SFR}$ ratio for typical star-forming galaxies and how that evolves with cosmic time.

Only $\sim 3\%$ of the H α -selected star-forming population are detected in the X-rays as AGN. Our results are in line with the results from the literature: Garn et al. (2010) found that only a few per cent of the H α emitters at $z = 0.84$ are detected in the X-rays. Sobral et al. (2016) found similar results, with X-ray-detected AGN fractions that varied from 1% to 2-3% for redshifts $0.8 \leq z \leq 2.23$. Our X-ray AGN fractions are 3% for the redshifts $z = 0.4 - 1.47$ and 2% for $z = 2.23$. This implies that there is no significant evolution of the X-ray AGN fraction with redshift. Our results also complement those from Sobral et al. (2016), who estimated AGN fractions at $z = 0.84 - 2.23$ for the most luminous H α emitters and found little to no evolution with redshift.

The FIR SFRs in our sample range from $\sim 2 M_{\odot} \text{yr}^{-1}$ to $\sim 40 M_{\odot} \text{yr}^{-1}$, from $z = 0.4$ to $z = 2.23$ (Thomson et al., 2016). This is in good agreement with the H α SFRs (see e.g. Sobral et al., 2014; Swinbank et al., 2012). The \dot{M}_{BH} we obtain are generally a thousandth of the SFRs of the galaxies we studied, in line with results from Lehmer et al. (2013) for star-forming galaxies at $z = 2.23$. The black hole accretion rates rise with redshift from $\dot{M}_{\text{BH}} \sim 0.004 M_{\odot} \text{yr}^{-1}$ at $z = 0.8$ to $\dot{M}_{\text{BH}} \sim 0.03 M_{\odot} \text{yr}^{-1}$ at $z = 2.23$. The rising of the \dot{M}_{BH} may be steeper until $z = 1.47$. Interestingly, the SFRD evolves in a very similar way to the \dot{M}_{BH} , starting to stabilise at around the same redshifts: the \dot{M}_{BH} evolution starts to “flatten” at $1.47 < z < 2.23$ (e.g. Sobral et al., 2013), something that is supported in the literature, as Aird et al. (2010) has found that the peak of X-ray luminosity density is located at $z = 1.2 \pm 0.1$.

Our $\dot{M}_{\text{BH}}/\text{SFR}$ ratio is observed to have little to no evolution with redshift, being approximately $\sim 10^{-3.3}$ between $z = 0$ and $z = 2.23$. This little to no

evolution across redshift suggests that \dot{M}_{BH} and SFRs of our typical star-forming galaxies evolve at similar rates across cosmic time. Our results are thus in good agreement with the ones in the literature. Several authors have noted that the \dot{M}_{BH} and SFR ratio has been independent of cosmic time for the last ~ 10 Gyrs, with a value of $\sim 10^{-3.2}$ (see e.g. Heckman & Best, 2014; Hopkins & Beacom, 2006; Shankar et al., 2009). It is worth noting that, although our results favour a scenario where the black holes and their host galaxies grow simultaneously as a whole, they do not imply that this is necessarily the case on a galaxy by galaxy basis. Nevertheless, the little to no evolution of $\dot{M}_{\text{BH}}/\text{SFR}$ across cosmic time suggests that the processes that fuel \dot{M}_{BH} and SFR have remained the essentially the same (or correlated) over cosmic time (see, e.g. Heckman et al., 2004; Mullaney et al., 2012b). However, understanding and explaining these physical processes in detail (feedback, gas stability and availability) is still a very important open question.

We also find that $\dot{M}_{\text{BH}}/\text{SFR}$ may decline slightly with increasing stellar mass, although very weakly. This specific relation is interesting because the canonical interpretation of the influence of AGN and star formation in galaxy evolution is that AGN generally dominate in more massive galaxies whereas in less massive galaxies star formation starts playing a more important role. The fact that $\dot{M}_{\text{BH}}/\text{SFR}$ depends so little on galaxy mass could indicate that BH activity and SFR form a combined mechanism for the regulation of galaxy growth, as opposed to simply one mechanism taking over the other at set intervals in time, but this is currently very uncertain.

As for the directly detected sources in the X-rays (X-ray AGN), they show very significant scatter. They seem to deviate from the behaviour of the full population, revealing $\dot{M}_{\text{BH}}/\text{SFR}$ ratios of $> 10^{-3.5}$ to $> 10^{-1.2}$. This is not a surprising result, since AGN activity is highly variable and the BH growth may exceed SFR and vice-versa on short timescales (e.g. Alexander et al., 2008; Targett et al., 2012).

Future work would need to focus on extending this study to other surveys as well as trying to understand how SF and BH activity might constrain the evolution of the galaxies they happen in. The further use of ALMA to probe gas outflows in AGN and SF galaxies would allow us to get a much more detailed idea

of whether these processes affect galaxies differently and let us better understand how AGN and SF influence galaxy growth and themselves.

Chapter 3

The X-ray activity of typical and
luminous Ly α emitters from $z\sim 2$
to $z\sim 6$

Abstract

Despite recent progress in understanding Ly α emitters, relatively little is known regarding their typical black hole activity across cosmic time. Here, we study the X-ray properties of ~ 4000 LAEs at $2.2 < z < 6$ from the SC4K survey in the COSMOS field. By exploring deep *Chandra* Legacy data, we reach an X-ray luminosity of $\sim 10^{42.7}$ erg s $^{-1}$ for the deepest, full sample stack of ~ 480 Ms. We detect 254 ($6.8\% \pm 0.4\%$) of the LAEs individually in the X-rays ($S/N > 3$) and find an average luminosity of $10^{44.31 \pm 0.07}$ erg s $^{-1}$ and an average black hole accretion rate (BHAR) of $0.72 \pm 0.01 M_{\odot} \text{ yr}^{-1}$, consistent with moderate to high accreting AGN. We find that X-ray LAEs have a hardness ratio of ($HR = -0.1 \pm 0.2$), with half of them being consistent with obscured sources. This fraction declines with increasing X-ray luminosity, but we find no change with either Ly α luminosity or redshift. For AGN, we find that Ly α luminosities correlate with the BHARs, suggesting that Ly α luminosity becomes an accretion rate indicator. Most LAEs ($93.1\% \pm 0.6\%$) at $2 < z < 6$ have no detectable X-ray emission (BHARs $< 0.009 M_{\odot} \text{ yr}^{-1}$).

Calhau, J., Sobral, Santos, S., Matthee, J., Paulino-Afonso, A., Stroe, A., Simmons, B., Barlow-Hall, C., Adams, B., 2020, MNRAS, 493, 3

3.1 Introduction

Supermassive black holes can initially emerge from massive black hole seeds formed by the direct collapse of gas clouds (Loeb & Rasio, 1994) or from the merging of smaller black holes, produced from the first stars, which would then form a population of intermediate mass black holes (Madau & Rees, 2001; Mezcua, 2017; Mezcua et al., 2018). While accretion plays the fundamental role on the growth of black holes (e.g. Volonteri, 2012), other studies have considered the hypothesis of coalescences during galaxy mergers (Merritt & Milosavljević, 2005). Theoretically, simulations have explored the growth of black holes driven by galaxy mergers (e.g. Di Matteo et al., 2005; Hopkins et al., 2005) as well as from accretion processes (e.g. Booth & Schaye, 2009; Bower et al., 2017; Rosas-Guevara et al., 2016). Part of the problem is that most samples used in these studies are AGN-selected samples, which restricts the sources observed to the most luminous galaxies and may introduce bias against fainter populations.

Further improving our understanding using fainter populations requires large samples of galaxies across cosmic time. With respect to star forming galaxies, we can use the $H\alpha$ ($\lambda_0 = 6563 \text{ \AA}$) emission line to select large and representative samples of SFGs at $z < 2.5$ (e.g. the HiZELS survey; Sobral et al., 2013) because it is a very well calibrated star formation indicator with limited dust attenuation and traces SFRs on timescales of ~ 10 Myr (e.g. Garn et al., 2010; Kennicutt, 1998; Oteo et al., 2015; Sobral et al., 2012). At $z > 2.5$, $H\alpha$ becomes unobservable from the ground, due to the line shifting into the mid-infrared, but $Ly\alpha$ ($\lambda_0 = 1216 \text{ \AA}$) may be used as an alternative for tracing both star formation and BH activity (e.g. Ono et al., 2012; Sobral & Matthee, 2019; Sobral et al., 2017; Stark et al., 2015). It is usually associated with SF and early “primeval” galaxies (e.g. Cowie & Hu, 1998; Pirzkal et al., 2007; Pritchet, 1994), although it can also originate from AGN activity (e.g. Gawiser et al., 2006; Ouchi et al., 2008; Sobral et al., 2018b; Wold et al., 2014, 2017). Furthermore, at $2 < z < 7$, the $Ly\alpha$ line is redshifted into the optical band, making it easy to be observed from the ground.

In order to make progress we require a large sample of LAEs selected across redshift and with access to the deepest data from the X-ray band. In this Chapter we make use of the public SC4K survey (Sobral et al., 2018a) to study the X-ray

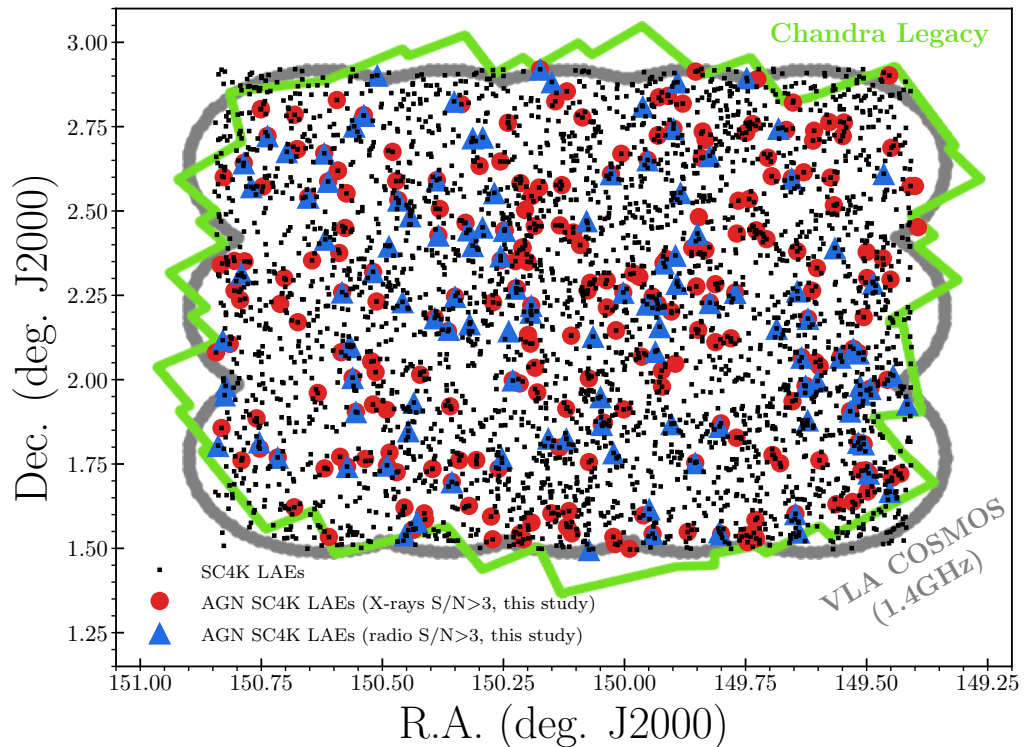


Figure 3.1: The distribution of the SC4K LAEs (Sobral et al., 2018a) across the COSMOS field (black markers). We consider only the sources covered by *Chandra* COSMOS Legacy (Civano et al., 2016, green line), for a total of 3700 sources. The red circles and blue triangles show the LAEs that are directly detected in the X-rays or radio, respectively. The grey boundary illustrates the area of the VLA-COSMOS 1.4 GHz survey (Schinnerer et al., 2004), which we also use. The HeRMES survey (*Herschel* space telescope, 100, 160, 250, 350 and 500 μm - Griffin et al., 2010; Oliver et al., 2012) and the VLA COSMOS 3 GHz survey (Smolčić et al., 2017) cover the totality of SC4K.

properties of roughly 4000 LAEs at $2 < z < 6$ in the COSMOS field. Using stacking analysis to probe beyond the current limits, we reach an equivalent total exposure time of 482 Ms (~ 15 yrs) in the X-rays to characterise the AGN activity of LAEs.

3.2 Data and sample

3.2.1 The sample of Ly α emitters at $z = 2.2 - 5.8$

We use a large sample of LAEs selected over a redshift range of $z \sim 2 - 6$ in the COSMOS field (SC4K; Sobral et al., 2018a). SC4K also includes the CALYMHA COSMOS sample at $z = 2.2$ (Sobral et al., 2017), with H α coverage from HiZELS (Geach et al., 2008; Sobral et al., 2009a, 2013). The LAEs were detected using a compilation of 16 narrow and medium band data taken with the Subaru and the Isaac Newton Telescopes. Sources were selected as LAEs through a combination of photometric and spectroscopic redshifts as well as colour-colour diagnostics. Briefly, a LAE satisfies all the following conditions (see Sections 1.1.5 and 1.1.6 for more details on the selection techniques):

1. Significant excess in a medium (narrow) band, with an $EW_0 > 50(25) \text{ \AA}$ (the majority of LAEs come from MB samples);
2. Presence of a Lyman break in rest-frame wavelengths blue-ward of the identified emission line;
3. A colour cut to exclude dusty lower redshift sources.

The resulting sample has 3908 LAEs with an average luminosity of $L_{\text{Ly}\alpha} \sim 10^{42.9} \text{ erg s}^{-1}$ ($\approx L_{\text{Ly}\alpha}^*$), over a volume of $\sim 6 \times 10^7 \text{ Mpc}^3$. We refer to Sobral et al. (2018a) for the full selection criteria and further details regarding the SC4K LAEs. Further information regarding the rest-frame UV morphologies and sizes of SC4K LAEs can be found in Paulino-Afonso et al. (2018) and Shibuya et al. (2019), while the clustering properties of LAEs and their dependencies on Ly α and SFRs have been extensively studied by Khostovan et al. (2019).

Figure 3.1 shows the on-sky distribution of SC4K LAEs in the COSMOS field. We also show the coverage of the *Chandra* COSMOS Legacy Survey (Civano et al., 2016) and the VLA COSMOS surveys (Schinnerer et al., 2004; Smolčić et al., 2017). Note that some SC4K LAEs fall outside the coverage of the *Chandra* COSMOS Legacy Survey and we further exclude 5 sources for being too close to the edge of the field, so we use a total of 3700 sources. This constitutes our sample of LAEs.

3.2.2 X-ray data: *Chandra* COSMOS-Legacy

The *Chandra* COSMOS-Legacy survey (Civano et al., 2016; Elvis et al., 2009) covers the COSMOS field (e.g. Capak et al., 2007; Scoville et al., 2007) over a total area of 2.2 deg². The survey has an exposure time of 150 ks px⁻¹ in the central 1.5 deg² and between 50 ks px⁻¹ to 100 ks px⁻¹ in the external regions. The average flux limit of the survey, as defined by the source catalogue (Civano et al., 2016) is 8.9×10^{-16} erg s⁻¹ cm⁻² for the full band (0.5 – 7 keV), 2.2×10^{-16} erg s⁻¹ cm⁻² for the soft band (0.5 – 2 keV) and 1.5×10^{-15} erg s⁻¹ cm⁻² for the hard band (2 – 7 keV).

Figure 3.1 shows an illustration of the regions covered by each of the surveys used in this work and the sources classified as X-ray AGN, in comparison to SC4K. The deep X-ray data allow us to track X-ray emission from processes like Bremsstrahlung and inverse-Compton scattering¹, and thus to identify AGN X-ray emission.

3.3 Methodology

Here we present the full methodology leading to all the quantities that are explored in this chapter. These include X-ray derived properties.

¹Mainly inverse-Compton scattering, as thermal emission becomes negligible at higher redshifts, (see Lehmer et al., 2016).

3.3.1 X-ray analysis

X-rays are one of the most efficient ways to probe the activity of black holes because they track the accretion of matter into the BH directly from the photons emitted through inverse Compton effect on the accretion disk (Haardt & Maraschi, 1991). Because of this, we expect X-ray luminosity to scale with the BHAR and use it to not only identify AGN, but also to estimate the growth rate of the supermassive black hole.

3.3.1.1 Source detection

For our X-ray analysis, we make use of the data from the *Chandra* Legacy Survey (Civano et al., 2016), which builds upon the C-COSMOS survey (Elvis et al., 2009). We bin the original science images (pixel scale of $0.5''\text{px}^{-1}$) by a factor of 2 and use the corresponding exposure maps. We obtain cut-outs of 100×100 px for both the X-ray and exposure maps centred on the 3700 LAEs and mask pixels with 0 exposure times, before transforming the image to counts/s. In this study we use apertures with a diameter of 8 px ($\sim 7.9''$), centred on the position of each LAE. This aperture allows us to extract roughly the full fluxes of most sources ($\sim 80\%$ - see Civano et al., 2016) in the COSMOS-Legacy survey without adding significant noise to the measurements. Nevertheless, we apply a final (small) aperture correction to assure we recover the full fluxes (see Section 3.3.1.3).

3.3.1.2 Background and net count estimation

To determine the background counts, we randomly place $7.9''$ apertures, while ignoring the central area and image borders. We restrict the placement of empty 8 px apertures to a region of 100×100 px around each LAE rather than the entire *Chandra* image in order measure the local noise and background. The counts/s in each of the individual apertures sampling the background are summed and the median of 2000 apertures is taken as the background value for each source. This background value is then subtracted from the source's net count.

The uncertainty is measured by taking asymmetric errors. We define the upper and lower errors as the 84th and 16th percentile of the backgrounds, respectively.

The signal to noise ratio (S/N) is defined as the ratio between the net counts/s and the lower error of each image. A source is considered detected if its signal-to-noise rises above or equals 3, but we also define S/N cuts of 5 and compare with the higher significance catalogue provided by Civano et al. (2016).

3.3.1.3 X-ray Flux estimation

We convert our counts/s into flux by using the method detailed in Elvis et al. (2009) and Civano et al. (2016). To this effect, we multiply our normalised count rates by a conversion factor (CF) and divide the result by a factor of 10^{11} :

$$F_{X_0} = (\text{counts/s}) \times \text{CF} \times 10^{-11} \text{ (erg s}^{-1} \text{ cm}^{-2}\text{)} \quad (3.1)$$

In our study, we take the average of the conversion factors between the two *Chandra* COSMOS surveys, C-COSMOS (Elvis et al., 2009) and *Chandra* Legacy (see Civano et al., 2016), resulting in conversion factors of 0.687, 3.05 and 1.64 for our Soft, Hard and Full band CFs, assuming a photon index $\Gamma = 1.4$. The noise values are converted in the same way. Note that the correction factors for C-COSMOS we use are corrected values (see Civano et al., 2016).

We compare our aperture fluxes F_{X_0} with the full fluxes F_C obtained by Civano et al. (2016) by matching them using a $1''$ matching radius and calculate an aperture correction as the median of the flux difference in log space¹. This allows us to define a median aperture correction from our fluxes to full fluxes². We define our full flux, F_X , aperture corrected to match Civano et al. (2016), as:

$$\log_{10}(F_X) = \log_{10}(F_{X_0}) + A_C \quad (3.2)$$

We find $A_C = 0.1$, which we apply throughout this paper. The matched Civano et al. (2016) fluxes show a median error of $8.1 \times 10^{-16} \text{ erg s}^{-1}$, in the full band, and the individual errors vary across the *Chandra* Legacy field, with no apparent trend. Our aperture-corrected flux errors for the matched sources, taken as the

¹ $A_C = \text{median}[\log_{10}(F_C) - \log_{10}(F_{X_0})]$, see also Figure 3.2.

²We also do a linear fit to the difference between F_{X_0} and F_C , before correcting our fluxes, and find that the slope is close to zero (-0.01).

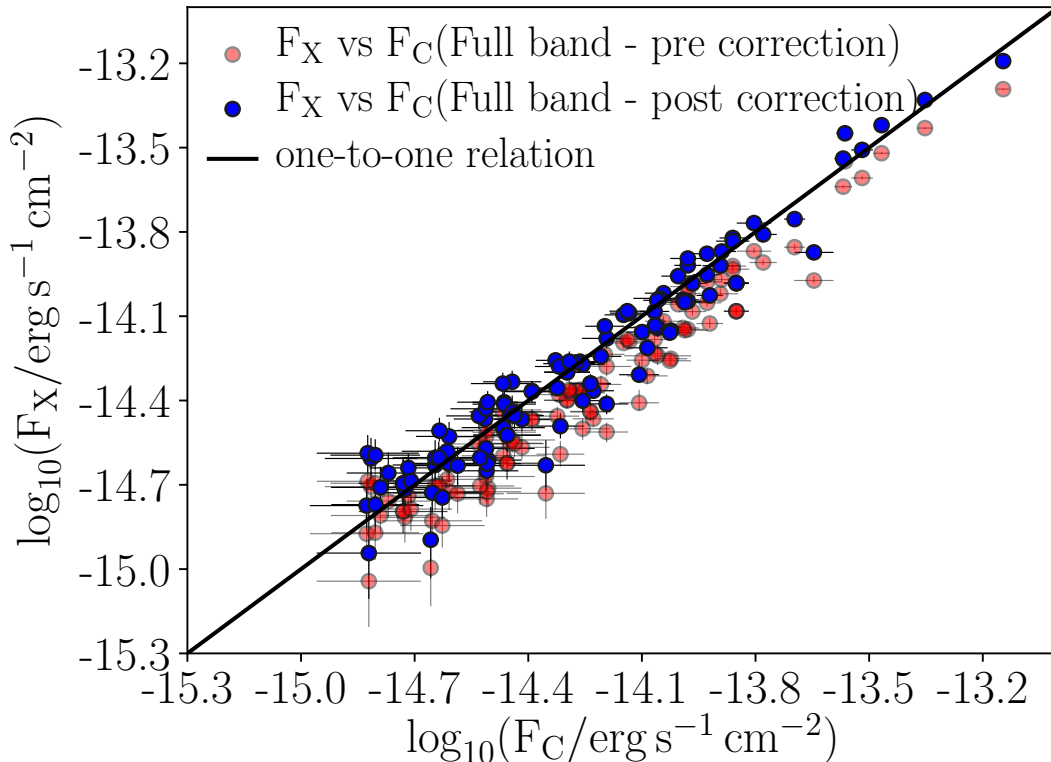


Figure 3.2: Comparison between the X-ray fluxes obtained in this work (F_X) and the ones reported by Civano et al. (2016) (F_C), for the full band (0.5-7 keV) of *Chandra*. As expected, our initial aperture fluxes consistently underestimate the X-ray fluxes. After applying a median correction, we successfully recover the fluxes of Civano et al. (2016) on average.

84th and 16th percentile of the background measurements, have a median of $3.1 \times 10^{-16} \text{ erg s}^{-1}$ but get greater as the sources approach the edges of the Chandra Legacy field, following the trend set by the exposure maps and in some of the more extreme cases reaching errors of the order of $10^{-15} \text{ erg s}^{-1}$. Figure 3.2 shows the comparison between our initial aperture fluxes and the aperture corrected ones when compared to Civano et al. (2016), showing an excellent agreement.

Using just the Civano et al. (2016)’s catalogue would be an alternative of looking at the questions explored by this work (which we also take), and we show that our results are unchanged in a qualitative way. However, since in this study we have a pre-selected sample of sources (LAEs), and because stacking is

crucial to try to unveil any fainter X-ray emission statistically, it is crucial that the individual detections and the stacking methodology are self-consistent. In our analysis we make sure that i) we can reproduce the robust fluxes of Civano et al. (2016) and ii) we apply a methodology that is easily transferrable to our stacking analysis in a self-consistent way and that allows us to go to a lower S/N.

3.3.1.4 Hardness ratio estimation

Soft band photons are the first of the X-ray photons to be absorbed by the environment surrounding the SMBH. We illustrate this in Figure 1.1, where we show the spectrum of an AGN observed through a column density of $N_{\text{H}} \sim 10^{21} \text{ cm}^{-2}$ and the emission of hard X-ray photons, from inverse Compton scattering or synchrotron radiation, with no absorption. As the column density increases, the spectrum of the AGN gets increasingly absorbed, starting with the photons from the soft band (0.5-2 keV), which translates into a lower count rate for this band. Comparing the count rates of both the soft and the hard band gives us a measurement of the level of obscuration of an AGN (see, e.g., Park et al., 2006). We achieve this by estimating the hardness ratio of the AGN. In this endeavour we restrict ourselves to sources detected in both the soft and hard band. In order to estimate the hardness ratio of our sources, we adopt the standard definition (see Park et al., 2006, for a discussion on the various definitions of the hardness ratio):

$$HR = \frac{H - S}{H + S} \quad (3.3)$$

where HR is the hardness ratio of a source and H and S are the count rates (counts/s, in 7.9" apertures) in the hard (2-7 keV) and soft band (0.5-2 keV), respectively. We caution that the requirement of both soft and hard band detections for the determination of the hardness ratio may bias us towards more obscure sources, in a low count scenario.

3.3.1.5 X-ray luminosity estimation

We convert the fluxes to observed X-ray luminosity by using

$$L_X = 4\pi(F_X)d_L^2 \text{ (erg s}^{-1}\text{)} \quad (3.4)$$

where d_L is the luminosity distance in cm. We determine the luminosity distance by taking the redshift associated with the narrow or medium band filter the source is detected with. We do this for both the individual sources and while stacking.

We convert the observed luminosity in each band into the rest-frame 0.5 – 10 keV luminosity by multiplying the observed luminosity by a K-correction factor as defined in Marchesi et al. (2016b), resulting in the expression:

$$L_{0.5-10 \text{ keV}} = \frac{L_X(10^{(2-\Gamma)} - 0.5^{(2-\Gamma)})}{(E_{\text{max}}(1+z))^{(2-\Gamma)} - (E_{\text{min}}(1+z))^{(2-\Gamma)}} \quad (3.5)$$

where E_{max} and E_{min} are the maximum and minimum energies for the band used, z is the redshift and Γ is the photon index, assumed to be 1.4. This is the value for the background X-ray slope and is a good average slope for populations containing both obscured and unobscured AGN (assuming Galactic absorption, see Markevitch et al., 2003). It is also a good value for star-forming galaxies (not expected to have strong X-ray emission, see Alexander et al., 2003). We do not correct for absorption at the source since the vast majority of SC4K LAEs are not detected in the X-rays and we have no way of determining their intrinsic absorption. For the sources that are detected in both bands we estimate an average $\text{HR} \sim -0.1$, which translates into an absorption of $1.7 \times 10^{23} \text{ cm}^{-2}$ and a correction of 0.7 to the full band X-ray log scale luminosity. We therefore caution that some X-ray luminosities and BHAR may be underestimated due to their sources being obscured.

3.3.1.6 Black Hole Accretion Rates

In order to determine the BHARs of our sources, we start by translating our 0.5 – 10 keV luminosities into bolometric luminosities by taking:

$$L_{\text{bol}} = 22.4 \times L_{0.5-10 \text{ keV}} \quad (3.6)$$

Where 22.4 is the bolometric correction factor. Vasudevan & Fabian (2007) find that the bolometric correction varies with the Eddington ratio of the sources, going from 15 – 25 for AGN with Eddington ratios of <0.1 and 40 – 70 for AGN with higher ratios. Given the high variability of the bolometric corrections, we follow Lehmer et al. (2013) and assume the median value of 22.4 for the bolometric correction of AGN of $L_X = 10^{41} - 10^{46} \text{ erg s}^{-1}$. We then estimate the BHAR from our bolometric luminosities using:

$$\dot{M}_{\text{BH}} = \frac{L_{\text{bol}}(1 - \epsilon)}{\epsilon c^2} \times 1.59 \times 10^{-26} (\text{M}_{\odot} \text{ yr}^{-1}) \quad (3.7)$$

where \dot{M}_{BH} is the BHAR, ϵ is the accretion efficiency, assumed to be 0.1 (see Marconi et al., 2004, for motivation) and c is the speed of light. We stress that we are assuming a median value of 22.4 for the bolometric correction, but the actual value is uncertain and may vary. Varying the bolometric correction between 15 and 50 results in an uncertainty of the BHAR of the order of ${}^{+0.5}_{-0.03} \text{ M}_{\odot} \text{ yr}^{-1}$ and adding it in quadrature would provide a more conservative error estimation. However we adopt the median value for simplicity.

3.3.1.7 Stacking

Apart from studying the individual sources, we also obtain stacks of LAEs in the X-rays. In order to do so we first stack the cut-outs in count/s, using median and average statistics, before following the same procedure as for the individual sources. This includes applying the correction to the fluxes estimated from our comparison with (Civano et al., 2016, see Section 3.3.1.3). This means if we stack the individual detections we recover the average (median) fluxes of Civano et al. (2016) catalogue within 0.01 (0.03) dex. We calculate the median of the redshifts of the sources used in the stacks and take it as the redshift associated with that stack, effectively treating all sources in a stack as having that same redshift. We also take the 16th and 84th percentiles as the errors associated with the redshift, where applicable. The median redshifts are then used to estimate the luminosity distances used when calculating the X-ray luminosities of the stacks.

We stack our sources based on different redshift and Ly α luminosity bins (see Table A.5). We also stack the full sample, both while including and excluding the AGN candidates.

3.3.1.8 SFR contribution to the X-ray emission

X-rays can also track SFR due to emission from supernova remnants, high mass X-ray binaries (see e.g. Figure 1.1) and hot plasma (see, e.g. Fabbiano, 1989; Ranalli et al., 2003). We estimate X-ray luminosity (L_X ; erg s^{-1}) produced by several processes associated with star formation by using the relation¹ derived by Lehmer et al. (2016) for SFGs galaxies at $0 < z < 7$ (converted to a Chabrier IMF):

$$\log_{10}(L_X) = 39.82 + 0.63 \log_{10}(\text{SFR}) + 1.31 \log_{10}(1 + z) \quad (3.8)$$

where SFR is in $M_\odot \text{ yr}^{-1}$ and L_X is rest-framed and in erg s^{-1} . The dependence on redshift is due to the evolution of the contribution to X-ray luminosity by X-ray binaries (see Lehmer et al., 2016, and references therein). It should be noted that the relation is expected to overestimate the X-ray luminosity of sources with $\text{SFR} < 10 M_\odot \text{ yr}^{-1}$ (Lehmer et al., 2016). Equation 3.8 implies that for the redshift range of SC4K LAEs ($2 < z < 6$) and SFRs as low as $\sim 5 M_\odot \text{ yr}^{-1}$ we expect $L_X \sim 10^{41} \text{ erg s}^{-1}$. Only SFRs of $\sim 1000 M_\odot \text{ yr}^{-1}$ or higher can reach $L_X \sim 10^{42} \text{ erg s}^{-1}$, justifying the commonly used X-ray luminosity above which AGN dominate the emission.

3.4 The X-ray properties of LAEs at $2 < z < 6$

Using the method detailed in Section 3.3.1 we find a total of 254 (7%) LAEs which are directly detected in the *Chandra* full band (0.5 – 7.0 KeV) with $\text{S/N} > 3$ (see e.g. Figure 3.3). Of these detections, 165 have S/N equal or higher than 5. The majority (89.4% \pm 2.3%) of the X-ray LAEs are detected at $z < 3.5$. Our

¹The relation is given by $\log_{10}(L_X) = A + B \log_{10}(\text{SFR}) + C \log_{10}(1 + z)$, and we use A, B and C with values 39.82 ± 0.05 , 0.63 ± 0.04 and 1.31 ± 0.11 .

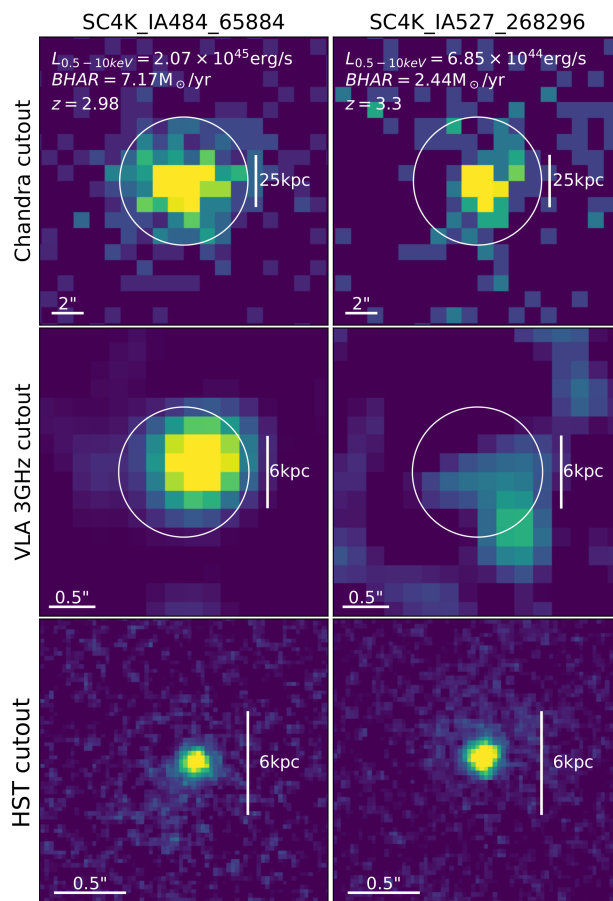


Figure 3.3: Two X-ray detected LAEs: SC4K-IA427-65884 (left, $z = 2.98$) and SC4K-IA484-268296 (right, $z = 3.3$). The two sources have high X-ray luminosities, implying BHARs of $\sim 7 M_{\odot} \text{ yr}^{-1}$ and $\sim 2 M_{\odot} \text{ yr}^{-1}$, respectively. Both present point-like X-ray emission. The circles represent the apertures used for determining the fluxes. The second row of images shows the VLA 3 GHz cut-outs for the sources, showing that only one of these LAEs is significantly detected in the radio. The third row shows the *HST* F814W filter cut-outs for the respective sources, revealing very compact rest-frame UV morphologies (see also Paulino-Afonso et al., 2018).

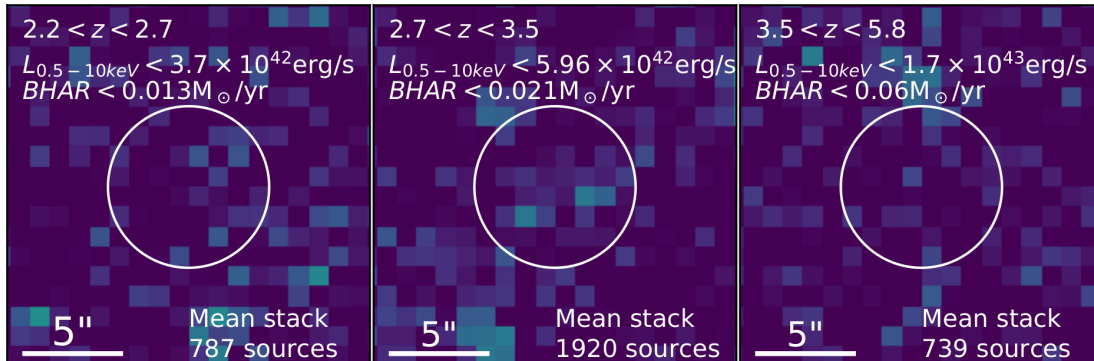


Figure 3.4: The results of mean stacking LAEs in the X-rays in 3 different redshift groups, excluding all LAEs that are individually detected in the X-rays ($S/N > 3$). No X-ray emission is detected in any of these stacks and we are only able to provide upper limits for the luminosity and BHARs.

detections have moderate to high X-ray luminosity ($L_{0.5-10\text{keV}} = 10^{43-45} \text{ erg s}^{-1}$) with an average luminosity of $10^{44.07 \pm 0.01} \text{ erg s}^{-1}$ (see Figure 3.3).

Stacking in bins of $\text{Ly}\alpha$ luminosity (including X-ray detected sources) results in robust detections for the vast majority of the bins, translating into X-ray luminosities ranging from $L_{0.5-10\text{keV}} \sim 10^{42.9} \text{ erg s}^{-1}$ to $\sim 10^{44.2} \text{ erg s}^{-1}$. On the other hand, stacking by excluding X-ray sources produces no detections in general (see Figure 3.4 and table A.5). This result is the same if we only take out the sources from Civano et al. (2016), but some of the stacks (e.g. $z = 2.9$, $z = 3.7$) yield tentative detections with $S/N \sim 2$ and a X-ray luminosity of $\sim 10^{42.7} \text{ erg s}^{-1}$. Furthermore, we note that if we only exclude the sources from Civano et al. (2016), we get significant detections for the X-ray stacks of the most luminous LAEs with luminosities $L_{\text{Ly}\alpha} > 10^{43.3} \text{ erg s}^{-1}$. This is because at the highest $\text{Ly}\alpha$ luminosities there are still a significant number of X-ray sources individually detected at $S/N \sim 3-5$ which are not in the high significance Civano et al. (2016) X-ray selected catalogue.

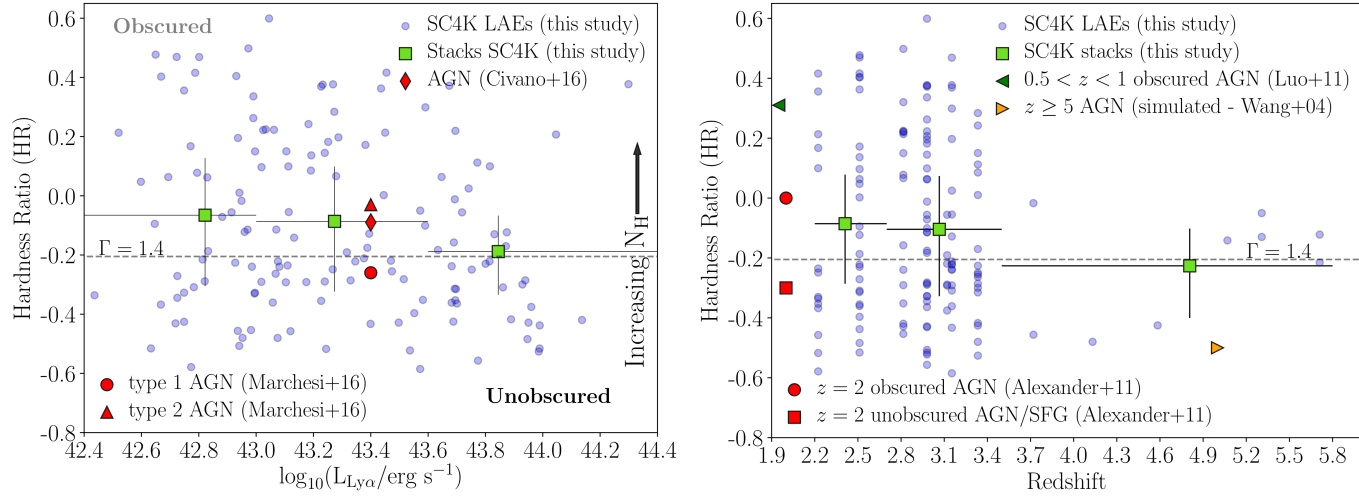


Figure 3.5: The X-ray hardness ratio (HR) of our X-ray AGN LAEs. For our analysis we only use sources detected in both the soft and hard band ($S/N > 3$), for a total of 143 LAEs. The HR errorbars represent the 68% confidence on the HR measurements. The $\text{Ly}\alpha$ (horizontal) errorbars illustrate the size of the bins used. We find no significant relation between the HR and $\text{Ly}\alpha$ luminosity or redshift, with roughly half the sources having $\text{HR} > -0.2$ and therefore consistent with being significantly obscured. The grey line represents the typical HR limit for obscured AGN with $\Gamma = 1.4$ (see also Mezcua et al., 2018). Also shown are the HRs for the samples of Civano et al. (2016) and Marchesi et al. (2016a) (Left panel) and Wang et al. (2004b) ($z \geq 5$ AGN), Alexander et al. (2011) (obscured AGN and unobscured AGN/SFG) and Luo et al. (2011) (obscured AGN - Right panel). We place literature measurements at their reported redshifts and arbitrarily place measurements at a $\text{Ly}\alpha$ luminosity of $\sim 10^{43.4} \text{ erg s}^{-1}$ for illustrative purposes. Our results reveal that X-ray LAEs seem to be representative of the full X-ray selected population.

3.4.1 The hardness ratio of X-ray LAEs

Of the 254 X-ray LAEs, 143 are detected in both hard (2.0 – 7.0 keV) and soft (0.5 – 2.0 keV) bands individually at $S/N > 3$. As a whole, these 143 LAEs have an average HR of $-0.1^{+0.21}_{-0.17}$ (errors estimated by taking the 68% confidence region). As Figure 3.5 shows, approximately 48% (69 out of 143) of our LAEs can be classed as unobscured as they have a low hardness ratio of $HR < -0.2$. We find no significant relation between HR and $\text{Ly}\alpha$ luminosity or redshift (see Figure 3.5), although there may be a weak trend of lower HR at the highest $\text{Ly}\alpha$ luminosities and at the highest redshifts. Our results are therefore consistent with X-ray LAEs having similar column densities/obscuration at a range of $\text{Ly}\alpha$ luminosities and across redshift.

We compare our results for X-ray detected LAEs with those based on X-ray selected sources at similar redshifts. As Figure 3.5 shows, X-ray LAEs show similar hardness ratios to those reported for the global X-ray AGN population (Civano et al., 2016), where the average HR is ≈ -0.11 . Interestingly, Civano et al. (2016) reports that the overall population of X-ray AGN in COSMOS is best described by a double gaussian peaking at $HR = -0.31$ and $HR = 0.12$. Such values could be interpreted as the result of two different X-ray AGN populations, one unobscured and one obscured, as shown by Marchesi et al. (2016a). We find no significant evidence of the presence of a double peak in the distribution for the X-ray LAEs, although this is possibly due to the sample being much smaller than the full X-ray AGN sample in COSMOS, particularly towards higher redshifts.

In Figure 3.6 we present how the X-ray hardness ratio may depend on X-ray luminosity for LAEs. We find a significant correlation between the HR and X-ray luminosity, which implies that X-ray LAEs with higher X-ray luminosity have generally lower HR and likely lower column densities/less obscuration. This trend is very similar to what has been found by Marchesi et al. (2016b) for the entire sample of X-ray AGN. Specifically, Marchesi et al. (2016b) found that 80% of the X-ray sources in COSMOS with $L_X < 10^{43} \text{ erg s}^{-1}$ are likely obscured AGN, while such fraction declines to $\sim 20\%$ at $L_X > 10^{44} \text{ erg s}^{-1}$. This trend has also been observed in several other studies (e.g. Hasinger, 2008; Lawrence & Elvis, 1982; Merloni et al., 2014), for populations with obscuration determined both optically

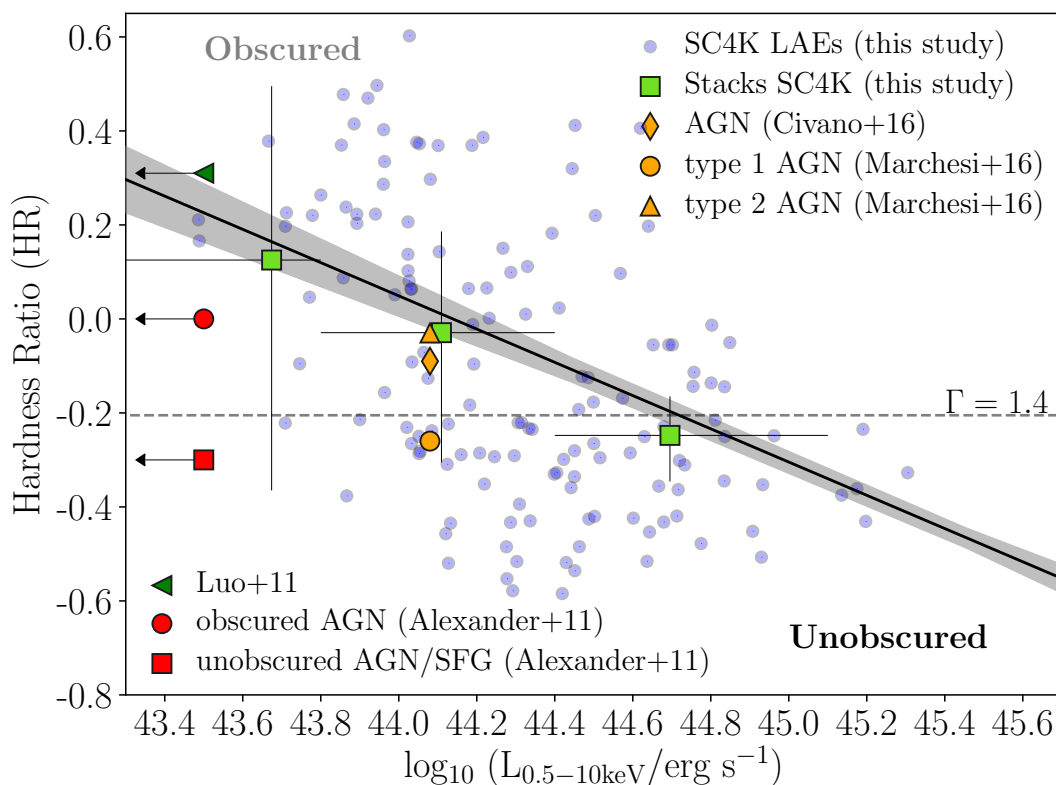


Figure 3.6: The X-ray hardness ratio (HR) of our X-ray AGN LAEs as a function of their X-ray luminosity. The vertical errorbars are the 68% confidence on the HR measurements. The X-ray luminosity (horizontal) errorbars illustrate the size of the bins used. A statistically significant correlation is observed (estimated through a linear regression fit with `Scipy.optimize`), with the more luminous X-ray LAEs having lower HR. The shaded region represents the 68% confidence interval, which clearly dismisses the possibility of the presence of a flat relation. This can be interpreted as lower column densities for the LAEs with the highest observed X-ray luminosities, while the lowest X-ray luminosity sources seem to be predominantly highly obscured. For comparison, we show the results by Alexander et al. (2011) (obscured AGN and unobscured AGN/SFG) and Luo et al. (2011) (obscured AGN) for different X-ray luminosities.

and through X-rays (but see e.g. Lusso et al., 2013), so our results seem to indicate that AGN LAEs follow the trend set by the general X-ray AGN population. Nevertheless, it is worth noting that our results may be biased towards high HR values at lower X-ray luminosities, due to requiring detections in both bands to determine the HR. As can be seen in Figure 3.6, the decrease of HR with X-ray luminosity is much milder above $\sim 10^{44}$ erg s $^{-1}$, where in principle we are much more complete to the full range of sources regardless of their obscuration.

3.4.2 X-ray luminosity of LAEs as a function of redshift

In Figure 3.7 we show the X-ray luminosities of the X-ray detected LAEs as a function of redshift. The black line in Figure 3.7 represents the X-ray luminosity for the 3σ limit in our study. The range of X-ray luminosities is relatively wide, particularly at $2 < z < 3$. Most X-ray LAE AGN in our sample have luminosities $L_X \sim 10^{43-45}$ erg s $^{-1}$. In general, our X-ray LAEs fall within the expected luminosities for moderate to powerful AGN at similar redshifts (see Brandt & Alexander, 2015, and references therein). The X-ray luminosity ranges of the AGN LAEs also correspond to high to moderate BHARs, with the highest being $\sim 4.2 M_\odot \text{ yr}^{-1}$ and the lowest $\sim 0.04 M_\odot \text{ yr}^{-1}$ (see Table A.1 for the full description of our X-ray AGN candidates' properties).

We find a significant number of X-ray LAEs below $z \sim 3.5$, but the number of such sources drops sharply for higher redshifts. This is partly explained by the number of LAEs at high redshift being lower than at $z < 3.5$ in SC4K and the fact that the X-ray luminosity limit rises, but those alone are not the full explanation (see Section 5.4.2). Interestingly, the low number of X-ray LAEs is quite striking when using the high significance X-ray selected catalogue of Civano et al. (2016), where only 3 X-ray LAEs in a total of 766 are found at $z > 3.5$. However, when we go down in S/N we find a significantly larger number of X-ray LAEs at high redshift, as can be seen in Figure 3.7, much closer to the detection limit.

The observed low number of X-ray LAEs detected at high redshift (particularly using Civano et al. 2016) is in agreement with the literature. Wang et al. (2004a), for example, studied ~ 400 LAEs at $z \sim 4.5$ (101 of which had *Chandra*

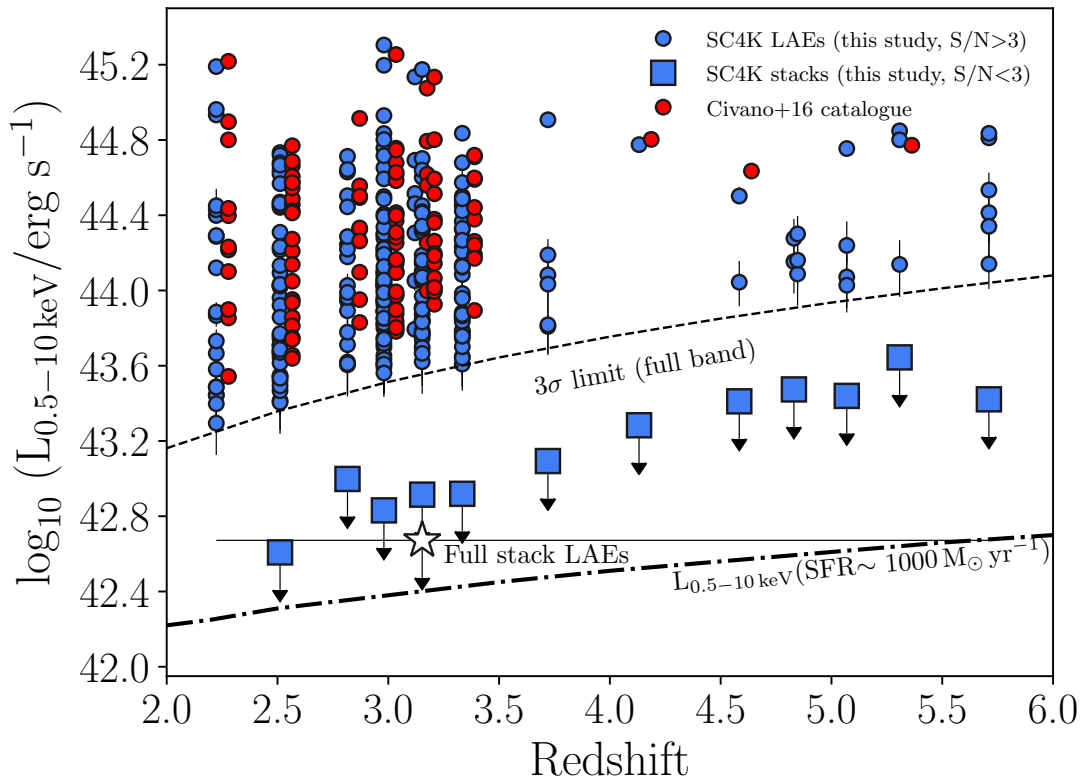


Figure 3.7: The X-ray luminosity of all our X-ray LAEs against redshift. Stacking by excluding X-ray LAEs results in non-detections in the X-rays for all redshifts (blue squares) including the full stack (white star), which supports most non-X-ray LAEs having very low accretion rates. The black dashed line indicates the 3σ luminosity detection limit used in this work. X-ray LAEs are marked by blue circles. Sources detected in the *Chandra* COSMOS-Legacy catalogue are represented by red circles, with the luminosities from Civano et al. (2016). Errors were estimated by taking the 68% confidence interval, as explained in Section 3.3.1 We apply a slight horizontal shift of $+0.06$ to the AGN markers from Civano et al. (2016) in order to facilitate inspection. The difference in the number of sources is due to the higher signal-to-noise limit used by Civano et al. (2016) of $\sim 5\sigma$ and the different extraction methods used. We also show the luminosity limit above which AGN start to dominate the X-ray emission (dot-dashed line). This is because SFRs of $\sim 1000 M_{\odot} \text{ yr}^{-1}$ are required (Lehmer et al., 2016) to achieve such X-ray luminosity. Most importantly, a SFR of $\sim 5 M_{\odot} \text{ yr}^{-1}$ (more typical of LAEs) should lead to a X-ray luminosity of just $L_X \sim 10^{41} \text{ erg s}^{-1}$ (see Section 3.3.1.8 and Lehmer et al., 2016), significantly below the stacking limits.

coverage) and found no significant X-ray emission, which the authors interpreted as evidence for a lack of AGN in LAEs at that redshift. In comparison, in our study we find only 27 (0.7% of the total SC4K sample) LAEs with X-ray emission at $z > 4$. In order to check the consistency of our results, we conducted a jackknifing test by randomly selecting 101 galaxies from our $z > 4$ LAE sample and checking how many of those galaxies are detected in the X-rays. By repeating this resampling 10000 times we obtain a distribution in which the event of finding 0 X-ray detected LAEs (AGN) is at $\sim 1.8\sigma$ of the mean. It is therefore possible that the low number of LAEs in Wang et al. (2004a) combined with their low luminosity, was simply not enough to allow for the detection of X-ray LAEs. Fortunately, the SC4K sample of LAEs in COSMOS is finally large enough to find these rare sources even at high redshift, for the first time.

To further investigate the relative lack of X-ray detections at high redshift and any potential evolution in the population, we set up a test where we randomly picked a LAE at lower redshift ($z = 2.2 - 3.5$) and shifted it towards the higher redshifts ($z = 3.5 - 5.8$). We make sure we mimic the selection limits at higher redshift by e.g. selecting LAEs at $z \sim 2 - 3$ with $L_{\text{Ly}\alpha} > 10^{43} \text{ erg s}^{-1}$, the typical luminosity limit at higher redshift. We then find that the X-ray luminosities for the shifted sources that are detectable in *Chandra* would be expected to have $L_X = 10^{43.7-44.6} \text{ erg s}^{-1}$, which is consistent with what we observe in the actual sample with our analysis. However, if the X-ray AGN fraction remained constant we would expect to have found many more X-ray LAEs at high redshift, which reveals an evolution in the population.

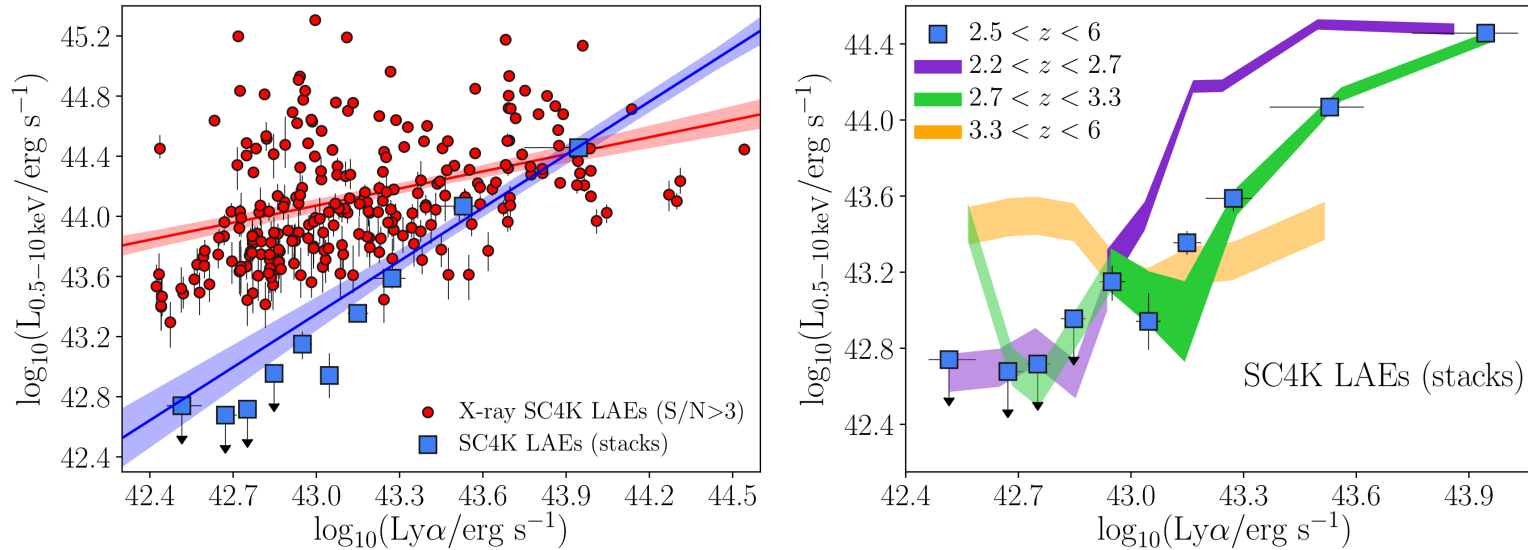


Figure 3.8: The X-ray luminosity plotted against the Ly α luminosity. *Left:* The red circles are the LAEs with X-ray $S/N > 3$. The blue squares encompass the sources of the full SC4K sample (stacks of Ly α luminosity bins) and the blue line represents the linear fit to the X-ray stacks as a function of Ly α luminosity, which results in a relation of the form $\log_{10}(L_X) = \log_{10}(\text{Ly}\alpha) \times (1.18 \pm 0.12) - (7.3 \pm 5.3)$. The red line is a linear fit to the direct detections. Both fits were done with *Scipy.optimize*. We find a significant correlation, suggesting that the Ly α and X-ray are tracing the same physical processes. The errors in the direct detections were estimated by taking the 68% confidence interval, following Section 3.3.1. For the stacked points the X-ray luminosity errors are also the 68% confidence, but the Ly α luminosity errors illustrate the bins used in the stack. *Right:* The X-ray luminosity vs the Ly α luminosity for LAEs at $2.2 < z < 2.7$, $2.7 < z < 3.3$ and $3.3 < z < 6$. The results show that LAEs at low redshift seem to have higher X-ray luminosity at a fixed Ly α luminosity above $10^{43} \text{ erg s}^{-1}$. We mark the luminosities for which we have only X-ray lower limits by increasing the transparency of the shadows (see also Table A.5 and the full tables available online). All Ly α bins at $3.3 < z < 6$ also provided lower limits for the X-ray luminosity.

Results based on the general X-ray selected population at high redshift find a negative evolution of the X-ray luminosity function (XLF) where the low-luminosity end progressively lowers and flattens with redshift (e.g. Georgakakis et al., 2015; Silverman et al., 2008). Given that X-ray LAEs seem to roughly reflect or follow the general X-ray selected population, it is possible that the behaviour of the XLF explains the lower number of detections at $z > 3.5$. We also point out that *Chandra*'s sensitivity is such that only the brighter X-ray AGN are detected even at the lower redshifts, so it is possible we are still missing X-ray LAEs even at lower redshift (see also Section 5.4 for further discussion).

In an effort to probe the X-ray activity of the sources which remain individually undetected in the X-rays in our analysis, we stack them. Figure 3.7 shows the results of X-ray stacking our sample of LAEs in bins of redshift (blue square markers) after removing individual AGN detections (X-ray $S/N > 3$). We find no X-ray detection in any of the redshift binned stacks, even if we re-define the bins to encompass larger redshift intervals (see Table 3.1) or when stacking the entire sample. The X-ray upper limits we find indicate that most LAEs have no significant X-ray emission and thus LAEs are mainly SF galaxies with a small subsample of X-ray bright, AGN-powered LAEs. We note that our stacking is capable of reaching faint luminosities in the X-rays, close to $\sim 10^{42} \text{ erg s}^{-1}$ at $z = 2$, the limit commonly used to separate AGN from star-forming galaxies, and corresponding to a SFR of $\sim 1000 M_{\odot} \text{ yr}^{-1}$. We note that very low luminosity AGN can still escape detection even in our stacking analysis. We also note that rejecting only the sources from Civano et al. (2016) (or those in our $S/N > 5$ analysis) results in tentative stack detections, particularly for the stacks at $z = 2.9$ and $z = 3.7$ which reach a $S/N \sim 2.2$. This is due to the stricter cut applied on the *Chandra* catalogue, causing some of the lower luminosity LAEs that are weakly detected in the X-rays at $S/N = 3 - 5$ to contribute to the stacks.

Table 3.1: The properties of the stacked LAEs in the SC4K sample as determined in this study. We divide the sample in bins of redshift and extract properties for each stack. We stack both using the full sample and excluding the X-ray and radio-detected LAEs. We also show the number of sources detected in the FIR (Jin et al., 2018) and radio. We include the median Ly α luminosity of the stacks, as well as the X-ray and radio mean luminosities, the SFR as determined from the Ly α and radio luminosities and the BHAR as determined from the X-rays. In addition, we show the BHAR/SFR ratio where the average ratio's errors are $^{+0.005}_{-0.003}$ (determined by taking the 68% confidence interval and applying standard error propagation where necessary), showing the evolution of the relative black hole-to-galaxy growth. The SFRs considered for the BHAR/SFR ratio are the average between the radio and Ly α SFRs. When a stack leads to a S/N < 3 we provide the 3σ limit as the upper-limit for the quantities. We also include the (X-ray + radio) AGN fraction, estimated using the number of sources on each bin (errors are binomial counting errors).

Subsample Stacked (Full sample)	$\log_{10} L$ Ly α [erg s $^{-1}$]	SFR (Ly α) [M $_{\odot}$ yr $^{-1}$]	$\log_{10} L$ X-rays [erg s $^{-1}$]	$\log_{10} L$ radio [W Hz $^{-1}$]	SFR (radio) [M $_{\odot}$ yr $^{-1}$]	\dot{M}_{BH} (X-rays) [M $_{\odot}$ yr $^{-1}$]	\dot{M}_{BH} — SFR	Total AGN fraction (%)	Radio detected (#)	FIR detected (#)
2.2 < z < 2.7	42.6 $^{+0.2}_{-0.2}$	4.2 $^{+4.0}_{-2.0}$	43.12 $^{+0.05}_{-0.05}$	23.81 $^{+0.01}_{-0.01}$	-	0.047 $^{+0.005}_{-0.005}$	0.007	9.1 \pm 0.9	32	13
2.7 < z < 3.5	42.9 $^{+0.2}_{-0.1}$	6.1 $^{+5.5}_{-2.6}$	43.12 $^{+0.07}_{-0.07}$	23.22 $^{+0.04}_{-0.03}$	-	0.047 $^{+0.008}_{-0.007}$	0.005	9.7 \pm 0.6	69	26
3.5 < z < 5.8	43.1 $^{+0.2}_{-0.3}$	9.8 $^{+9.9}_{-5.2}$	<43.2	<23.2	-	<0.059	<0.006	4.9 \pm 0.7	15	7
2.2 < z < 5.8	42.9 $^{+0.3}_{-0.2}$	6.0 $^{+7.0}_{-2.7}$	43.06 $^{+0.06}_{-0.07}$	23.53 \pm 0.01	-	0.041 $^{+0.006}_{-0.006}$	0.005	8.6 \pm 0.4	116	46
(no AGN)										
2.2 < z < 2.7	42.6 $^{+0.2}_{-0.1}$	4.1 $^{+3.7}_{-1.9}$	<42.6	22.45 $^{+0.12}_{-0.14}$	9.0 $^{+3.0}_{-2.5}$	<0.013	<0.0019	-	-	3
2.7 < z < 3.5	42.9 $^{+0.2}_{-0.1}$	6.0 $^{+5.3}_{-2.5}$	<42.8	22.52 $^{+0.14}_{-0.14}$	10.6 $^{+4.1}_{-3.2}$	<0.021	<0.0025	-	-	7
3.5 < z < 5.8	43.1 $^{+0.2}_{-0.3}$	9.8 $^{+9.7}_{-5.2}$	<43.2	<23.1	<43.5	<0.060	<0.0061	-	-	1
2.2 < z < 5.8	42.8 $^{+0.3}_{-0.2}$	5.9 $^{+6.8}_{-2.7}$	<42.7	22.47 $^{+0.12}_{-0.13}$	9.3 $^{+3.0}_{-2.4}$	<0.017	<0.0022	-	-	11

3.4.3 X-ray luminosity vs Ly α luminosity

To test for a relation between the X-ray and Ly α luminosities, we divided the sample in bins of Ly α luminosity and performed stacking in the X-ray full band (0.5-10 keV). Stacking in the X-rays based on bins of Ly α luminosity by including the X-ray LAEs (see Figure 3.8, left panel) yields detections for all stacks except for the faintest Ly α luminosities ($< 10^{42.9}$ erg s $^{-1}$). There is a clear positive correlation between the X-ray and Ly α luminosities. Furthermore, the relation is present when considering the individually detected LAEs (red markers and red linear fit, Figure 3.8, left panel). From these results, it is clear that the driving force behind the X-ray-Ly α relation is the AGN activity. In other words, the Ly α emission of the X-ray direct detections is likely coming from the BH activity, and thus tracing the black hole accretion rate, while for the remainder of the sample Ly α likely comes from SF processes. This dichotomy of the origins of Ly α emission has also been identified in a recent study by Dittenber et al. (2020) on a sample of spatially resolved LAES at $z < 0.1$. Dittenber et al. (2020) find that, in 9 of the 12 galaxies considered, compact objects may be a major source of Ly α emission, with SFR processes like the activity of high mass x-ray binaries and AGN nuclear activity having possible roles in the powering of Ly α emission. This suggests that the duality of Ly α emission's origins is observed across redshift and might have consequences for the study of the epoch of reionisation.

We also investigate whether the X-ray-Ly α relation is evolving with redshift. The results are shown in Figure 3.8, where the right panel reveals an evolution of the luminosity relation for each of the three redshift bins shown in Table 3.1 ($z = 2.2 - 2.7$, $z = 2.7 - 3.5$ and $z = 3.5 - 5.8$). Our results suggest differences in the relation that are dependent on the redshift intervals being considered. The X-ray LAEs at $2.2 < z < 2.7$ reveal higher X-ray luminosities for the same Ly α luminosity (for $L_{\text{Ly}\alpha} > 10^{43}$ erg s $^{-1}$) when compared to the sources at $2.7 < z < 6$. Such result could point to an evolution in the accretion efficiency, in the typical Eddington ratios (affecting X-ray emission) and/or an evolution on the production and escape of Ly α photons for a given X-ray luminosity or BHAR.

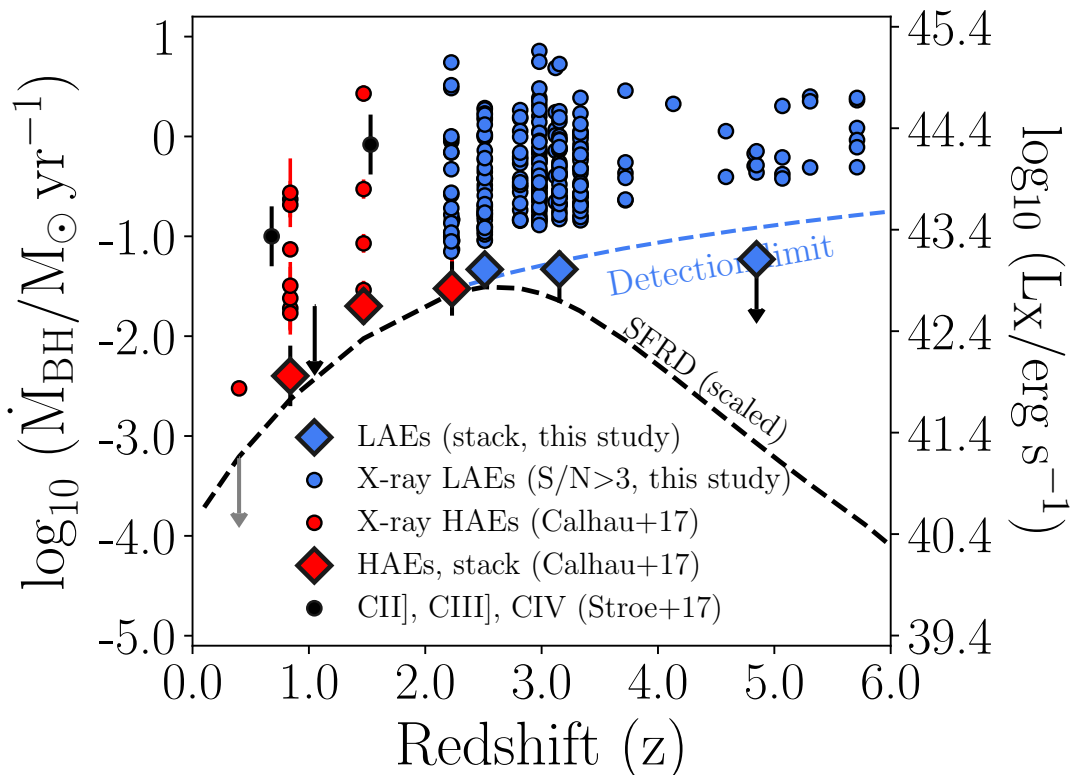


Figure 3.9: The BHARs of LAEs across redshift. We find relatively constant BHARs for LAEs across time. The large markers represent the stacking and the smaller markers are LAEs that have been directly detected by *Chandra*. The dashed blue line is the detection limit of our study when demanding a 3σ cut. The dashed black line shows the evolution of the SFRD derived by Khostovan et al. (2015), scaled to coincide with the BHAR at $z \sim 2.5$. Note that while the BHARs seem to follow the evolution of the SFRD up to $z \sim 2.5$, this is not clear at $z > 3$, although our results suggest that there is no significant rise. We also place our results into context by comparing them with the BHARs of $\text{H}\alpha$ -selected sources from Calhau et al. (2017) and to the CII], CIII] and CIV emitters from Stroe et al. (2017). The errorbars were estimated using the 68% confidence interval for our data and by taking the values from the literature otherwise.

3.4.4 \dot{M}_{BH} of LAEs vs \dot{M}_{BH} of HAEs

As can be seen in Figure 3.9, X-ray LAEs have moderate to strong BHARs, with a median of $0.42_{-0.2}^{+0.7} M_{\odot} \text{yr}^{-1}$ and an average BHAR of $0.72_{-0.01}^{+0.02} M_{\odot} \text{yr}^{-1}$. We also show the average stacks of our sample in three redshift bins (see also Table 3.1). Our stacking reveals relatively low BHARs of $\text{BHAR} = 0.047_{-0.005}^{+0.005} M_{\odot} \text{yr}^{-1}$ and $0.047_{-0.007}^{+0.008} M_{\odot} \text{yr}^{-1}$, for $2.2 < z < 2.7$ and $2.7 < z < 3.5$, respectively. We find no significant detection for the $3.5 < z < 6$ X-ray stack (see Figure 3.9).

Also shown in Figure 3.9 are the emission line-selected sources from Stroe et al. (2017) and Calhau et al. (2017). A comparison between results reveals that BHARs of X-ray LAEs are similar to the BHARs of $z = 0.68$ and $z = 1.53$ CII] and CIV emitters (obtained by Stroe et al. 2017). They are also comparable to the more powerful X-ray counterparts of HiZELS at $0.8 \leq z \leq 2.23$. Comparing the stacks reveals BHARs comparable to the BHAR for the stacks of the HAEs at redshift 1.5 – 2.2.

Figure 3.9 also shows the evolution of the SFRD presented by Khostovan et al. 2015 and scaled so that the SFRD at $z \sim 2.5$ coincides with the BHAR at the same redshift. Our results can be considered consistent with the BHAR following the evolution of SFRD up to $z \sim 3.0$, something that is mirrored by HAEs at lower redshift. Even though the current detection limits do not allow us to confirm whether such trend remains for redshifts greater than $z = 3.5$, the relatively strong upper limits at high redshift are consistent with a drop of the BHARs.

3.5 Conclusions

We have studied the X-ray properties of 3700 LAEs ($\text{Ly}\alpha$ Emitters) at $2 < z < 6$ from the SC4K sample (Sobral et al., 2018a), and investigated the possible relations between those quantities and $\text{Ly}\alpha$. We made use of the publicly available data from COSMOS to stack the sample and get the average X-ray luminosity and BHAR of LAEs. Our main results are:

- A total of 254 LAEs ($6.8\% \pm 0.4\%$) are detected by *Chandra* and so classified as X-ray AGN.

- Most X-ray detections (227/254) are found at $z = 2.2\text{--}3.5$ with luminosities ranging from $L_X = 10^{43} \text{ erg s}^{-1}$ to $L_X = 10^{45} \text{ erg s}^{-1}$, resulting in BHARs as high as $\sim 7 M_\odot \text{ yr}^{-1}$.
- X-ray LAEs have a hardness ratio of -0.1 ± 0.2 , consistent with the global X-ray AGNs at similar redshifts. We find that about half of the X-ray LAEs have hardness ratios consistent with obscured sources, with this fraction declining with increasing X-ray luminosity, but showing no change with $\text{Ly}\alpha$ luminosity or redshift.
- The X-ray luminosity of our LAEs correlates with the $\text{Ly}\alpha$ luminosity as $\log_{10}(L_X/\text{erg s}^{-1}) = \log_{10}(L_{\text{Ly}\alpha}/\text{erg s}^{-1}) \times (1.18 \pm 0.12) + (7.3 \pm 5.3)$, driven by the AGN present within the sample. $\text{Ly}\alpha$ is likely tracing the BHAR for X-ray LAEs.
- LAEs remain undetected in deep X-ray stacks performed by excluding X-ray LAEs ($S/N > 3$). As a result, non X-ray LAEs present a low average BHAR of $< 0.017 M_\odot \text{ yr}^{-1}$.
- The low BHAR of LAES is in accordance with the BHAR of lower redshift line-emitting star-forming galaxies with detectable X-ray emission. Comparison reveals that LAES have BHARs similar to those of CII] and CIV] emitters at $z = 0.68$ and $z = 1.53$. LAEs BHARs are also comparable to the more powerful counterparts of HiZELS HAEs at $0.8 < z < 2.23$.

Our results reveal that LAEs at high redshift are mostly star-forming galaxies with relatively low AGN activity ($\text{BHAR} < 0.017 M_\odot \text{ yr}^{-1}$), but with a few ($6.8\% \pm 0.4\%$) X-ray-bright AGN where the $\text{Ly}\alpha$ emission likely comes from the accretion of matter into the central super-massive black hole. These X-ray LAEs become the dominant population among LAEs at the highest $\text{Ly}\alpha$ luminosities, but there seems to be an important negative evolution of such population towards high redshift. Future studies are required to conduct deep spectroscopic observations of LAEs to unveil even lower BHARs, to establish the redshift evolution even more conclusively, and to identify the physical origins and their consequences for how early galaxies form and evolve.

Chapter 4

The radio activity of typical and
luminous Ly α emitters from $z\sim 2$
to $z\sim 6$

Abstract

We study the radio properties of ~ 4000 LAEs at $2.2 < z < 6$ from the SC4K survey in the COSMOS field. We make use of VLA data, and detect 120 ($3.2\% \pm 0.3\%$) of the LAEs individually in the Radio (in either 1.4 GHz or 3.0 GHz, $S/N > 3$). We find an average 1.4 GHz luminosity of $10^{24.71 \pm 0.03} \text{ W Hz}^{-1}$, consistent with moderate to low luminosity radio AGN. Approximately half of the LAEs detected in the radio are also detected in the X-rays. We find that radio LAEs have an average spectral index of $-1.3_{-1.5}^{+0.4}$, steeper than the mean value for the spectral index in the COSMOS field, but consistent with AGN sources and more extreme star-forming galaxies. We find no relations between the spectral index and the $\text{Ly}\alpha$ luminosity or between radio luminosity and $\text{Ly}\alpha$ luminosity, suggesting little to no relation between them for the population of SC4K. While stacking and excluding radio LAEs, we find detections ($S/N \sim 3-4$) when stacking the full sample and at lower redshifts, with luminosities in the SF dominated region of radio luminosities ($L_{\text{radio}} \sim 10^{22.4-22.5} \text{ W Hz}^{-1}$). Splitting the sample in further redshift slices results in no detections. Our results suggest that the majority of the LAE population is made of star-forming galaxies, detectable only in the the deepest radio stacks.

Calhau, J., Sobral, Santos, S., Matthee, J., Paulino-Afonso, A., Stroe, A., Simmons, B., Barlow-Hall, C., Adams, B., 2020, MNRAS, 493, 3

4.1 Introduction

Radio emission is often associated with both AGN (from radio jets and lobes) and star forming processes (such as supernovae remnants) and it is often difficult to separate between the two origins for radio emission (see, e.g. Meurs & Wilson, 1984; Sadler et al., 2002).

AGN were one of the first sources to be identified through radio observations (Bolton et al., 1949) and stood out due to their high luminosities. This makes them good tracers of the early Universe, as they are easily detected even at higher redshifts, and are used to study both the evolution of the more massive galaxies and high dense environments (e.g. Miley & De Breuck, 2008; Venemans et al., 2007). The energy released by the relativistic jets and lobes of radio AGN comprise an important form of AGN feedback, as the energy released in the emission prevents the gas in the galaxy from cooling down enough to start forming stars (e.g. McNamara & Nulsen, 2007). Not only that, but the relativistic jets are also responsible for the generation of massive gas outflows, which influence the formation of stars in the central regions of the galaxies (e.g. Holt et al., 2008; Morganti et al., 2005).

On the star formation side of galaxy evolution, radio observations have been involved in the understanding of the evolution of the SFRD across cosmic time. These studies can be made from a variety of different wavelengths (mostly FIR and UV), but the results can differ significantly in magnitude (Hopkins & Beacom, 2006; Hopkins et al., 2003; Kennicutt, 1998), partly due to the uncertainties from dust absorption. Radio observations do not suffer from the effects of dust and has been used as a tool to try and obtain a dust-free estimation of SFR across redshifts (e.g. Smolčić et al., 2009), but suffer from two major complications: 1) the need for deep observations, in order to reach the regime where star formation starts to dominate (e.g. Sadler et al., 2002; Seymour et al., 2008) and; 2) the fact that the use of radio as a SFR indicator is subject to uncertainty due to being derived from the poorly understood relation between radio and infrared. This relation is thought to be constant and linear (see, e.g. Yun et al., 2001), but recent studies point to the possibility of an evolution with redshift (Calistro Rivera et al., 2017; Delhaize et al., 2017). However, these results are either unable

to dismiss the existence of a flat relation or need a more detailed understanding of the radio emission and required corrections in order to understand the radio-IR correlation, particularly the effect of possible AGN contamination.

$\text{Ly}\alpha$ emission is also often associated with periods of strong star formation (e.g., Cowie & Hu, 1998; Pirzkal et al., 2007) and AGN activity (e.g., Sobral et al., 2018b; Wold et al., 2017). In the previous Chapter we showed that $\text{Ly}\alpha$ may also correlate with the BHAR of an AGN from the correlation observed between $\text{Ly}\alpha$ luminosity and X-ray luminosity.

However, $\text{Ly}\alpha$ is also known to be found in radio sources, such as quasars (e.g. Christensen et al., 2006; Weidinger et al., 2004). Furthermore, the presence of the so called $\text{Ly}\alpha$ blobs (LABs) are generally attributed to the effect of relativistic jets or supernovae outflows (e.g., Hu et al., 1991; Wilman et al., 2000). At the same time, however, studies have also shown that $\text{Ly}\alpha$ structures, particularly low brightness $\text{Ly}\alpha$ haloes, do not appear to have any correlation with radio activity or structures such as radio lobes and jets (Villar-Martín et al., 2002).

In this Chapter, we probe the radio activity of LAEs at $z \sim 2 - 6$ and characterise their radio properties, from their radio spectral index and AGN activity to the possible existence of an association between radio emission and $\text{Ly}\alpha$ luminosity.

4.2 Radio data: 1.4 GHz and 3 GHz VLA-COSMOS

The VLA-COSMOS Survey (Bondi et al., 2008; Schinnerer et al., 2004, 2007, 2010) used the National Radio Astronomy Observatory’s Very Large Array to conduct deep, wide-field imaging with $\approx 1.5''$ resolution at 1.4 GHz continuum of the 2 deg² COSMOS field (Figure 3.1). The data reaches down to a 1σ sensitivity of about $11 \mu\text{Jy beam}^{-1}$, leading to Bondi et al. (2008) presenting a catalog of roughly 3600 radio sources.

The VLA’s 3 GHz COSMOS Large Project covers the entirety of the COSMOS field at a deeper average sensitivity of $2.3 \mu\text{Jy beam}^{-1}$ and also at a higher spatial resolution, with an average beam-width of $0.75''$. The observations and data reduction details can be found in Smolčić et al. (2017), including a catalogue of

over 10,000 radio sources. Usage of the 3 GHz VLA data allows us to further probe the existence of radio-emitting AGN over a larger area, as this survey covers the entirety of SC4K. In addition, by removing radio-detected AGN and obtaining deep radio stacks, radio data will allow us a dust-independent determination of the SFRs of SC4K LAEs (as confirmed in Section 5.2.1). We nevertheless caution that removing the radio-detected sources may still result in some contamination from undetected low luminosity radio AGN.

4.3 Methodology

4.3.1 Radio analysis

4.3.1.1 Source detection: 3 GHz

For our analysis, we use the VLA-COSMOS 3 GHz Large Project data in Jy/beam. Smolčić et al. (2017) estimate the fluxes of the sources by selecting all pixels above a S/N threshold (≥ 5) and enforcing a minimum area of 3 px by 3 px. The total flux density is taken as the sum of all the values within the area and then dividing it by the beam size in pixels. The peak flux is estimated by fitting a two-dimensional parabola around the brightest pixel. We use a simpler method and fix an aperture with a radius of $0.6''$ ($0.8 \times$ beam radius) for a total integration area of $1.76''^2$. We also apply an aperture correction to recover the Smolčić et al. (2017) fluxes on average (see Section 4.3.1.4 and Figure 4.1).

4.3.1.2 Source detection: 1.4 GHz

For the 1.4 GHz VLA-COSMOS data, Schinnerer et al. (2007) use AIPS (Astronomical Image Processing System, Greisen, 2003) to find sources with peak fluxes higher than a certain flux level ($30 \mu\text{Jy beam}^{-1}$, $\sim 3\sigma$ in the most sensitive regions). For each component, AIPS gives the peak flux and total flux, among other quantities, by either Gaussian fitting or applying non-parametric interpolation. The original catalogue has since been updated by Bondi et al. (2008), which we use in this work. Because the resolution of the 1.4 GHz band is poorer

than 3.0 GHz, we use a larger fixed aperture of $2.5''$ radius ($1.4 \times$ beam radius) for our analysis, for a total integration area of $19.6''^2$, selected in order to make our fluxes as similar to Bondi et al. (2008) as possible.

4.3.1.3 Background estimation

To determine the background we place $1.2''$ apertures ($0.6''$ radius) for the 3 GHz band and $5''$ apertures ($2.5''$ radius) for the 1.4 GHz band, masking the image borders and the area centred on the LAE for which we are performing the flux measurement. The placement of the empty apertures is restricted to a region of 100×100 px around each LAE, allowing us to measure the local background and noise levels. The fluxes in the background areas are summed and the total background is taken as the median of ~ 2000 random apertures. We then subtract this value from the source's flux.

The uncertainty is taken as the 84th and 16th percentile of the background (upper and lower errors, respectively). We define the S/N as the ratio between the source's flux and the lower error of each image. A source is considered detected if the S/N rises above or equals 3, but we also define S/N cuts of 5 and use the Smolčić et al. (2017) catalogue.

4.3.1.4 Radio flux and spectral index estimation

We compare our aperture fluxes F_{ν_0} with the appropriate full fluxes F_r obtained by either Smolčić et al. (2017) for 3 GHz or Bondi et al. (2008) for 1.4 GHz and calculate an aperture correction (A_C) per band as the median of the flux difference in log space¹. We define our full radio fluxes (F_ν), aperture corrected to median match Smolčić et al. (2017) or Bondi et al. (2008) catalogue fluxes, as:

$$\log_{10}(F_\nu) = \log_{10}(F_{\nu_0}) + A_C \quad (4.1)$$

We find $A_C = -0.05$ and $A_C = 0$ for the 3.0 GHz and 1.4 GHz bands, respectively, which we apply throughout this paper. In order to assure we obtain full radio

¹ $A_C = \text{median}[\log_{10}(F_r) - \log_{10}(F_{\nu_0})]$.

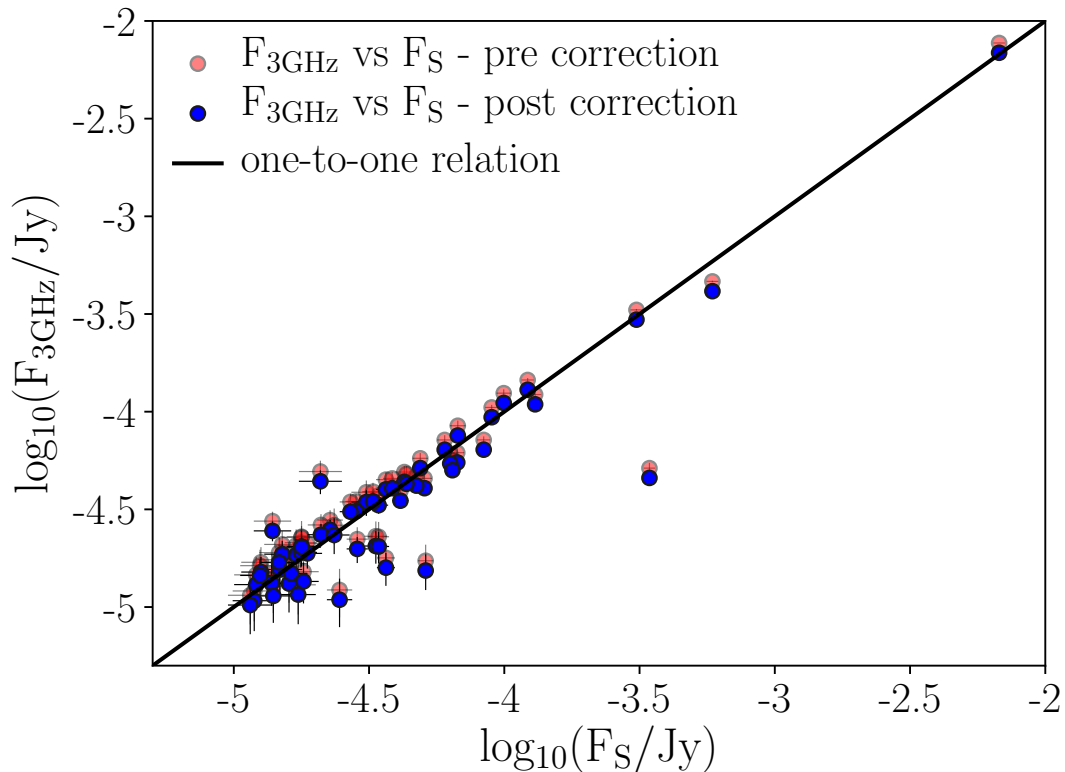


Figure 4.1: Comparison between our initial radio fluxes ($F_{3\text{GHz}}$) and those of Smolčić et al. (2017) (F_S). The black line represents a perfect agreement between measurements. The blue points show the flux difference between the two data sets after applying the correction.

fluxes in individual detections and for stacks we derive and apply a flux correction based on fluxes published by Bondi et al. (2008); Schinnerer et al. (2007); Smolčić et al. (2017). Figure 3.2 shows the comparison between our initial radio fluxes and the corrected ones when compared to Smolčić et al. (2017).

By using the radio fluxes, we also calculate the radio spectral index α , estimated between 1.4 GHz and 3.0 GHz, as:

$$\alpha = \frac{\log_{10}\left(\frac{F_{3\text{GHz}}}{F_{1.4\text{GHz}}}\right)}{\log_{10}\left(\frac{3}{1.4}\right)} \quad (4.2)$$

where F_ν is the flux at frequency ν .

4.3.1.5 Radio luminosity estimation

We estimate the radio luminosities by using:

$$L_\nu = \frac{4\pi d_L^2}{(1+z)^{\alpha+1}} F_\nu \text{ (W Hz}^{-1}\text{)}, \quad (4.3)$$

where d_L is the luminosity distance in meters, z is the redshift, F_ν is the flux at 1.4 GHz or 3 GHz ($\text{W Hz}^{-1} \text{ m}^{-2}$) and α is the radio spectral index. We assume $\alpha = -0.8$, the characteristic spectral index of synchrotron radiation and a value typically found in AGN (Delhaize et al., 2017, although for a wider redshift range of $0 < z < 5$), even though we note that, on average, our sources detected in both 1.4 GHz and 3 GHz show a steeper α (≈ -1.3). Because the 3 GHz data is deeper than the 1.4 GHz, it is possible the steeper indices are a selection effect of the increased depth of the 3 GHz band. Furthermore, a very steep spectral index may lead to source being more easily detectable in 1.4 GHz (see Figure 1.1). However, the unique advantage of the current deeper 3 GHz data is the much higher spatial resolution, diminishing the risk of contamination by nearby sources. Therefore, throughout this paper, we chose to make use of the 3 GHz data whenever possible. We then convert the 3 GHz fluxes into 1.4 GHz luminosity by following the steps detailed in Delhaize et al. (2017):

$$L_{1.4\text{ GHz}} = \frac{4\pi d_L^2}{(1+z)^{\alpha+1}} \left(\frac{1.4\text{ GHz}}{3.0\text{ GHz}} \right)^\alpha F_{3\text{ GHz}} \text{ (W Hz}^{-1}\text{)} \quad (4.4)$$

where $F_{3\text{ GHz}}$ is the flux in the 3 GHz band ($\text{W Hz}^{-1} \text{ m}^{-2}$), D_L is the luminosity distance in m and α is the spectral index, assumed to be -0.8 . When referring to luminosities in the radio band, we use the converted 3.0 GHz \rightarrow 1.4 GHz luminosity (hereafter L_{radio}) and only use the 1.4 GHz measurements for the sources that are not detected in the 3 GHz band (which we specifically refer to as $L_{1.4\text{ GHz}}$).

4.3.1.6 Radio stacking

We perform mean and median stacking in each individual band, both when including all sources and after removing the radio detections. As with the X-ray

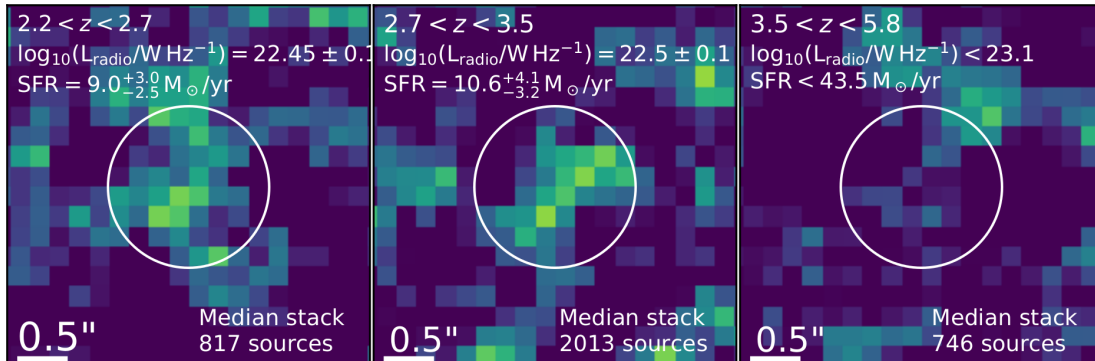


Figure 4.2: The results of median stacking the SC4K LAEs not directly detected in the radio. We detect weak radio emission from LAEs for the stacks at $z = 2.2 - 2.7$ (*left*) and $z = 2.7 - 3.5$ (*middle*) with radio luminosities of $L_{\text{radio}} = 10^{22.5 \pm 0.1} \text{ W Hz}^{-1}$, corresponding to $\text{SFR} = 9.0^{+3.0}_{-2.5} \text{ M}_{\odot} \text{ yr}^{-1}$ and $L_{\text{radio}} = 10^{22.5 \pm 0.1} \text{ W Hz}^{-1}$, corresponding to $\text{SFR} = 10.6^{+4.1}_{-3.2} \text{ M}_{\odot} \text{ yr}^{-1}$, respectively. For $z > 3.5$ we are able to provide a 3σ upper limit of $\text{SFR} < 44 \text{ M}_{\odot} \text{ yr}^{-1}$. Errors are the 68% confidence interval.

data, we perform stacking for various sub-samples (see table A.4), taking the median redshift of each stack in order to calculate the luminosity distances required for estimating radio luminosities.

4.4 The radio properties of LAEs at $2 < z < 6$

Using the method detailed in Section 4.3.1, we find a total of 116 LAEs ($\text{S/N} > 3$) in either the 1.4 GHz or 3 GHz radio bands. Out of the total 116 radio sources, most (88) are detected in the 3 GHz data, with 28 being detected exclusively in the 1.4 GHz VLA data and 25 in both. Out of all radio sources, 56 are also detected in the X-rays by *Chandra*.

We obtain a very significant detection ($\text{S/N} \sim 50$) when stacking the entire sample of LAEs in the radio, revealing a radio luminosity of $L_{\text{radio}} = 10^{23.53 \pm 0.01} \text{ W Hz}^{-1}$, where the errors are the 68% confidence region. We also find detections in the radio stacks of LAEs when we split the sample in redshift, with stacks of LAEs at $z = 2.2 - 2.7$ and $z = 2.7 - 3.5$ yielding particularly high S/N radio detections. Stacks of LAEs obtained as a function of $\text{Ly}\alpha$ luminosity also reveal clear detections, but these include the direct radio detections, almost certainly powered by

AGN activity, which we find dominate the stacks.

Removing the LAEs directly detected in the radio from the sample leads to a much lower radio signal, and to a weak ($S/N = 3.9$) radio detection for the entire sample, with $L_{\text{radio}} = 10^{22.47 \pm 0.1} \text{ W Hz}^{-1}$. We also detect weak radio emission when removing radio detections for $2.2 < z < 2.7$ and $2.7 < z < 3.5$ (see Figure 4.2), but not at the highest redshifts (see Table 3.1).

4.4.1 Radio spectral index and $\text{Ly}\alpha$ luminosity

We follow Section 4.3.1.4 and estimate the radio spectral index for the LAEs detected in both the 1.4 and 3.0 GHz bands. We find that the average spectral index is $-1.3^{+0.4}_{-1.5}$. We find some unusually steep spectral indices, especially for the sources for which we can only provide limits (see Figure 4.3), but many of these values are affected by large errors. We note, nonetheless, that Smolčić et al. (2017) constrain their spectral indices to a minimum of -2.5 , when estimating α . This is because standard synchrotron radiation does not result in spectral indices lower than -2.5 , unless it is an exotic source (such as free-free absorption processes found in rare quasars, see Krishna et al., 2014; Rees, 1967). We do not apply any constraints to our spectral indices but it should be noted that values lower than -2.5 are unlikely to be physically meaningful and that applying a cut of $S/N > 5$ to our data results in these low spectral indices disappearing for all but two sources.

As Figure 4.3 shows, we do not find a statistically significant relation between the radio spectral index and $\text{Ly}\alpha$ luminosity, suggesting little to no relation between them for the range of $\text{Ly}\alpha$ luminosities probed by SC4K. However, we find that the radio spectral indices of the radio LAEs are steeper than the mean spectral index for the overall COSMOS survey ($\bar{\alpha} = -0.73$, see Smolčić et al., 2017). Our results imply that radio LAEs are not representative of the overall radio-selected population. The steeper (more negative) average α for radio LAEs is still consistent with a sub-sample of AGN sources and potentially some more extreme star-forming galaxies in literature (e.g. Delhaize et al., 2017).

Spectral indices can be used in several different ways, such as a probe for the origins of the radio emission itself (e.g. thermal emission, synchrotron radiation;

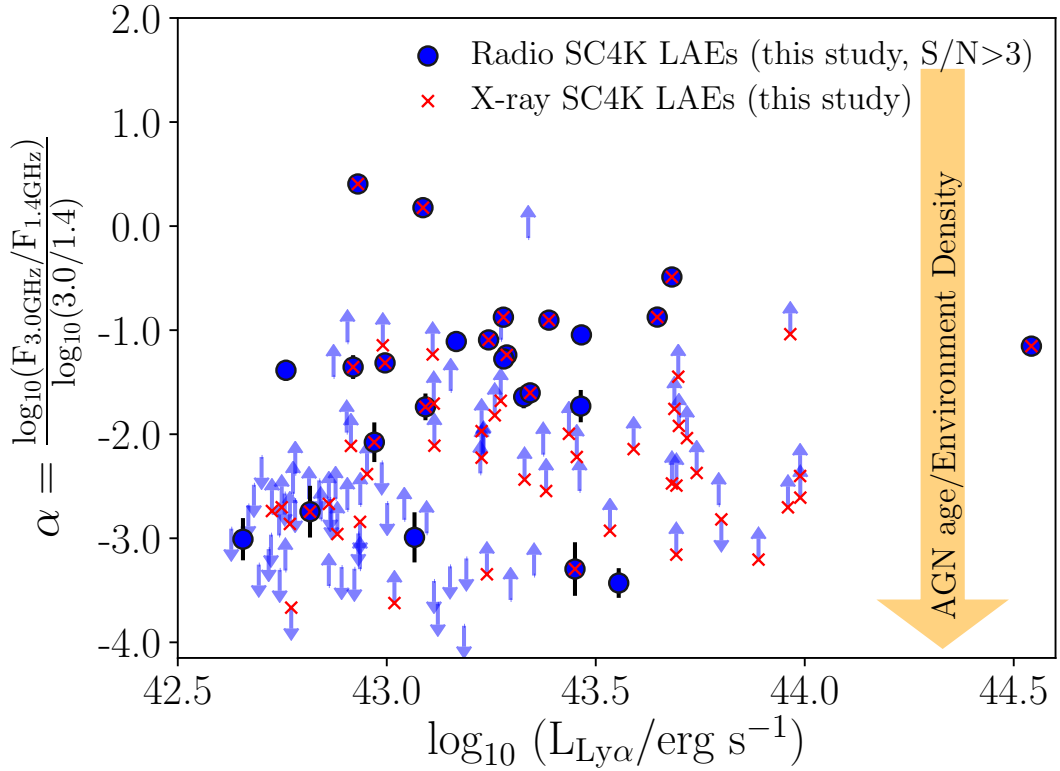


Figure 4.3: The radio spectral index, estimated between 1.4 GHz and 3.0 GHz, against the Ly α luminosity for LAEs. Our results show that there is no significant relation between the radio spectral index and Ly α luminosity, consistent with radio properties being uncorrelated with Ly α properties for LAEs. Errors were estimated by taking the 68% confidence interval on the fluxes and applying standard error propagation.

Klein & Emerson, 1981). Thermal emission from HII regions would result in a spectral index of $\alpha = -0.1$ to $\alpha = 2.0$, with steeper indices being a characteristic of synchrotron radiation. Our results are therefore consistent with radio emission from synchrotron processes, such as those found in radio AGN. Spectral indices can also be used as a measure of the age or density of the environment surrounding the source. This is because radio galaxies with steeper spectral index are generally located at the centre of rich clusters of galaxies (see e.g. Athreya & Kapahi, 1998; Klammer et al., 2006). As radio LAEs have steeper α than the general radio-selected population, our results may suggest that they are good tracers of high density regions at high redshift (i.e. protoclusters; Franck & McGaugh, 2016). This is consistent with several results in the literature. For example, Venemans et al. (2007) and Yamada et al. (2012) found bright LAEs around dense regions of the Universe for $2 < z < 5.2$ (see also Kubo et al., 2013; Overzier, 2016). Furthermore, more recently, Khostovan et al. (2019) conducted a detailed clustering analysis of faint to luminous LAEs, including the SC4K LAEs, to find that luminous LAEs reside in the most massive dark matter haloes at high redshift, and are therefore consistent with being progenitors of some of the most massive clusters found today (see also Matsuda et al., 2004).

4.4.2 Radio luminosity of LAEs as a function of redshift

The LAEs detected directly in the radio present an average $L_{\text{radio}} = 10^{24.94 \pm 0.02} \text{ W Hz}^{-1}$ across the full redshift range, as can be seen in Figure 4.4. Such high radio luminosities are well into the AGN dominated region of the radio luminosity range ($L_{\text{radio}} > 10^{23.2} \text{ W Hz}^{-1}$; e.g. Meurs & Wilson, 1984; Sadler et al., 2002, see Figure 4.4). Even at $z \sim 2$ the radio data is not deep enough to individually detect sources which would be in the clear SF regime. At higher redshifts the higher luminosity limit leads to a stronger bias towards detecting the highest radio luminosity LAEs only (see Figure 4.4). This high luminosity limit at high redshift, combined with a lower number of LAEs, might be able to explain the relatively low number of radio LAEs at higher redshift, although it is worth noting that we do not find a single radio LAE at a redshift beyond $z \sim 5$.

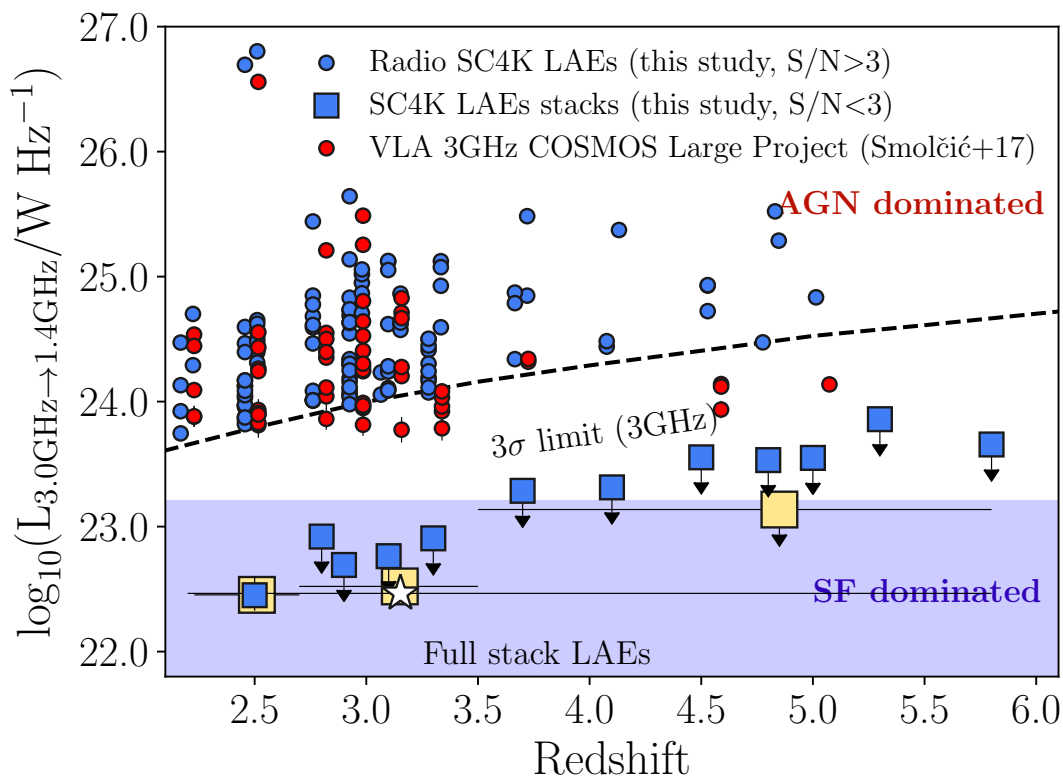


Figure 4.4: The radio luminosity of LAEs across redshift. The blue circles represent the direct detections found following the method presented in Section 4.3.1, while the red circles show our results using the VLA 3 GHz COSMOS catalogue (Smolčić et al., 2017), shifted by +0.05 in redshift. We also show the results of stacking in bins of redshift (square markers). We find detections for the stacks of $2.2 < z < 2.7$ and $2.7 < z < 3.5$. We also detect radio emission when stacking the full sample while excluding radio LAEs (white star). All three detected stacks are situated well in the radio luminosity range where star formation is expected to take over radio emission (e.g. Meurs & Wilson, 1984). Errors were estimated using the 68% confidence interval. For the stack points the horizontal errorbars illustrate the width of the bins used.

The radio detection limit biases detections towards radio AGN. However, by stacking, and particularly by stacking in the radio and excluding radio LAEs, we can investigate the typical radio luminosities of the remaining population. Our results are shown in Figure 4.4. For our stacking analysis we use the 3 GHz band, due to the higher resolution and depth of the survey. We find weak radio detections ($S/N \sim 3 - 4$) in the stacks when we use the full sample of non radio LAEs and at lower redshift, placing the majority of the sources well within the SF dominated region of radio luminosities, with $L_{\text{radio}} \approx 10^{22.4-22.5} \text{ W Hz}^{-1}$. Splitting the sample in further redshift slices leads to upper limits which are fully consistent with our weak detections, only achievable due to the combination of the radio data depth and the large number of LAEs in SC4K. Our results imply that some LAEs have high radio luminosities, allowing them to be directly detected in the radio, but that the majority of the LAE population is made of star-forming galaxies with very weak radio luminosities, only detectable with very deep radio stacks.

4.4.3 Radio luminosity vs Ly α luminosity

In Section 3.4.3 we found strong relations between X-ray and Ly α luminosities, implying a clear link between them and BHARs. Here we investigate if there is a similar relation between radio and Ly α luminosities. The results are presented in Figure 4.5. Our results show a flat relation between radio and Ly α luminosities for radio detected sources (see Figure 4.5). Stacking (including radio LAEs) shows a potential weak relation but this result is consistent with no relation within 2σ .

The absence of a relation between the radio and Ly α luminosities suggests radio emission and Ly α emission may be unrelated or out of sync, unlike X-ray and Ly α . It is possible that the radio is simply tracing different AGN-related processes than the ones Ly α and X-rays trace. Differences could arise if the origin of radio emission happens on different physical scales (e.g. jets or away from the X-ray emitting region), also implying different timescales between the accretion of matter and the emission, but also because radio emission can be much more long-lived. Significant variability in AGN LAEs could potentially explain why radio luminosities for LAEs are uncorrelated with the likely BHAR-driven Ly α emission.

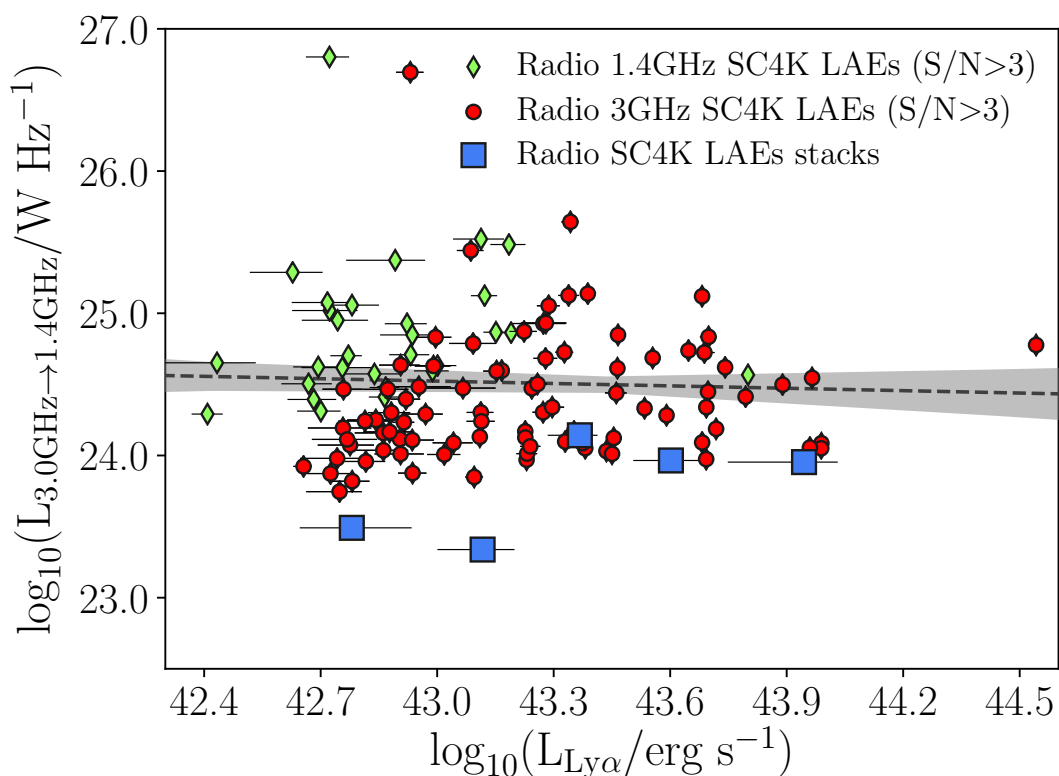


Figure 4.5: The radio luminosity of LAEs versus their Ly α luminosity. We find no statistically significant correlation between the two quantities, suggesting that radio and Ly α are tracing processes with different physical origins or timescales. The red markers are the LAEs detected directly in the 3.0 GHz band, while the green diamonds represent the sources that are only detected at 1.4 GHz. The blue squares represent stacking made in bins of Ly α luminosity using all LAEs. Errors were estimated from the 68% confidence interval. The black line represent a linear regression fit (using *Scipy.optimize*) to direct detections with 1σ uncertainties.

4.5 Conclusions

We have studied the radio properties of 3700 LAEs ($\text{Ly}\alpha$ Emitters) at $2 < z < 6$ from the SC4K sample (Sobral et al., 2018a), and investigated the possible relations between those quantities and $\text{Ly}\alpha$. We made use of the publicly available data from COSMOS to explore the radio properties of LAEs and use the available data from VLA-COSMOS to also stack the sample in the radio and estimate the SFR and radio properties of typical LAEs. Our main results are:

- Overall, $3.1\% \pm 0.3\%$ (116) of our LAEs are detected in the radio, either in the 1.4 GHz or 3 GHz (or both) bands.
- The radio-detected LAEs have an average $L_{\text{radio}} = 10^{24.94 \pm 0.03} \text{ W Hz}^{-1}$, has expected from AGN sources. We do not find radio LAEs at $z > 5$, although that may be due to the luminosity limit. Even at $z = 2$ we are not sensitive enough to individually detect sources in the SF regime.
- We obtain significant detections when stacking the entire sample in the radio ($S/N > 50$) for an average radio luminosity of $L_{\text{radio}} = 10^{23.53 \pm 0.01} \text{ W Hz}^{-1}$. We find further detections when splitting the sample in redshift, at $z = 2.2 - 2.7$ and $z = 2.7 - 3.5$.
- Removing the radio-detected LAEs from the sample yields detections in the same stacks as mentioned above, albeit with much lower signal ($S/N \sim 3.5$) and an average luminosity of $L_{\text{radio}} = 10^{22.5 \pm 0.1} \text{ W Hz}^{-1}$.
- We find that radio-detected LAEs have a median radio spectral index (α) of $-1.3_{-1.5}^{+0.4}$, steeper than the global radio AGN population, which may indicate that they are good sign-posts of over-dense regions (proto-clusters) at high redshift, consistent with the clustering analysis of Khostovan et al. (2019).
- We find no relation between radio and $\text{Ly}\alpha$ luminosities, implying radio is tracing different processes/timescales than $\text{Ly}\alpha$ and X-rays, for the AGN LAEs.

Our results reveal that LAEs at high redshift are mostly star-forming galaxies and that radio LAEs are not fully representative of the radio-selected AGN at similar redshifts. LAEs detected in the radio show properties consistent with residing in over-dense regions, but there is a general lack of correlation between the radio and $\text{Ly}\alpha$, unlike the strong $\text{Ly}\alpha$ -X-ray correlations, likely due to those luminosities tracing very different timescales and consistent with significant AGN variability for AGN LAEs.

Chapter 5

The growth of typical and
luminous Ly α emitters and their
supermassive black holes from
z \sim 2 to z \sim 6

Abstract

We use X-rays, radio and FIR data to evaluate the AGN fraction and SFRs of LAEs and probe the relative growth of LAEs and their super-massive black holes across cosmic time. We find that the global AGN fraction in our sample is $8.6\% \pm 0.4\%$ for $\gtrsim L_{\text{Ly}\alpha}^*$ LAEs ($L_{\text{Ly}\alpha}^*$ is the characteristic Ly α luminosity). The global AGN fraction rises with Ly α luminosity and declines with increasing redshift. We estimate the median star formation rate of star-forming LAEs from Ly α and radio luminosities and find them to be comparable, with a median overall SFR of $7.2_{-2.8}^{+6.6} M_{\odot} \text{ yr}^{-1}$. We also estimate the Ly α escape fraction with our radio SFRs and obtain an $f_{\text{esc}} = 0.7 \pm 0.3$, in excellent agreement with the predictions of Sobral & Matthee (2019). The black hole to galaxy growth ratio (BHAR/SFR) for LAEs is < 0.0016 , consistent with typical star forming galaxies and the local BHAR/SFR relation. We conclude that LAEs at $2 < z < 6$ include two different populations: an AGN population, where Ly α luminosity traces BHAR, making them bright in Ly α , and another with low SFRs which remain undetected in even the deepest X-ray stacks but is detected in the radio stacks.

Calhau, J., Sobral, Santos, S., Matthee, J., Paulino-Afonso, A., Stroe, A., Simmons, B., Barlow-Hall, C., Adams, B., 2020, MNRAS, 493, 3

5.1 Introduction

Several studies have investigated the interplay and evolution of the central supermassive black holes and their host galaxies. Observations reveal that galaxies were undergoing significantly higher star formation rates in the past, with the star formation rate density reaching a peak around $z \sim 2 - 3$ (e.g. Khostovan et al., 2015; Lilly et al., 1996; Sobral et al., 2013). Such peak seems to be roughly coincident with the highest point in the SMBH activity (black hole accretion rates, BHAR, e.g. Calhau et al., 2017; Delvecchio et al., 2014; Madau & Dickinson, 2014; Shankar et al., 2009), suggesting a link between them. However, the connection between SFR and BHAR remains unclear and simulations still find different correlations for these two quantities based on the selection methods used for the samples (e.g. McAlpine et al., 2017).

When studying the relation between SFRs and BHARs, different strategies are employed. One approach is to study samples selected due to their clear active galactic nuclei signatures, typically strong X-ray (2-8 keV) emission (e.g. Harrison et al., 2012; Lutz et al., 2010; Mullaney et al., 2012b; Stanley et al., 2015). These samples show varying results depending on the luminosity of the sources, with low luminosity samples ($L_{2-8\text{keV}} < 10^{44} \text{ erg s}^{-1}$) showing no correlation between BHAR and SFR (e.g. Azadi et al., 2015; Mullaney et al., 2012a; Stanley et al., 2015), while high luminosity samples ($L_{2-8\text{keV}} > 10^{44} \text{ erg s}^{-1}$) show either positive (e.g. Lutz et al., 2010), negative (e.g. Page et al., 2012) or no correlation at all (e.g. Azadi et al., 2015; Harrison et al., 2012; Stanley et al., 2015). The differences in the results might be explained by low number statistics and it is worth noting that studies making use of larger samples appear to support the existence of a flat relation between BHAR and SFR at higher X-ray luminosities (e.g. Azadi et al., 2015; Stanley et al., 2015). This has been interpreted as, for example, a result of the high variability of AGN activity weakening any observable relation between the SFR and AGN luminosity (e.g. Stanley et al., 2015), or due to an underlying connection such as a common gas reservoir for both AGN and SFR (Azadi et al., 2015). Another explanation might be that, although SFR and BHAR trace each other at the early stages of galaxy evolution, that relation does not continue past a certain point in the galaxy's life. An example of this is the work of Ferré-Mateu

et al. (2015), who found eight massive outlier galaxies in the local $M_{\text{BH}}-M_{\text{bulge}}$ relation and explain them as relics from the $z \sim 2$ Universe whose extremely large SMBHs are completely formed by this redshift and whose host galaxies remain structurally the same and without further growth (see also Barber et al., 2016).

An alternative strategy is to study the BHARs of star forming-selected galaxies, which allows for the study of galaxy samples without requiring clear AGN activity. Studies focusing on SFGs consistently find that the BHAR/SFR ratio stays relatively constant across redshift (e.g. Calhau et al., 2017; Delvecchio et al., 2015; Rafferty et al., 2011). A possible explanation is that the relation is due to the BHARs being dependent on the content of dense molecular gas of the host galaxies and, as such, BHARs and SFRs broadly trace each other across cosmic time.

Integral field unit and narrow band surveys have now detected large numbers of $\text{Ly}\alpha$ emitters at $2 < z < 6$, of which several are completely undetected in photometric broad-band surveys. This is consistent with faint LAEs of low mass, blue and with low metallicity (Bacon et al., 2015; Karman et al., 2015; Nakajima et al., 2016; Sobral et al., 2015, 2019). However, studies at $z \sim 2$ find a second population of $\text{Ly}\alpha$ sources which are massive, dusty and red (Chapman et al., 2005; Matthee et al., 2016; Oteo et al., 2012a, 2015; Sandberg et al., 2015). At lower redshifts ($z < 3$) luminous $\text{Ly}\alpha$ emitters appear more AGN-dominated (Cowie et al., 2010; Sobral et al., 2018b; Wold et al., 2014), but most may still be considered analogous to $z > 3$ LAEs (Erb et al., 2016; Oteo et al., 2012b; Trainor et al., 2016) and the distinction between these two likely depends on the $\text{Ly}\alpha$ luminosity, likely due to a maximal observable unobscured $\text{Ly}\alpha$ luminosity at $\text{SFR} \sim 20 M_{\odot} \text{ yr}^{-1}$ (e.g. Sobral et al., 2017, 2018a).

Despite evidence that at $z = 2 - 3$ luminous LAEs ($L_{\text{Ly}\alpha} \gtrsim 10^{43} \text{ erg s}^{-1}$) are mostly associated with the presence of AGN (e.g. Konno et al., 2016; Ouchi et al., 2008; Sobral et al., 2017), the limiting X-ray sensitivity makes it impossible to probe the nature of lower luminosity $\text{Ly}\alpha$ emitters source by source. Matthee et al. (2017a), for example, reported X-ray fractions as high as $\sim 80\%$ of luminous $\text{Ly}\alpha$ emitters as AGN ($L_{2-8\text{keV}} > 3 \times 10^{44} \text{ erg s}^{-1}$ and $L_{\text{Ly}\alpha} > 10^{44} \text{ erg s}^{-1}$), while Sobral et al. (2018b) showed that such fractions are likely just a lower limit, with the AGN fraction of luminous LAEs being even higher. However, little is

known about the potential AGN activity of fainter populations of LAEs. It is uncertain how the AGN fraction of LAEs might evolve with redshift, and whether the transition Ly α luminosity between dominant SF and AGN LAEs evolves with redshift.

In this Chapter, we join the conclusions and results drawn from the X-rays and radio in the previous two Chapters and join them with the SFR measurements from FIR, Ly α and radio and study the evolution of the AGN fraction and the BHAR/SFR ratio in star-forming galaxies at redshifts $z \sim 2 - 6$.

5.2 Methodology

5.2.1 SFRs of LAEs

5.2.1.1 FIR SFRs and upper limits

We explore the public Jin et al. (2018) COSMOS catalogue with de-blended FIR photometry (100, 160, 250, 350 and 500 μm) in order to obtain the fluxes for the LAEs detected in the FIR (see further details in Santos et al., 2020). We use those fluxes and fit them for each of the 46 LAEs detected in at least one FIR band. We explore a range of modified black-bodies (grey-bodies; see details in e.g. Calhau et al., 2017). We then fit the modified black-bodies between rest-frame 100 μm and 850 μm and integrate between 8 and 1000 μm to obtain the total FIR luminosity, after using the corresponding luminosity distance of each LAE. We convert the luminosity to SFRs by using:

$$\text{SFR}_{\text{IR}} = L_{\text{IR}} \times 2.5 \times 10^{-44} (\text{M}_{\odot} \text{ yr}^{-1}) \quad (5.1)$$

where L_{IR} is the luminosity obtained from integrating the grey-body templates (e.g. Ibar et al., 2013, converted to Chabrier IMF). We also compare our SFRs and FIR luminosities with those presented in Jin et al. (2018), finding a good agreement on average and within the errors, with differences mostly arising from sources with just one FIR detection per source.

5.2.1.2 Radio SFRs

We determine the radio SFRs from the 1.4 GHz luminosities by adopting the calibration used by Yun et al. (2001), converted to a Chabrier IMF (see Karim et al., 2011):

$$\text{SFR}_{1.4\text{ GHz}} = 3.18 \times 10^{-22} L_{1.4\text{ GHz}} (\text{M}_{\odot} \text{ yr}^{-1}) \quad (5.2)$$

We only estimate radio SFRs for the stacks where LAEs directly detected in the radio are excluded, in order to avoid contamination by radio AGN emission.

5.2.1.3 Ly α SFRs

We also estimate the SFRs of LAEs by following Sobral & Matthee (2019) and using a Chabrier IMF:

$$\text{SFR}_{\text{Ly}\alpha} [\text{M}_{\odot} \text{ yr}^{-1}] = \begin{cases} \frac{L_{\text{Ly}\alpha} \times 4.4 \times 10^{-42}}{0.042 \text{EW}_0} & \text{EW}_0 < 210 \text{ \AA} \\ 4.98 \times 10^{-43} \times L_{\text{Ly}\alpha} & \text{EW}_0 > 210 \text{ \AA} \end{cases} \quad (5.3)$$

where $L_{\text{Ly}\alpha}$ is the observed Ly α luminosity in erg s^{-1} and EW_0 is the Ly α rest-frame equivalent width in \AA . The SFRs obtained this way should already be corrected for dust extinction as part of the calibration (see Sobral & Matthee, 2019, for a detailed explanation).

5.2.1.4 Estimating the Ly α escape fraction from EW_0 and radio

We follow Sobral & Matthee (2019) and estimate the escape fraction of Ly α photons (f_{esc}) from the median Ly α EW_0 , by using:

$$f_{\text{esc}} = 0.0048 \times \text{EW}_0 \quad (5.4)$$

where EW_0 is the median Ly α equivalent width (see full details and the physical interpretation in Sobral & Matthee, 2019). With this method we obtain $f_{\text{esc}} = 0.67_{-0.34}^{+0.33}$ (where the errors are the 68% confidence region), for the full SC4K sample with a median EW_0 of $138_{-70}^{+282} \text{ \AA}$.

Using our radio SFRs, we can also estimate the Ly α f_{esc} by simply assuming that $\text{SFR}_{1.4\text{GHz}} = \text{SFR}_{\text{H}\alpha}$, which leads to:

$$f_{\text{esc}} = \frac{L_{\text{Ly}\alpha} \times 4.4 \times 10^{-42}}{8.7 \times \text{SFR}_{1.4\text{GHz}}} \quad (5.5)$$

where $L_{\text{Ly}\alpha}$ is the observed Ly α luminosity in erg s^{-1} and $\text{SFR}_{1.4\text{GHz}}$ is the radio star formation rate in $M_{\odot} \text{yr}^{-1}$.

5.3 The SFRs of LAEs

5.3.1 FIR SFRs

A total of 46 LAEs are individually detected in at least one of the FIR bands (100, 160, 250, 350 and $500 \mu\text{m}$) in Jin et al. (2018). We use the fluxes from Jin et al. (2018) and estimate the associated SFR_{IR} following Section 5.2.1.1. The average (median) SFR_{IR} of FIR detected LAEs stands at $340_{-260}^{+290} M_{\odot} \text{yr}^{-1}$ ($200_{-110}^{+430} M_{\odot} \text{yr}^{-1}$). Most (31 of 46, 67%) of the FIR-detected LAEs have SFRs of 30-300 $M_{\odot} \text{yr}^{-1}$, with only 6 (13%) having SFRs $> 600 M_{\odot} \text{yr}^{-1}$ and the remaining 20% having values in between 300 and 600 $M_{\odot} \text{yr}^{-1}$.

We also stack our LAEs in the five FIR bands and recover SFR upper-limits of 30, 45 and 300 $M_{\odot} \text{yr}^{-1}$ for the redshift ranges of $2.2 < z < 2.7$, $2.7 < z < 3.5$ and $3.5 < z < 5.8$. Our direct detections stand above these limits, with average SFRs of 114, 320 and 900 $M_{\odot} \text{yr}^{-1}$ for the same redshift ranges. It is also worth noting that 35 out of the 46 LAEs (76%) with at least one FIR detection are X-ray or radio AGN LAEs. In summary, most ($\sim 99\%$) LAEs remain undetected in the de-blended FIR catalogue of Jin et al. (2018) and they also remain undetected once stacked, implying SFRs below a few tens of $M_{\odot} \text{yr}^{-1}$.

5.3.2 Radio SFRs

Stacking all SC4K LAEs in the 3 GHz band (excluding radio LAEs; see Section 4.4.2) in the radio results in an average SFR of $9.3_{-2.4}^{+3.0} M_{\odot} \text{yr}^{-1}$ and a median of

$8.6_{-2.0}^{+2.5} M_{\odot} \text{ yr}^{-1}$, well under the limits imposed by the FIR stacking measurements. We are able to further split the sample in redshift bins. For $2.2 < z < 2.7$ and $2.7 < z < 3.5$, our radio stacking yield average SFRs of $9.0_{-2.5}^{+3.0}$ and $10.6_{-3.2}^{+4.1} M_{\odot} \text{ yr}^{-1}$, respectively (see Tables 3.1 and A.4), and corresponding median SFRs of $8.4_{-1.6}^{+1.7}$ and $9.7_{-2.9}^{+3.4} M_{\odot} \text{ yr}^{-1}$. For $z > 3.5$ we find a mean (median) upper-limit of < 43.5 (37.4) $M_{\odot} \text{ yr}^{-1}$. We also obtain radio stacks in terms of Ly α luminosity, measuring higher radio SFRs for higher Ly α luminosities (see Table A.4).

5.3.3 Ly α SFRs

We estimate our Ly α SFRs (Section 5.2.1.3) by excluding AGN (radio and X-ray) from the sample, because Ly α emission may be coming from the accretion process of the SMBHs for these sources and result in a biased SFR measurement when not excluded (see Section 3.4.2). We obtain a median SFR of $6.0_{-2.7}^{+7.0} M_{\odot} \text{ yr}^{-1}$ for the entire SC4K sample. Santos et al. (in prep.) estimates the SFRs of LAEs by making use of both the recipe from Sobral & Matthee (2019) and by using MAGPHYS (da Cunha et al., 2008) to obtain SED-derived SFRs, finding a median $\text{SFR}_{\text{Ly}\alpha} = 5.7_{-2.6}^{+7.0} M_{\odot} \text{ yr}^{-1}$ and a median $\text{SFR}_{\text{SED}} = 4.5_{-2.6}^{+9.5} M_{\odot} \text{ yr}^{-1}$, fully consistent with our results and confirming the low SFRs of SC4K LAEs.

We also split the sample in three different redshift bins, finding similar SFRs with medians of $4.1_{-1.9}^{+3.7}$, $6.0_{-2.5}^{+5.3}$ and $9.8_{-5.2}^{+9.7} M_{\odot} \text{ yr}^{-1}$ for LAEs at $2.2 < z < 2.7$, $2.7 < z < 3.5$ and $z > 3.5$, respectively (see also Table 3.1).

5.3.4 SFR comparison and Ly α escape fraction from radio SFR

The derived SFRs from different methods produce consistent results for the SC4K LAEs. In particular, the median Ly α SFRs and the median radio SFRs reveal excellent agreement with $\text{SFR}_{\text{Ly}\alpha} = 6.0_{-2.7}^{+7.0} M_{\odot} \text{ yr}^{-1}$ and $\text{SFR}_{1.4 \text{ GHz}} = 8.6_{-2.0}^{+2.5} M_{\odot} \text{ yr}^{-1}$. In this work, we take the average between the Ly α -derived values and the radio-derived values (if available) as the SFRs¹ of LAEs. For the full sample, we

¹The errors in the combined SFR are estimated by applying standard error propagation. For the highest redshift LAEs we use the SFR from Ly α only.

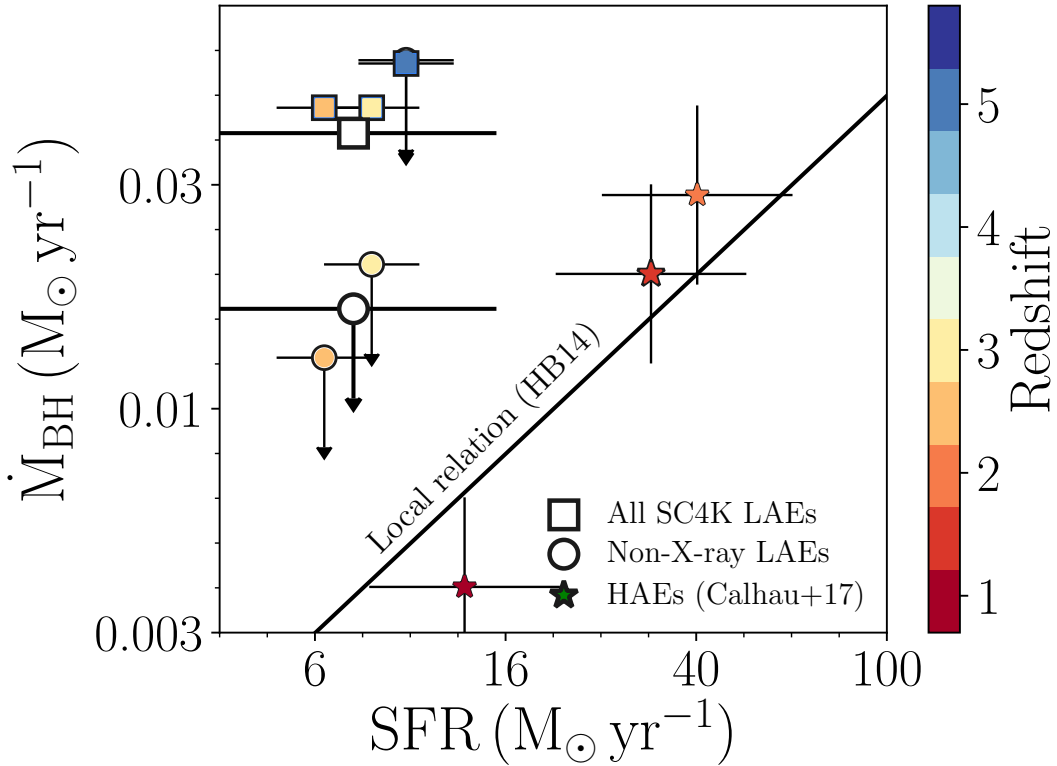


Figure 5.1: The average star formation rate of LAEs versus their average black hole accretion rate. The square markers present the results including X-ray LAEs, while the circles show the results excluding those sources. The data points are coloured following the median redshift of the respective stack. The white markers are the stacks for the entire redshift range of the sample ($z = 2 - 6$) including all LAEs (square) and excluding X-ray LAEs (circle). We compare our results with a similar analysis of H α selected SF galaxies from HiZELS (see Calhau et al., 2017). The black line represents the local relation between the BHAR and SFR of galaxies, taken from Heckman & Best (2014). Our results show that the non-AGN LAEs likely have BHAR/SFR ratios consistent with BH-galaxy co-evolution at much lower SFRs than the typical H α emitters. However, AGN LAEs are growing their super-massive black holes at significantly higher rates, many times above the local relation. Errors were estimated by taking the 68% confidence intervals.

find a $\text{SFR} = 7.2_{-2.8}^{+6.6} \text{ M}_{\odot} \text{ yr}^{-1}$.

The availability of radio SFRs allows us to estimate the $\text{Ly}\alpha$ escape fraction for SC4K LAEs. We use equation 5.5 using the observed median $\text{Ly}\alpha$ luminosity and obtain a $\text{Ly}\alpha f_{\text{esc}} = 0.5 \pm 0.2$. We can also estimate f_{esc} with equation 5.4 (Sobral & Matthee, 2019) and obtain $f_{\text{esc}} = 0.7 \pm 0.3$, showing a good agreement within the uncertainties. Our results represent the first time radio has been used to determine the escape fraction of high- z LAEs and that the Sobral & Matthee (2019) calibration can be tested with an independent method at high redshift (see also Santos et al., 2020).

5.4 Is there a BH-galaxy co-evolution in LAEs? AGN fractions, SFRs and BHAR/SFR

In total, out of 3700 LAEs, 314 are classified as AGN due to their detection in the X-ray full band or one of the radio bands. Of the 314 AGN LAEs, 254 are detected in the X-rays. We also identify 116 galaxies with detectable radio emission. This results in a total LAE AGN fraction of $8.5\% \pm 0.4\%$ (errors are binomial counting errors). We stress that this is a lower limit as there may be AGN in our sample that are too faint to be detected (e.g. Sobral et al., 2018b).

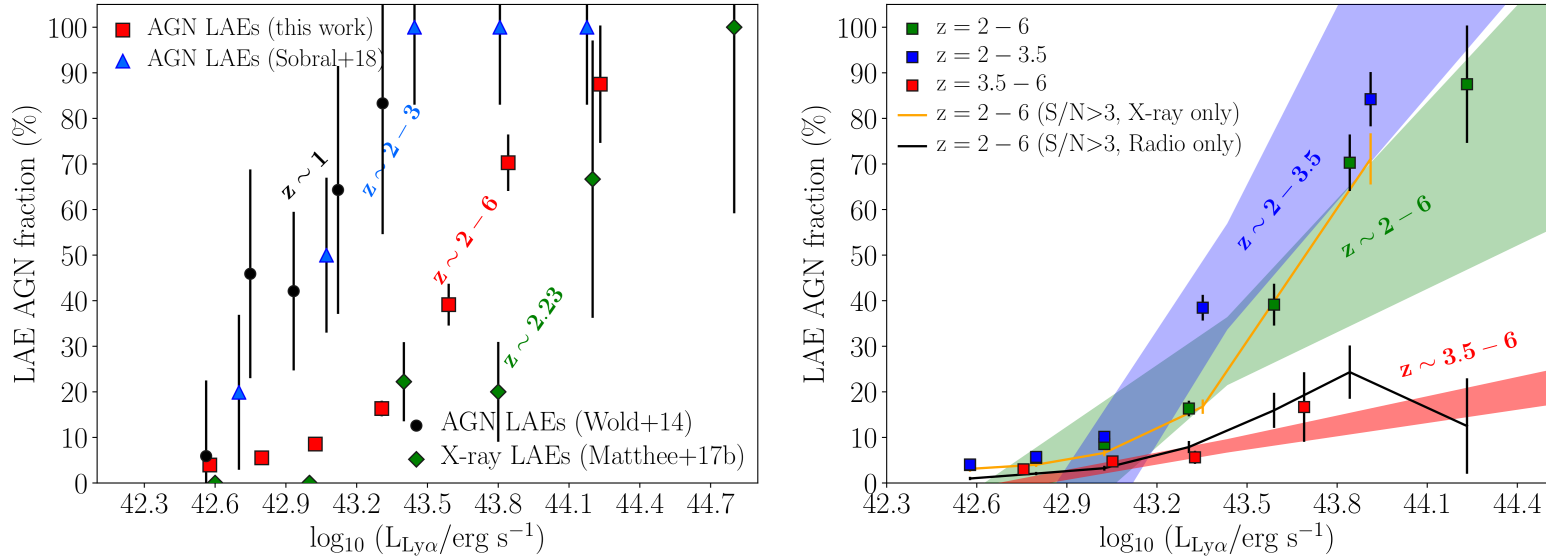


Figure 5.2: *Left:* The LAE AGN fraction rises steeply with increasing Ly α luminosity for our full sample, revealing that the most luminous LAEs are almost all AGN. Our results are in agreement with those found in the literature. *Right:* The evolution of the AGN fraction for the entire sample (green) and for LAEs at $z = 2 - 3.5$ (blue) and $z = 3.5 - 6$ (red). We find a significant redshift evolution of the AGN fraction as a function of Ly α luminosity. The fraction growth is much steeper at lower redshifts than at $3.5 < z < 6$. The shaded regions represent the 16th-86th percentiles of linear fits obtained when the Ly α luminosity bins and bin widths are varied randomly. The errorbars are binomial counting errors. We also show that the rise is dominated by X-ray LAEs, while the radio AGN fraction still rises with Ly α luminosity, but at a much shallower rate.

5.4.1 AGN fraction and its redshift evolution

The X-ray AGN fraction for LAEs is found to be $7.3\% \pm 0.8\%$ at $z \sim 2.2 - 2.7$ and $7.9\% \pm 0.5\%$ at $z \sim 2.7 - 3.5$. At $z > 3.5$, the X-ray AGN fraction of LAEs drops to $3.5\% \pm 0.6\%$. The decline at higher redshift is found regardless of the signal-to-noise cut employed or whether we use Civano et al. (2016)'s catalogue (see Table 5.1 for full details).

The total radio AGN fraction of LAEs is $3.1\% \pm 0.3\%$. We find that the radio AGN fraction remains relatively constant at $\sim 3.4\%$ at $z \sim 2.2 - 3.5$, before falling towards $2.0\% \pm 0.5\%$ at $z \sim 3.5 - 5.8$. We note that the uncertainties in the AGN fractions allow for the fractions to remain constant or even rise slightly between $z = 2.2$ and $z = 5.8$ in all cases (3σ cut, 5σ cut and Smolčić et al. 2017's catalogue, see Table 5.1). The radio AGN fraction among LAEs shows a much flatter evolution with redshift than the X-ray AGN fraction.

Overall, the AGN fraction of LAEs stays relatively constant up to $z \sim 3.5$, from $9.1\% \pm 0.9\%$ at $z \sim 2.2 - 2.7$ to $9.6\% \pm 0.6\%$ at $z \sim 2.7 - 3.5$ before dropping by a factor of almost 2 to $4.9\% \pm 0.7\%$ at $z \sim 3.5 - 5.8$ (see Tables 3.1 and 5.1). Using a higher S/N cut (or the Civano et al. (2016) and Smolčić et al. (2017) catalogues) leads to an even sharper decline of the AGN fraction at the highest redshifts, but the qualitative result is the same.

5.4.2 The AGN fraction dependence on Ly α luminosity

5.4.2.1 Global AGN fraction: global rise with Ly α

Figure 5.2 presents how the full LAE AGN fraction (radio + X-rays) varies as a function of increasing Ly α luminosity for SC4K LAEs. The global AGN fraction clearly rises with $L_{\text{Ly}\alpha}$, to the point where the most luminous LAEs are almost, if not all, AGN. In practice, the AGN fraction rises from $\sim 0 - 5\%$ to $\sim 80 - 100\%$ from $L_{\text{Ly}\alpha} \sim 10^{42.6} \text{ erg s}^{-1}$ to $L_{\text{Ly}\alpha} \sim 10^{44.4} \text{ erg s}^{-1}$ at $z \sim 2 - 6$.

The left panel of Figure 5.2 compares our results with other recent studies. Matthee et al. (2017a) conducted a similar analysis to ours, albeit with shallower X-ray and Ly α data. They find a very similar rise in the (X-ray) AGN fraction as a function of Ly α luminosity at $z \sim 2.2$. Matthee et al. (2017a) also notes that

Table 5.1: The evolution of the LAE X-ray and radio detected AGN fractions with redshift. We present the results obtained by selecting sources with a $S/N > 3$, $S/N > 5$ and also by using only the sources detected in Civano et al. (2016) and Smolčić et al. (2017) catalogues as AGN LAEs. We find a general drop in the AGN fraction at the highest redshifts. This drop is particularly steep towards $z \sim 3.5 - 6$ when using the high significance detection catalogues of Civano et al. (2016) and Smolčić et al. (2017) and our own analysis with $S/N > 5$. Radio AGN fractions show a flatter evolution overall when compared to X-ray LAEs. Our AGN fractions should be interpreted as lower limits as there could be undetected AGN in both radio and X-ray bands. All errors are binomial counting errors.

X-ray LAEs	AGN fraction (%)		
Sample	$2 < z < 2.7$	$2.7 < z < 3.5$	$3.5 < z < 6$
This Work (3σ)	7.3 ± 0.8	7.9 ± 0.5	3.5 ± 0.6
This Work (5σ)	5.2 ± 0.7	5.1 ± 0.5	0.8 ± 0.3
Civano et al.(2016)	3.9 ± 0.6	3.5 ± 0.4	0.4 ± 0.2
Radio LAEs	AGN fraction (%)		
Sample	$2 < z < 2.7$	$2.7 < z < 3.5$	$3.5 < z < 6$
This Work (3σ)	3.8 ± 0.6	3.3 ± 0.4	1.9 ± 0.5
This Work (5σ)	1.3 ± 0.4	1.2 ± 0.2	0.8 ± 0.3
Smolčić et al.(2017)	1.9 ± 0.5	1.7 ± 0.3	0.8 ± 0.3
Radio+X-ray LAEs	AGN fraction (%)		
Sample	$2 < z < 2.7$	$2.7 < z < 3.5$	$3.5 < z < 6$
This Work (3σ)	9.1 ± 0.9	9.6 ± 0.6	4.9 ± 0.7
This Work (5σ)	5.5 ± 0.7	5.6 ± 0.5	2.5 ± 0.5

the increase in the fraction corresponds to the luminosity at which the number densities start to deviate from the Schechter function (see also Konno et al., 2016; Sobral et al., 2017), which is fully captured and discussed at multiple redshifts by Sobral et al. (2018a). Wold et al. (2014, 2017) used spectroscopy to classify LAEs at $z \sim 1$, finding a similar relation which is offset to much higher AGN fractions for a fixed Ly α luminosity. This could be interpreted as a redshift evolution, but as shown by Sobral et al. (2018b) that is likely not the explanation. Sobral et al. (2018b) followed-up spectroscopically (using rest-frame UV lines and photo-ionisation modelling) a sample of the most luminous $z \sim 2 - 3$ LAEs to find a very similar relation (including the normalisation) to Wold et al. (2014, 2017), consistent with no redshift evolution from $z \sim 1$ to $z \sim 2 - 3$. Instead, Sobral et al. (2018b) show how X-ray data only allow to estimate lower limits for the AGN fraction at high redshift. Their results show that essentially all LAEs with $L_{\text{Ly}\alpha} > 10^{43.3} \text{ erg s}^{-1}$ are AGN. This rise is extremely fast as can be seen in Figure 5.2.

5.4.2.2 X-ray and radio AGN fractions as a function of Ly α

We find that the X-ray AGN fraction on its own rises steeply with Ly α luminosity, from $3.6\% \pm 0.7\%$ at $L_{\text{Ly}\alpha} \sim 10^{42.7} \text{ erg s}^{-1}$ to $70\% \pm 5\%$ at $L_{\text{Ly}\alpha} \sim 10^{43.7} \text{ erg s}^{-1}$ (see the right panel of Figure 5.2). At the highest Ly α luminosities, most LAEs become detected by *Chandra*, showing that AGN detected in the X-rays dominate the sample at high Ly α luminosities. These results are also qualitatively observed if we restrict the sample to the $S/N > 5$ X-ray detections or use Civano et al. (2016)'s catalogued sources.

The radio AGN fraction of LAEs shows a flatter rise with Ly α luminosity (see Figure 5.2), reflecting the different L_X - $L_{\text{Ly}\alpha}$ and L_{radio} - $L_{\text{Ly}\alpha}$ relations we find for LAEs (see Sections 3.4.3 and 4.4.3). The radio AGN fraction of LAEs remains relatively low for most of Ly α luminosity bins, only growing to 25-30% for the highest Ly α luminosities. The results support a radio AGN fraction that rises with Ly α luminosity but with a shallower slope and a much lower normalisation. Interestingly, we also find that the rise of the radio AGN population for the highest Ly α luminosities is driven by the inclusion of radio sources which are also

X-ray sources. Restricting the AGN fraction to pure radio sources which remain undetected in the X-rays results in an even lower radio AGN fraction with the highest values only reaching $\sim 5\%$ even at the highest Ly α luminosities.

5.4.2.3 The rise of the LAE AGN fraction with Ly α evolves with redshift

Sobral et al. (2018b) discuss the possibility of the LAE AGN fraction being much lower at fixed observed Ly α luminosity towards higher redshifts (particularly based on results from Matthee et al., 2017b,c) and the physical implications/interpretations. We can investigate this possibility for the first time by splitting our sample into a higher and lower redshift sub-sample. Figure 5.2 (right panel) shows our results. We find that the LAE AGN fraction increases with Ly α luminosity at both $z \sim 2 - 3.5$ and $z \sim 3.5 - 6$, but shows significant evolution as suggested by Sobral et al. (2018b). The AGN fraction is higher and seems to rise more steeply with increasing Ly α luminosity at $z \sim 2 - 3.5$ than at $z \sim 3.5 - 6$. While at $z \sim 2 - 3.5$ virtually all LAEs with Ly α luminosities in excess of 10^{44} erg s $^{-1}$ are (X-ray or radio) AGN, by $z \sim 3.5 - 6$ the measured AGN fraction is only $\sim 10\%$. While it is harder to detect AGN with X-rays and radio at higher redshift, the strong redshift evolution is much stronger than expected simply based on a detection bias. The decrease in the AGN fraction with redshift, for a fixed Ly α luminosity, may be due to the fact that the BH accretion rate density of X-ray AGN drops significantly for $z > 3$ (e.g. Vito et al., 2016) or due to the high fraction of obscured AGN population at high redshifts ($> 50\%$ at $z > 3$ and increasing with redshift, see e.g. Vito et al., 2014).

Sobral et al. (2018b) argue that the relation between the AGN fraction of LAEs and their observed luminosity at $z \sim 2-3$ (and the steepness of the relation) is caused by star-forming galaxies having a maximum observable unobscured Ly α (and UV) luminosity, which seems to correspond to a SFR of $\approx 20 M_{\odot} \text{ yr}^{-1}$. Galaxies with higher SFRs exist in large numbers and will have higher intrinsic luminosities but dust extinction reduces the observable flux in a non-linear way, resulting in a limit to the observed luminosity. The reason why AGN become prevalent above this limit is because the physics of Ly α (and UV) production

and escape is able to scale up much higher without dust limiting it. If this is the case, then the evolution of the AGN LAE fraction towards lower values, or towards higher Ly α observed luminosities, may imply that at high redshift galaxies can form stars at higher rates without dust limiting the observed Ly α luminosity. There is evidence for the brightest LAEs at $z \sim 7$ being mergers unobscured by dust, while structures with similar Ly α luminosity at $z = 2 - 3$ show heavy obscuration (see e.g. Matthee et al., 2019). This might be possible under much more metal poor conditions, together with hard and intense radiation fields that limit dust production or even destroy dust very effectively, with consequences for even the escape of LyC photons at high redshift. Another competing effect may be the reduction of the number of AGN LAEs which may happen faster than the decline in the number density of SF-powered LAEs for a given observed Ly α luminosity. These scenarios can only be fully explored and tested with future deep rest-frame UV and optical spectroscopy of luminous LAEs at high redshift (Sobral et al., 2018b).

5.4.3 The black hole-to-galaxy growth of LAEs

Having determined the BHARs and SFRs for different sub-samples of LAEs, we can attempt to investigate the relative black hole-to-galaxy growth of LAEs and any evolution with redshift. We show the results in Figure 5.1. Considering the full sample of LAEs, we find a very high BHAR for the SFR inferred. However, this is mostly because the population of LAEs is made of 1) a bulk of SF galaxies with low SFRs which dominate the numbers and SFRs and 2) a small fraction of X-ray AGN LAEs which dominate the X-ray emission and become dominant at high Ly α luminosities and towards $z \sim 2$. Indeed, if we exclude the X-ray LAEs, our results suggest that the bulk of LAEs (without X-ray emission) are consistent with co-evolution between their super-massive black holes and their stellar populations (Figure 5.1).

We can further quantify our results by computing and interpreting the BHAR/SFR ratio of each sub-population (see Table 3.1). For the entire LAE sample (including the X-ray LAEs) we find an average BHAR/SFR ≈ 0.005 , eight times higher than what is expected for the local relation (BHAR/SFR ≈ 0.0006 , see Heckman

& Best, 2014, and Figure 5.1). Excluding the X-ray LAEs from the sample results in a lower ratio of $\text{BHAR}/\text{SFR} < 0.0022$, only a factor 3.5 from what one would expect to establish the local relation in a co-evolution scenario between the growth of the super massive black hole and the host galaxy.

We find that the typical BHAR/SFR for LAEs decreases with redshift by a factor of just over 3. We find $\text{BHAR}/\text{SFR} \approx 0.007$ for $z \sim 2.2 - 2.7$, decreasing to $\text{BHAR}/\text{SFR} \approx 0.005$ at $z \sim 2.7 - 3.5$ and $\text{BHAR}/\text{SFR} < 0.006$ at $z \sim 3.5 - 6$. When excluding X-ray LAEs we can only obtain upper limits, so we are not able to investigate any potential evolution.

In Figure 5.1 we also compare our results for LAEs with the results of Calhau et al. (2017) for $\text{H}\alpha$ emitters at $0.8 < z < 2.2$. Our LAEs have, on average, BHARs comparable to those of $\text{H}\alpha$ emitters at $0.8 < z < 1.5$, while the SFRs of $\text{Ly}\alpha$ emitters are around an order of magnitude smaller than that of $\text{H}\alpha$ emitters. The average relative black hole-to-galaxy growth ratio for all LAEs is much higher than for all $\text{H}\alpha$ emitters. However, when excluding X-ray LAEs the LAE population may well be fully consistent with the BHAR/SFR ratios measured for the highly star-forming $\text{H}\alpha$ selected sources (see Figure 5.1), but with LAEs having significantly lower SFRs.

5.5 Conclusions

We have studied the X-ray and radio properties of 3700 LAEs ($\text{Ly}\alpha$ Emitters) at $2 < z < 6$ from the SC4K sample (Sobral et al., 2018a), and investigated the possible relations between those quantities and $\text{Ly}\alpha$. We made use of the publicly available data from COSMOS to stack the sample and get the average X-ray luminosity and BHAR of LAEs. We also explore the radio properties of LAEs and use the available data from VLA-COSMOS to also stack the sample in the radio and estimate the SFR and radio properties of typical LAEs. Our main results are:

- The AGN fraction of LAEs increases significantly with $L_{\text{Ly}\alpha}$, with the brightest LAEs being AGN dominated. The correlation is found at all redshifts, but it is found to evolve towards lower AGN fractions at higher

redshift, for a fixed Ly α luminosity. This could be due to a shift towards higher values in the maximal observed unobscured Ly α luminosity, as proposed and discussed by Sobral et al. (2018b).

- The X-ray AGN fraction drives the global AGN fraction dependence on Ly α luminosity. The radio AGN fraction remains relatively low with increasing Ly α luminosity and only grows significantly at the highest Ly α luminosities.
- We are able to estimate SFRs for SC4K LAEs from radio stacking, yielding $8.6^{+2.5}_{-2.0} M_{\odot} \text{ yr}^{-1}$, and from Ly α , resulting in $6.0^{+7.0}_{-2.7} M_{\odot} \text{ yr}^{-1}$, fully consistent with the upper limits we obtain with FIR *Herschel* data.
- We estimate the Ly α escape fraction of SC4K LAEs from radio SFRs (excluding AGN), obtaining $f_{\text{esc}} = 0.5 \pm 0.2$. We find that this is in agreement with what we obtain using Sobral & Matthee (2019) and the Ly α EW₀ ($f_{\text{esc}}(\text{EW}) = 0.7 \pm 0.3$).
- The full population of LAEs as a whole is growing their super-massive black holes at a relative faster rate than their host galaxies, but this is driven by a small fraction of the LAE population which is detected in the X-rays. Excluding X-ray sources, LAEs have a black hole-to-galaxy growth ratio of $\log(\dot{M}_{\text{BH}}/\text{SFR}) < -2.7$, comparable to star-forming galaxies at lower redshifts and consistent with a co-evolution between their super-massive black holes and their host galaxies.

Our results reveal that LAEs at high redshift are mostly star-forming galaxies with relatively low median SFRs ($7.2^{+6.6}_{-2.8} M_{\odot} \text{ yr}^{-1}$) and low AGN activity ($\text{BHAR} < 0.017 M_{\odot} \text{ yr}^{-1}$), but with a few ($6.8\% \pm 0.4\%$) X-ray-bright AGN where the Ly α emission likely comes from the accretion of matter into the central super-massive black hole. These X-ray LAEs become the dominant population among LAEs at the highest Ly α luminosities, but there seems to be an important negative evolution of such population towards high redshift. Radio LAEs are not fully representative of the radio-selected AGN at similar redshifts. LAEs detected in the radio show properties consistent with residing in over-dense regions, but there is a general lack of correlation between the radio and Ly α , unlike the

strong Ly α -X-ray correlations, likely due to those luminosities tracing very different timescales and consistent with significant AGN variability for AGN LAEs. Future studies are required to conduct deep spectroscopic observations of LAEs to unveil even lower BHARs, to establish the redshift evolution even more conclusively, and to identify the physical origins and their consequences for how early galaxies form and evolve.

Chapter 6

Conclusion

This thesis' work characterises the BH activity of star-forming-selected galaxies and compares them to their own star forming activity across cosmic time. In this way, the results presented in this thesis allow for the growth of the understanding on the AGN and star forming processes of star-forming galaxies, particularly line emitters like $H\alpha$ and $Ly\alpha$, as well as helping constrain the co-evolution of SMBH and their host galaxies, enriching the understanding on the processes behind the BH-galaxy correlation found observationally.

6.1 The evolution of SMBH and their star-forming host galaxies since $z \sim 2$

The results of Chapter 2 show that the majority of star-forming galaxies at $z < 2$ has no nuclear activity of note, with only 3% being detected in the X-rays. There also seems to be no significant redshift evolution of the AGN fraction, which remains relatively constant at $\sim 3\%$ from $z = 0.4$ to $z = 2.23$.

The SFRs obtained from FIR measurements are within the expectations for $H\alpha$ SFRs ($\sim 2 M_{\odot} \text{ yr}^{-1}$ at $z = 0.4$ to $\sim 40 M_{\odot} \text{ yr}^{-1}$ at $z = 2.23$), which means $H\alpha$ star-forming galaxies grow 1000 times faster than their SMBHs ($\dot{M}_{\text{BH}} \sim 0.0004 M_{\odot} \text{ yr}^{-1}$ at $z = 0.8$ and $\dot{M}_{\text{BH}} \sim 0.003 M_{\odot} \text{ yr}^{-1}$ at $z = 2.23$).

The $\dot{M}_{\text{BH}}/\text{SFR}$ ratio has little to no evolution with redshift, suggesting a co-evolution of SFR and BHAR across cosmic time and that the processes for fuelling \dot{M}_{BH} and SFR are correlated over cosmic time. The $\dot{M}_{\text{BH}}/\text{SFR}$ ratio also depends very little on the galaxy mass, which might indicate that BH activity and SF activity form a unified mechanism for regulating galaxy growth, as opposed to one mechanism taking over the other at set points in time. This is still, however, very uncertain and further testing is required before a conclusion may be drawn.

6.2 The SMBH activity of star-forming galaxies from $z \sim 2$ to $z \sim 6$ - the X-ray perspective

Chapter 3 begins the task of extending the research of Chapter 2 to higher redshifts by studying the X-ray properties of the star-forming galaxies of SC4K (selected through their Ly α emission from $z \sim 2$ to $z \sim 6$). It shows that the trend of low AGN presence in star-forming galaxies continues at higher redshifts, with only $\sim 6.8\%$ of LAEs being detected in the X-rays. These X-ray-detected LAEs have a hardness ratio consistent with the overall AGN population, with approximately half of them being consistent with obscured sources. This obscured/unobscured ratio seems to remain unchanged throughout the redshifts and Ly α luminosities considered.

The X-ray emission of the AGN LAEs correlates with their Ly α luminosity, suggesting that Ly α becomes a BHAR tracer for X-ray LAEs. However, most LAEs do not show this correlation and retain a low accretion rate of $\dot{M}_{\text{BH}} < 0.017 M_{\odot} \text{yr}^{-1}$, in accordance with the results obtained for lower redshift line-emitting star-forming galaxies shown in Chapter 2.

In summary, Chapter 3 shows that high redshift LAEs are mainly star-forming galaxies with low BHARs and a few X-ray-luminous AGN where Ly α originates from the accretion onto the central supermassive black hole.

6.3 The SMBH activity of star-forming galaxies from $z \sim 2$ to $z \sim 6$ - the radio perspective

The results of Chapter 4 expand on the characterisation of high redshift LAEs by studying the radio properties of SC4K galaxies. Approximately 3% of LAEs are detected in the radio, a low fraction in accordance with the results from X-rays (Chapters 2 and 3). The radio-detected LAEs have 1.4 GHz luminosities consistent with AGN sources. We do not detect radio sources at $z > 5$, though that may be due to sensitivity limits, and cannot individually detect sources in the SF regime at any redshift.

However, in contrast with X-rays, we find significant detections when stacking our sample while excluding radio-detected LAEs, a result we make use of in Chapter 5.

Chapter 4 shows that radio-detected LAEs have a median spectral index α of ~ -1.3 , steeper than the overall AGN population, which may indicate that LAEs at high redshifts reside in over-dense regions (proto-clusters).

6.4 The global perspective: Is there a SMBH-galaxy co-evolution for star forming galaxies?

Chapter 5 connects the results of the previous chapters together by estimating the SFRs of LAEs at $z = 2 - 6$ and then obtaining the $\dot{M}_{\text{BH}}/\text{SFR}$ ratio of LAEs for this redshift range and comparing it to the results of the lower redshift H α emitters.

Joining the results from Chapters 3 and 4, Chapter 5 finds that the global AGN fraction of LAEs increases with Ly α luminosity to the point where the brightest Ly α emitters are AGN dominated. The evolution of the global AGN fraction is driven mainly by the X-ray AGN fraction, with the radio AGN fraction remaining relatively low with increasing Ly α luminosity.

Using FIR, radio and Ly α data, Chapter 5 also presents the SFRs of LAEs. FIR SED fitting can only provide upper limits for the SFRs, as there are no significant detections in the FIR even when using stacking, but radio and Ly α are able to provide actual SFR measurements, with $\text{SFR}_{\text{radio}} \sim 8.6 M_{\odot} \text{yr}^{-1}$ and $\text{SFR}_{\text{Ly}\alpha} \sim 6.0 M_{\odot} \text{yr}^{-1}$, consistent with FIR upper limits.

The population of LAEs at redshifts $z = 2 - 6$ appears to grow their SMBHs faster than the host galaxies, but this is due to the small AGN fraction of LAEs that is detected in the X-rays. Excluding X-ray detected sources, LAEs are star-forming galaxies with low SFR (median of $\sim 7.2 M_{\odot} \text{yr}^{-1}$) and low AGN activity ($\dot{M}_{\text{BH}} < 0.017 M_{\odot} \text{yr}^{-1}$). They present a $\dot{M}_{\text{BH}}/\text{SFR}$ ratio of < -2.7 , comparable to star-forming galaxies at lower redshift, setting up a trend where star-forming galaxies grow approximately 1000 times faster than the SMBHs they host across cosmic time and consistent with a co-evolution between central supermassive black holes and their host galaxies, as this ratio remains relatively constant from $0.4 < z < 6$.

6.5 Closing remarks and future work

Detailed understanding of the possible co-evolution between central supermassive black holes and their host galaxies is still an open objective in extragalactic astrophysics. The main problem resides in the difficulty with observing these sources at high redshift, which results in either populations biased towards the brightest sources (AGN-selected) or with a restrictive number of sources in the sample that are significantly detected, be it directly or through stacking (star-forming-selected).

This study addresses these concerns by using a large (reducing the restriction on the number of sources) star-forming sample (avoiding high luminosity bias) of line emitting galaxies. I conducted a study of the X-ray and radio properties of H α and Ly α line-emitters, which, for the Ly α sample in particular, had not been done before.

The results presented in this thesis provide additional evidence for the co-evolution of galaxies and their supermassive black holes by showing that the

BHAR/SFR ratio remains relatively constant across redshift ($z \sim 0.4 - 3.0$) and further restrict the behaviour of the black hole accretion history at higher redshifts ($z \sim 3 - 6$) by providing upper limits to the BHARs. Our results are in agreement with the findings present in the literature in regards to the BHAR/SFR ratio of star-forming populations (e.g. Delvecchio et al., 2015; Rafferty et al., 2011) and show that the BHAR tracks the evolution of the SFH up to $z \sim 3.0$.

I establish that the vast majority of line emitters are low-to-moderate star-forming galaxies, with little to no AGN activity of note in the X-rays and radio bands. However, I find that, particularly for Ly α emitters, Ly α is correlated to X-ray emission, suggesting that Ly α tracks the BHAR of AGN LAEs. This dual nature of LAEs is observed also at redshifts closer to the local Universe (Dittenber et al., 2020) and the possible AGN origin of Ly α emission may have important implications to our knowledge of the epoch of reionization.

My investigation of the radio characteristics of LAEs allowed me to conclude that LAEs probably reside in over-dense regions, in support of results previous presented in the literature (e.g. Franck & McGaugh, 2016; Khostovan et al., 2019; Klamer et al., 2006). I also use the radio to better constrain the SFR of LAEs and HAEs and, for the first time, use radio-derived SFRs to determine the escape fraction of Ly α and provided an independent test of the Ly α calibration developed by Sobral & Matthee (2019).

In summary, the results presented in this thesis are derived from a large statistical sample and refine and confirm our current understanding of galaxy evolution, AGN/SF related processes at high redshift and, in particular, the characteristics of Ly α emitters in the early Universe. I further contribute to the scientific community with the multiwavelength data accessible through the openly-available catalogues resulting from this work. However, further studies are required to conduct deeper spectroscopic observations to unveil even lower BHARs, establish the redshift evolution more conclusively and further advance our understanding of galaxy formation and evolution and the physical processes behind it.

Possible lines of work include morphological studies in diverse wavelengths, such as X-ray, Radio and Ly α in order to understand where in the galaxies the emissions are originating. This would allow us to, for example, understand

whether or not the X-ray/Ly α relation really is related to Ly α tracing the black hole activity of AGN. Preliminary results show that, for X-ray detected AGN, Ly α and X-rays concentrate on the central area of the galaxies. On the other hand, radio emission can come from a variety of sources, from the central area to more outward, extended regions, due to, probably, shockwaves from relativistic jets. These areas also show Ly α emission and are an example of how diverse the origins of the data we collect can be, in regards to the processes that give it birth.

Future observatories such as the *Athena* and *Lynx* space telescopes will be particularly useful for these questions, as their higher resolution should enable us to better understand the spatial distribution of X-ray emission in AGN, while the higher sensitivity should also enable us to further constrain black hole activity at $z > 3$ and AGN detection at $z > 6$ and further test its possible co-evolution with SFR up to the highest redshifts.

Appendix A

Appendices

A.1 Public Catalogue of SC4K LAEs and Stacking tables

Table A.1 shows the first 3 entries in the catalogue of all SC4K LAEs which we make available with this paper. The complete catalogue includes all LAEs in the study, with X-ray and radio measurements for the LAEs detected in these bands, as well as upper limits for the ones that remain undetected, following the methods described in this study. We also include the measurements from the catalogues from Civano et al. (2016), Smolčić et al. (2017) and FIR fluxes and FIR-derived SFRs from Jin et al. (2018).

We provide, in tables A.4 and A.5, extended stacking results in the X-ray and radio done in this work. All quantities are estimated following the procedures detailed in Sections 3.3.1 (for the X-ray analysis) and 4.3.1 (for the radio analysis). The tables are available online.

Table A.1: Table showing the first 3 transposed entries of the original table of LAEs in our SC4K (adding to Sobral et al., 2018a), fully available online. The uncertainties in the redshifts are taken from the NB or MB filter widths (see Sobral et al., 2018a). The X-ray luminosities were estimated from the full band fluxes available from the *Chandra* Legacy survey full band (0.5 – 7 keV) and converted to the 0.5 – 10 keV band, but we also provide the 0.5 – 2.0 keV and 2.0 – 7.0 keV luminosities. We also show the BHARs as determined from the X-ray luminosities of the sources. The “-99” flag symbolises non-detection or unavailable data. The full public catalogue includes all LAEs in the study, detected and undetected in the X-rays, as well as radio, FIR and Ly α quantities. It also includes the measurements from the catalogues from Civano et al. (2016), Smolčić et al. (2017) and Jin et al. (2018).

	SC4K-NB392-2	SC4K-NB392-6	SC4K-NB392-7
RA	150.676	150.653	150.653
DEC	2.59	2.66	2.54
EW ₀	37.55	116.41	65.86
EW ₀ err _{up}	14.73	159.78	27.36
EW ₀ err _{lo}	11.86	54.73	21.84
Ly α Lum	42.70	42.60	42.77
Ly α Lum err _{up}	0.04	0.05	0.03
Ly α Lum err _{lo}	0.06	0.06	0.05
SFR_SM19	13.9	3.6	9.4
z	2.22	2.22	2.22
flux _(0.5–7.0 keV)	1.03×10^{-15}	1.00×10^{-15}	1.28×10^{-15}
flux _(0.5–7.0 keV) err _{up}	3.4×10^{-16}	3.3×10^{-16}	3.5×10^{-16}
flux _(0.5–7.0 keV) err _{lo}	3.4×10^{-16}	3.3×10^{-16}	3.4×10^{-16}
flux _(2.0–7.0 keV)	1.66×10^{-15}	1.84×10^{-15}	1.20×10^{-15}
flux _(2.0–7.0 keV) err _{up}	5.5×10^{-16}	6.1×10^{-16}	5.0×10^{-16}
flux _(2.0–7.0 keV) err _{lo}	5.5×10^{-16}	6.1×10^{-16}	4.5×10^{-16}
flux _(0.5–2.0 keV)	3.5×10^{-16}	2.13×10^{-16}	2.4×10^{-16}
flux _(0.5–2.0 keV) err _{up}	1.2×10^{-16}	7.0×10^{-17}	1.0×10^{-16}
flux _(0.5–2.0 keV) err _{lo}	1.2×10^{-16}	7.0×10^{-17}	5.6×10^{-17}
Lum _(0.5–10 keV)	2.47×10^{43}	2.42×10^{43}	3.08×10^{43}
Lum _(0.5–10 keV) err _{up}	8.2×10^{42}	8.1×10^{42}	8.5×10^{42}
Lum _(0.5–10 keV) err _{lo}	8.2×10^{42}	8.0×10^{42}	8.2×10^{42}
Lum _(2.0–7.0 keV)	4.0×10^{43}	4.4×10^{43}	3.6×10^{43}
Lum _(2.0–7.0 keV) err _{up}	1.3×10^{43}	1.5×10^{43}	1.20×10^{43}
Lum _(2.0–7.0 keV) err _{lo}	1.3×10^{43}	1.5×10^{43}	1.1×10^{43}
Lum _(0.5–2.0 keV)	2.47×10^{43}	2.42×10^{43}	5.9×10^{42}
Lum _(0.5–2.0 keV) err _{up}	2.8×10^{42}	1.7×10^{42}	2.4×10^{42}
Lum _(0.5–2.0 keV) err _{lo}	2.8×10^{42}	1.7×10^{42}	1.4×10^{42}
Xray HR	0.032	0.328	0.166
Xray HR err _{up}	0.472	0.496	0.522
Xray HR err _{lo}	0.471	0.496	0.386

Table A.2: *Continued from previous table.*

	SC4K-NB392-2	SC4K-NB392-6	SC4K-NB392-7
BHAR	0.09	0.09	0.11
BHAR err _{up}	0.03	0.02	0.03
BHAR err _{lo}	0.03	0.03	0.03
CR _(0.5–7.0 keV)	5.0 ⁻⁵	4.9 ⁻⁵	6.2 ⁻⁵
CR _(2.0–7.0 keV)	-99.0	-99.0	3.9 ⁻⁵
CR _(0.5–2.0 keV)	-99.0	-99.0	2.8 ⁻⁵
BG CR _(0.5–7.0 keV)	3.2 ⁻⁵	2.3 ⁻⁵	3.4 ⁻⁵
BG CR _(2.0–7.0 keV)	2.1 ⁻⁵	1.6 ⁻⁵	2.3 ⁻⁵
BG CR _(0.5–2.0 keV)	7.2 ⁻⁶	7.8 ⁻⁶	6.5 ⁻⁶
Exp time _(0.5–7.0 keV) (s)	154544	127854	172909
Exp time _(2.0–7.0 keV) (s)	159948	126565	169896
Exp time _(0.5–2.0 keV) (s)	144866	125134	166917
DETECT _(0.5–7.0 keV)	false	false	true
DETECT _(0.5–2.0 keV)	false	false	true
DETECT _(2.0–7.0 keV)	false	false	true
S/N _(0.5–7.0 keV)	2.1	-0.5	3.8
S/N _(0.5–2.0 keV)	-99.0	-99.0	4.3
S/N _(2.0–7.0 keV)	-99.0	-99.0	3.4
ID Civano			
fb Civano	-99.0	-99.0	-99.0
fbe Civano	-99.0	-99.0	-99.0
fh Civano	-99.0	-99.0	-99.0
fhe Civano	-99.0	-99.0	-99.0
fs Civano	-99.0	-99.0	-99.0
fse Civano	-99.0	-99.0	-99.0
CIVANO DETECT	false	false	false
F250 Jin+18	-99.0	-99.0	-99.0
DF250 Jin+18	-99.0	-99.0	-99.0
F350 Jin+18	-99.0	-99.0	-99.0
DF350 Jin+18	-99.0	-99.0	-99.0
F500 Jin+18	-99.0	-99.0	-99.0
DF500 Jin+18	-99.0	-99.0	-99.0

Table A.3: *Continued from previous table.*

	SC4K-NB392-2	SC4K-NB392-6	SC4K-NB392-7
F100 Jin+18	-99.0	-99.0	-99.0
DF100 Jin+18	-99.0	-99.0	-99.0
F160 Jin+18	-99.0	-99.0	-99.0
DF160 Jin+18	-99.0	-99.0	-99.0
SFR _{IR} Jin+18	-99.0	-99.0	-99.0
eSFR _{IR} Jin+18	-99.0	-99.0	-99.0
ID JIN+18			
JIN+18 DETECT	false	false	false
flux _{1.4 GHz}	1.37×10^{-4}	1.67×10^{-4}	1.70×10^{-4}
flux _{1.4 GHz} err _{up}	4.6×10^{-5}	5.6×10^{-5}	4.9×10^{-5}
flux _{1.4 GHz} err _{lo}	6.5×10^{-5}	5.3×10^{-5}	4.4×10^{-5}
DETECT _{1.4 GHz}	false	false	true
flux _{3.0 GHz}	9.4×10^{-5}	1.0×10^{-5}	1.0×10^{-5}
flux _{3.0 GHz} err _{up}	3.1×10^{-6}	3.4×10^{-6}	3.5×10^{-6}
flux _{3.0 GHz} err _{lo}	3.1×10^{-6}	3.2×10^{-6}	3.0×10^{-6}
DETECT _{3.0 GHz}	false	false	false
1.4-3.0GHz spectral index	-99.0	-99.0	-3.7
1.4-3.0GHz spectral index_error	-99.0	-99.0	-99.0
S/N _{3.0 GHz}	0.7	-0.6	1.1
S/N _{1.4 GHz}	0.1	1.2	3.8
Schinnerer ID	-99	-99	-99
S _{1.4 GHz} Schinnerer	-99.0	-99.0	-99.0
S _{1.4 GHz} err Schinnerer	-99.0	-99.0	-99.0
Smolcic ID	-99	-99	-99
S _{3 GHz} Smolcic	-99.0	-99.0	-99.0
S _{3 GHz} err Smolcic	-99.0	-99.0	-99.0
SMOLCIC DETECT	false	false	false
SCHINNERER DETECT	false	false	false
RADIO DETECT	false	false	true
RADIO CONTAMINATED	false	false	false
VISUAL CHECK PASS	true	true	true

Table A.4: The results for the stacking analysis of the radio emission of LAEs. We determine the fluxes following the process detailed in Section 4.3.1, using a circular aperture of $5.3''$ and $1.2''$ for the 1.4 GHz and 3 GHz, respectively. In order to make them comparable to Smolčić et al. (2017), we follow Section 4.3.1.4. A stack is considered as having a detection when the $S/N \geq 3$. For stacks with lower S/N , we provide the 3σ upper limit.

Subsample Stacked	# Sources	Redshift (median)	$\log_{10} L$ $L_{\text{Ly}\alpha}$ [erg s $^{-1}$]	$\log_{10} L$ (1.4 GHz) [W Hz $^{-1}$]	SFR (1.4 GHz) [M $_{\odot}$ yr $^{-1}$]	S/N_{14}	$\log_{10} L$ (3.0 GHz) [W Hz $^{-1}$]	SFR (3.0 GHz) [M $_{\odot}$ yr $^{-1}$]	S/N_3
Including radio LAEs									
Full Sample	3696	$3.1^{+1.0}_{-0.6}$	$42.9^{+0.3}_{-0.2}$	$23.59^{+0.08}_{-0.07}$	-	6.7	$23.53^{+0.01}_{-0.01}$	-	50.9
No X-ray LAEs	3442	$3.2^{+1.0}_{-0.6}$	$42.8^{+0.3}_{-0.2}$	<23.5	-	<3	$22.70^{+0.08}_{-0.07}$	-	6.5
2.2<z<2.7	849	$2.5^{+0.0}_{-0.3}$	$42.6^{+0.2}_{-0.1}$	$24.00^{+0.02}_{-0.02}$	-	19.6	$23.81^{+0.01}_{-0.01}$	-	75.6
2.7<z<3.5	2085	$3.2^{+0.2}_{-0.2}$	$42.9^{+0.2}_{-0.1}$	<23.6	-	<3	$23.22^{+0.04}_{-0.03}$	-	16.5
3.5<z<6	762	$4.8^{+0.9}_{-0.7}$	$43.1^{+0.2}_{-0.3}$	<24.0	-	<3	<23.2	-	<3
$42.2 < \log_{10}(L_{\text{Ly}\alpha}) < 43.0$	2654	$3.0^{+0.4}_{-0.5}$	$42.8^{+0.1}_{-0.2}$	$23.51^{+0.08}_{-0.07}$	-	6.8	$23.49^{+0.01}_{-0.01}$	-	43.3
$43.0 < \log_{10}(L_{\text{Ly}\alpha}) < 43.3$	770	$3.3^{+1.5}_{-0.4}$	$43.1^{+0.1}_{-0.1}$	$23.53^{+0.13}_{-0.16}$	-	3.2	$23.34^{+0.04}_{-0.03}$	-	13.4
$43.3 < \log_{10}(L_{\text{Ly}\alpha}) < 43.5$	157	$4.1^{+1.2}_{-1.2}$	$43.4^{+0.1}_{-0.0}$	$24.27^{+0.10}_{-0.07}$	-	6.5	$24.14^{+0.02}_{-0.02}$	-	23.5
$43.5 < \log_{10}(L_{\text{Ly}\alpha}) < 43.8$	82	$3.3^{+2.0}_{-0.4}$	$43.6^{+0.1}_{-0.1}$	$24.16^{+0.32}_{-0.13}$	-	3.8	$23.96^{+0.04}_{-0.03}$	-	16.4
$43.8 < \log_{10}(L_{\text{Ly}\alpha}) < 44.8$	32	$3.1^{+0.2}_{-0.6}$	$43.9^{+0.2}_{-0.1}$	$24.28^{+0.11}_{-0.12}$	-	4.2	$23.95^{+0.04}_{-0.04}$	-	11.4
Excluding radio LAEs									
Full Sample	3576	$3.2^{+1.0}_{-0.6}$	$42.8^{+0.3}_{-0.2}$	<23.4	<84.0	<3	$22.47^{+0.12}_{-0.13}$	$9.3^{+3.0}_{-2.4}$	3.9
2.2<z<2.7	817	$2.5^{+0.0}_{-0.3}$	$42.6^{+0.2}_{-0.1}$	<23.2	<51.6	<3	$22.45^{+0.12}_{-0.14}$	$9.0^{+3.0}_{-2.5}$	3.6
2.2<z<3.5	2013	$3.2^{+0.2}_{-0.2}$	$42.9^{+0.2}_{-0.1}$	<23.5	<110.6	<3	$22.52^{+0.14}_{-0.16}$	$10.6^{+4.1}_{-3.2}$	3.3
3.5<z<6	746	$4.8^{+0.9}_{-0.7}$	$43.1^{+0.2}_{-0.3}$	<24.0	<288.9	<3	<23.1	<43.5	<3
$42.2 < \log_{10}(L_{\text{Ly}\alpha}) < 43.0$	2601	$3.0^{+0.4}_{-0.5}$	$42.8^{+0.1}_{-0.2}$	<23.3	<66.3	<3	<22.4	<8.2	<3
$43.0 < \log_{10}(L_{\text{Ly}\alpha}) < 43.3$	738	$3.3^{+1.5}_{-0.4}$	$43.1^{+0.1}_{-0.1}$	<23.6	<126.2	<3	$22.73^{+0.14}_{-0.17}$	$16.9^{+6.3}_{-5.5}$	3.0
$43.3 < \log_{10}(L_{\text{Ly}\alpha}) < 43.5$	143	$4.6^{+0.7}_{-1.6}$	$43.4^{+0.1}_{-0.0}$	<24.3	<673.6	<3	<23.4	<77.2	<3
$43.5 < \log_{10}(L_{\text{Ly}\alpha}) < 43.8$	68	$4.6^{+1.1}_{-1.6}$	$43.6^{+0.1}_{-0.1}$	<25.0	<3540.2	<3	$23.75^{+0.15}_{-0.12}$	$177.7^{+72.2}_{-41.4}$	4.3
$43.8 < \log_{10}(L_{\text{Ly}\alpha}) < 44.8$	25	$3.2^{+0.2}_{-0.6}$	$43.9^{+0.2}_{-0.1}$	<24.3	<640.5	<3	$23.58^{+0.11}_{-0.14}$	$120.5^{+33.3}_{-33.7}$	3.6

A.1 Public Catalogue of SC4K LAEs and Stacking tables

Table A.5: The results of our stacking analysis of the X-ray emission of LAEs. The redshift was estimated by taking the median and using the 16th and 84th percentiles as the errors. We use this median redshift to determine the luminosity distances used in calculating the x-ray luminosities. The fluxes were estimated using a circular aperture of $7.9''$. We apply further correction factors, as detailed in Section 3.3.1, including an aperture correction. A stack is considered to have a detection if the $S/N \geq 3$ and we provide the 3σ upper-limit in the case of a non-detection.

Subsample Stacked	# Sources	Redshift (median)	$\log_{10} L$ $L_{Ly\alpha}$ [erg s^{-1}]	$\log_{10} F$ 0.5 - 7 keV [$\text{erg s}^{-1} \text{cm}^{-2}$]	$\log_{10} L$ X-rays [erg s^{-1}]	BHAR 0.5 - 7 keV [$M_{\odot} \text{yr}^{-1}$]	S/N 0.5 - 7 keV
Including X-ray LAEs							
Full Sample	3700	$3.1^{+1.0}_{-0.6}$	$42.85^{+0.29}_{-0.17}$	$-15.61^{+0.06}_{-0.07}$	$43.06^{+0.06}_{-0.07}$	$0.041^{+0.006}_{-0.006}$	6.7
X-ray LAEs only	254	$3.0^{+0.4}_{-0.5}$	$43.08^{+0.61}_{-0.31}$	$-14.33^{+0.01}_{-0.01}$	$44.31^{+0.01}_{-0.01}$	$0.720^{+0.015}_{-0.011}$	65.8
2.2 < z < 2.7	849	$2.5^{+0.0}_{-0.3}$	$42.64^{+0.24}_{-0.15}$	$-15.37^{+0.05}_{-0.05}$	$43.12^{+0.05}_{-0.05}$	$0.047^{+0.005}_{-0.005}$	9.1
2.7 < z < 3.5	2085	$3.2^{+0.2}_{-0.2}$	$42.86^{+0.22}_{-0.12}$	$-15.56^{+0.07}_{-0.07}$	$43.12^{+0.07}_{-0.07}$	$0.047^{+0.008}_{-0.007}$	6.4
3.5 < z < 6	766	$4.8^{+0.9}_{-0.7}$	$43.07^{+0.24}_{-0.28}$	< -15.8	< 43.2	< 0.059	< 3
42.2 < $\log_{10}(L_{Ly\alpha})$ < 42.6	384	$2.5^{+0.0}_{-0.3}$	$42.52^{+0.05}_{-0.07}$	< -15.7	< 42.7	< 0.020	< 3
42.6 < $\log_{10}(L_{Ly\alpha})$ < 42.7	323	$2.5^{+0.8}_{-0.0}$	$42.67^{+0.02}_{-0.04}$	< -15.8	< 42.7	< 0.017	< 3
42.7 < $\log_{10}(L_{Ly\alpha})$ < 42.8	762	$3.0^{+0.4}_{-0.5}$	$42.75^{+0.03}_{-0.03}$	< -15.9	< 42.7	< 0.019	< 3
42.8 < $\log_{10}(L_{Ly\alpha})$ < 42.9	686	$3.2^{+0.2}_{-0.3}$	$42.85^{+0.05}_{-0.03}$	< -15.7	< 43.0	< 0.032	< 3
42.9 < $\log_{10}(L_{Ly\alpha})$ < 43.0	500	$3.2^{+1.0}_{-0.3}$	$42.95^{+0.03}_{-0.03}$	$-15.53^{+0.10}_{-0.08}$	$43.15^{+0.10}_{-0.08}$	$0.050^{+0.013}_{-0.009}$	5.7
43.0 < $\log_{10}(L_{Ly\alpha})$ < 43.1	334	$3.2^{+1.0}_{-0.3}$	$43.05^{+0.03}_{-0.03}$	$-15.74^{+0.15}_{-0.15}$	$42.94^{+0.15}_{-0.15}$	$0.031^{+0.013}_{-0.009}$	3.5
43.1 < $\log_{10}(L_{Ly\alpha})$ < 43.2	242	$3.3^{+1.5}_{-0.5}$	$43.15^{+0.04}_{-0.04}$	$-15.38^{+0.06}_{-0.06}$	$43.35^{+0.06}_{-0.06}$	$0.080^{+0.013}_{-0.011}$	7.6
43.2 < $\log_{10}(L_{Ly\alpha})$ < 43.4	302	$4.1^{+0.9}_{-1.2}$	$43.27^{+0.07}_{-0.05}$	$-15.32^{+0.07}_{-0.05}$	$43.59^{+0.07}_{-0.05}$	$0.138^{+0.024}_{-0.015}$	9.2
43.4 < $\log_{10}(L_{Ly\alpha})$ < 43.8	134	$3.5^{+2.1}_{-0.5}$	$43.53^{+0.16}_{-0.09}$	$-14.71^{+0.02}_{-0.02}$	$44.07^{+0.02}_{-0.02}$	$0.416^{+0.022}_{-0.017}$	24.3
43.8 < $\log_{10}(L_{Ly\alpha})$ < 44.8	32	$3.1^{+0.2}_{-0.6}$	$43.94^{+0.20}_{-0.09}$	$-14.22^{+0.01}_{-0.01}$	$44.46^{+0.01}_{-0.01}$	$1.018^{+0.019}_{-0.022}$	47.3
Excluding Civano+16 LAEs							
Full Sample	3600	$3.2^{+1.0}_{-0.6}$	$42.85^{+0.27}_{-0.17}$	< -16.0	< 42.7	< 0.016	< 3
2.2 < z < 2.7	816	$2.5^{+0.0}_{-0.0}$	$42.63^{+0.22}_{-0.14}$	< -15.9	< 42.6	< 0.014	< 3
2.7 < z < 3.5	2021	$3.2^{+0.2}_{-0.2}$	$42.86^{+0.21}_{-0.12}$	< -15.9	< 42.8	< 0.020	< 3
3.5 < z < 6	763	$4.8^{+0.9}_{-0.7}$	$43.07^{+0.24}_{-0.28}$	< -15.8	< 43.3	< 0.064	< 3
42.2 < $\log_{10}(L_{Ly\alpha})$ < 42.6	382	$2.5^{+0.0}_{-0.3}$	$42.51^{+0.05}_{-0.07}$	< -15.8	< 42.7	< 0.019	< 3
42.6 < $\log_{10}(L_{Ly\alpha})$ < 42.7	321	$2.5^{+0.8}_{-0.0}$	$42.67^{+0.02}_{-0.04}$	< -15.8	< 42.7	< 0.017	< 3
42.7 < $\log_{10}(L_{Ly\alpha})$ < 42.8	759	$3.0^{+0.4}_{-0.4}$	$42.75^{+0.03}_{-0.03}$	< -15.9	< 42.7	< 0.019	< 3
42.8 < $\log_{10}(L_{Ly\alpha})$ < 42.9	683	$3.2^{+0.2}_{-0.3}$	$42.85^{+0.05}_{-0.03}$	< -15.7	< 43.0	< 0.033	< 3
42.9 < $\log_{10}(L_{Ly\alpha})$ < 43.0	489	$3.2^{+1.0}_{-0.3}$	$42.95^{+0.03}_{-0.04}$	< -15.7	< 43.0	< 0.033	< 3
43.0 < $\log_{10}(L_{Ly\alpha})$ < 43.1	327	$3.2^{+1.0}_{-0.3}$	$43.05^{+0.03}_{-0.03}$	< -15.7	< 43.0	< 0.034	< 3
43.1 < $\log_{10}(L_{Ly\alpha})$ < 43.2	238	$3.3^{+1.5}_{-0.4}$	$43.15^{+0.04}_{-0.04}$	< -15.8	< 43.0	< 0.033	< 3
43.2 < $\log_{10}(L_{Ly\alpha})$ < 43.4	280	$4.6^{+0.5}_{-1.6}$	$43.27^{+0.07}_{-0.05}$	< -15.7	< 43.3	< 0.075	< 3
43.4 < $\log_{10}(L_{Ly\alpha})$ < 43.8	107	$4.6^{+1.2}_{-1.6}$	$43.51^{+0.12}_{-0.08}$	$-15.43^{+0.11}_{-0.11}$	$43.57^{+0.11}_{-0.11}$	$0.131^{+0.039}_{-0.029}$	4.6
43.8 < $\log_{10}(L_{Ly\alpha})$ < 44.8	13	$3.3^{+1.8}_{-0.2}$	$43.96^{+0.31}_{-0.10}$	$-14.64^{+0.03}_{-0.03}$	$44.09^{+0.03}_{-0.03}$	$0.434^{+0.028}_{-0.032}$	13.5
Excluding X-ray LAEs							
Full Sample	3446	$3.2^{+1.0}_{-0.6}$	$42.85^{+0.27}_{-0.17}$	< -16.0	< 42.7	< 0.017	< 3
2.2 < z < 2.7	787	$2.5^{+0.0}_{-0.0}$	$42.63^{+0.22}_{-0.14}$	< -15.9	< 42.6	< 0.013	< 3
2.2 < z < 3.5	1920	$3.2^{+0.2}_{-0.2}$	$42.86^{+0.20}_{-0.12}$	< -15.9	< 42.8	< 0.021	< 3
3.5 < z < 6	739	$4.8^{+0.9}_{-0.7}$	$43.07^{+0.23}_{-0.28}$	< -15.8	< 43.2	< 0.060	< 3
42.2 < $\log_{10}(L_{Ly\alpha})$ < 42.6	370	$2.5^{+0.0}_{-0.3}$	$42.52^{+0.05}_{-0.07}$	< -15.8	< 42.7	< 0.018	< 3
42.6 < $\log_{10}(L_{Ly\alpha})$ < 42.7	315	$2.5^{+0.8}_{-0.0}$	$42.67^{+0.02}_{-0.04}$	< -15.9	< 42.6	< 0.015	< 3
42.7 < $\log_{10}(L_{Ly\alpha})$ < 42.8	734	$3.0^{+0.4}_{-0.4}$	$42.75^{+0.03}_{-0.03}$	< -15.9	< 42.7	< 0.020	< 3
42.8 < $\log_{10}(L_{Ly\alpha})$ < 42.9	656	$3.2^{+0.2}_{-0.3}$	$42.85^{+0.03}_{-0.03}$	< -15.7	< 43.0	< 0.032	< 3
42.9 < $\log_{10}(L_{Ly\alpha})$ < 43.0	470	$3.2^{+1.0}_{-0.3}$	$42.95^{+0.03}_{-0.04}$	< -15.7	< 43.0	< 0.033	< 3
43.0 < $\log_{10}(L_{Ly\alpha})$ < 43.1	312	$3.2^{+1.0}_{-0.3}$	$43.05^{+0.03}_{-0.03}$	< -15.8	< 42.9	< 0.029	< 3
43.1 < $\log_{10}(L_{Ly\alpha})$ < 43.2	223	$3.3^{+1.6}_{-0.4}$	$43.15^{+0.04}_{-0.04}$	< -15.8	< 43.0	< 0.032	< 3
43.2 < $\log_{10}(L_{Ly\alpha})$ < 43.4	268	$4.6^{+0.5}_{-1.6}$	$43.27^{+0.07}_{-0.05}$	< -15.7	< 43.3	< 0.076	< 3
43.4 < $\log_{10}(L_{Ly\alpha})$ < 43.8	91	$4.8^{+1.0}_{-1.9}$	$43.51^{+0.10}_{-0.08}$	< -15.5	< 43.5	< 0.123	< 3
43.8 < $\log_{10}(L_{Ly\alpha})$ < 44.8	6	$3.2^{+2.0}_{-0.4}$	$43.88^{+0.14}_{-0.03}$	$-15.22^{+0.15}_{-0.22}$	$43.48^{+0.15}_{-0.22}$	< 0.109	2.1

References

- Abel T., Bryan G. L., Norman M. L., 2000, *ApJ*, 540, 39
- Aird J., Nandra K., et al., 2010, *MNRAS*, 401, 2531
- Alexander D. M., et al., 2003, *AJ*, 125, 383
- Alexander D. M., et al., 2008, *AJ*, 135, 1968
- Alexander D. M., et al., 2011, *ApJ*, 738, 44
- Antonucci R., 1993, *Annual Review of Astron and Astrophys*, 31, 473
- Athreya R. M., Kapahi V. K., 1998, *Journal of Astrophysics and Astronomy*, 19, 63
- Azadi M., et al., 2015, *ApJ*, 806, 187
- Bañados E., et al., 2018, *Nature*, 553, 473
- Bacon R., et al., 2015, *A&A*, 575, A75
- Barber C., Schaye J., Bower R. G., Crain R. A., Schaller M., Theuns T., 2016, *MNRAS*, 460, 1147
- Barnes J. E., 2004, *MNRAS*, 350, 798
- Begelman M. C., Volonteri M., Rees M. J., 2006, *MNRAS*, 370, 289
- Benson A. J., Bower R. G., Frenk C. S., Lacey C. G., Baugh C. M., Cole S., 2003, *ApJ*, 599, 38

- Best P. N., Kauffmann G., Heckman T. M., Brinchmann J., Charlot S., Ivezić Ž., White S. D. M., 2005, MNRAS, 362, 25
- Best P. N., Kaiser C. R., Heckman T. M., Kauffmann G., 2006, MNRAS, 368, L67
- Best P., et al., 2013, ASSP, 37, 235
- Bolton J. G., Stanley G. J., Slee O. B., 1949, Nature, 164, 101
- Bondi M., Ciliegi P., Schinnerer E., Smolčić V., Jahnke K., Carilli C., Zamorani G., 2008, ApJ, 681, 1129
- Booth C. M., Schaye J., 2009, MNRAS, 398, 53
- Booth C. M., Schaye J., 2011, MNRAS, 413, 1158
- Bower R. G., Benson A. J., Malbon R., Helly J. C., Frenk C. S., Baugh C. M., Cole S., Lacey C. G., 2006, MNRAS, 370, 645
- Bower R. G., Schaye J., Frenk C. S., Theuns T., Schaller M., Crain R. A., McAlpine S., 2017, MNRAS, 465, 32
- Brandt W. N., Alexander D. M., 2015, A&AR, 23, 1
- Bromm V., Loeb A., 2006, ApJ, 642, 382
- Bunker A. J., Warren S. J., Hewett P. C., Clements D. L., 1995, MNRAS, 273, 513
- Burbidge G. R., 1956, ApJ, 124, 416
- Calhau J., Sobral D., Stroe A., Best P., Smail I., Lehmer B., Harrison C., Thomson A., 2017, MNRAS, 464, 303
- Calistro Rivera G., et al., 2017, MNRAS, 469, 3468
- Capak P., et al., 2007, ApJS, 172, 99
- Casali M., Adamson A., Alves de Oliveira C., et al., 2007, A&A, 467, 777

-
- Chabrier G., 2003, *Public. of the Astron. Soc. Pac.*, 115, 763
- Chapman S. C., Blain A. W., Smail I., Ivison R. J., 2005, *ApJ*, 622, 772
- Chen C.-T. J., et al., 2013, *ApJ*, 773, 3
- Christensen L., Jahnke K., Wisotzki L., Sánchez S. F., 2006, *A&A*, 459, 717
- Civano F., et al., 2016, *ApJ*, 819, 62
- Compton A. H., 1923, *Phys. Rev.*, 21, 483
- Conselice C. J., 2014, *Annual Review of Astron and Astrophys*, 52, 291
- Cowie L. L., Hu E. M., 1998, *AJ*, 115, 1319
- Cowie L. L., Barger A. J., Hu E. M., 2010, *ApJ*, 711, 928
- Davies R. I., Maciejewski W., Hicks E. K. S., Tacconi L. J., Genzel R., Engel H., 2009, *ApJ*, 702, 114
- Delhaize J., et al., 2017, *A&A*, 602, A4
- Delvecchio I., Gruppioni C., et al., 2014, *MNRAS*, 439, 2736
- Delvecchio I., Lutz D., Berta S., et al., 2015, *MNRAS*, 449, 373
- Devecchi B., Volonteri M., 2009, *ApJ*, 694, 302
- Di Matteo T., Springel V., Hernquist L., 2005, *Nature*, 433, 604
- Dittenber B., Oey M. S., Hodges-Kluck E., Gallo E., Hayes M., Östlin G., Melinder J., 2020, *ApJL*, 890, L12
- Dressler A., Richstone D. O., 1988, *ApJ*, 324, 701
- Dunn J. P., et al., 2010, *ApJ*, 709, 611
- Elder F. R., Gurewitsch A. M., Langmuir R. V., Pollock H. C., 1947, *Physical Review*, 71, 829
- Elvis M., Civano F., Vignali C., et al., 2009, *ApJS*, 184, 158

-
- Erb D. K., Pettini M., Steidel C. C., Strom A. L., Rudie G. C., Trainor R. F., Shapley A. E., Reddy N. A., 2016, *ApJ*, 830, 52
- Event Horizon Telescope Collaboration et al., 2019, *ApJL*, 875, L1
- Fabbiano G., 1989, *Annual Review of Astron and Astrophys*, 27, 87
- Ferrarese L., Merritt D., 2000, *ApJL*, 539, L9
- Ferré-Mateu A., Mezcua M., Trujillo I., Balcells M., van den Bosch R. C. E., 2015, *ApJ*, 808, 79
- Franck J. R., McGaugh S. S., 2016, *ApJ*, 833, 15
- Fryer C. L., Woosley S. E., Heger A., 2001, *ApJ*, 550, 372
- Fukugita M., Hogan C. J., Peebles P. J. E., 1998, *ApJ*, 503, 518
- Ganguly R., Brotherton M. S., 2008, *ApJ*, 672, 102
- Garn T., et al., 2010, *MNRAS*, 402, 2017
- Gawiser E., et al., 2006, *ApJL*, 642, L13
- Geach J. E., Smail I., Best P. N., Kurk J., Casali M., Ivison R. J., Coppin K., 2008, *MNRAS*, 388, 1473
- Geach J. E., et al., 2013, *MNRAS*, 432, 53
- Geach J. E., et al., 2014, *Nature*, 516, 68
- Genel S., et al., 2014, *MNRAS*, 445, 175
- Georgakakis A., et al., 2015, *MNRAS*, 453, 1946
- Greisen E. W., 2003, in Heck A., ed., *Astrophysics and Space Science Library* Vol. 285, *Information Handling in Astronomy - Historical Vistas*. p. 109, doi:10.1007/0-306-48080-8_7
- Griffin M. J., et al., 2010, *A&A*, 518, L3

-
- Gurzadian V. G., Ozernoi L. M., 1979, *Nature*, 280, 214
- Haardt F., Maraschi L., 1991, *ApJL*, 380, L51
- Harrison C. M., et al., 2012, *ApJL*, 760, L15
- Hasinger G., 2008, *A&A*, 490, 905
- Heckman T. M., Best P. N., 2014, *Annual Review of Astron and Astrophys*, 52, 589
- Heckman T. M., Kauffmann G., Brinchmann J., Charlot S., Tremonti C., White S. D. M., 2004, *ApJ*, 613, 109
- Heinis S., et al., 2013, *MNRAS*, 429, 1113
- Hickox R. C., Alexander D. M., 2018, *Annual Review of Astron and Astrophys*, 56, 625
- Hildebrandt H., et al., 2017, *MNRAS*, 465, 1454
- Holt J., Tadhunter C. N., Morganti R., 2008, *MNRAS*, 387, 639
- Hopkins A. M., Beacom J. F., 2006, *ApJ*, 651, 142
- Hopkins A. M., et al., 2003, *ApJ*, 599, 971
- Hopkins P. F., Hernquist L., Cox T. J., Di Matteo T., Martini P., Robertson B., Springel V., 2005, *ApJ*, 630, 705
- Hopkins P. F., Lidz A., Hernquist L., Coil A. L., Myers A. D., Cox T. J., Spergel D. N., 2007, *ApJ*, 662, 110
- Hu E. M., Songaila A., Cowie L. L., Stockton A., 1991, *ApJ*, 368, 28
- Ibar E., et al., 2013, *MNRAS*, 434, 3218
- Jin S., et al., 2018, *ApJ*, 864, 56
- Karim A., et al., 2011, *ApJ*, 730, 61

- Karman W., et al., 2015, *A&A*, 574, A11
- Kennicutt Jr. R. C., 1998, *ARA&A*, 36, 189
- Khostovan A. A., Sobral D., Mobasher B., Best P. N., Smail I., Stott J. P., Hemmati S., Nayyeri H., 2015, *MNRAS*, 452, 3948
- Khostovan A. A., et al., 2019, *MNRAS*, 489, 555
- Kim J.-H., Wise J., Abel T., 2009, in *APS April Meeting Abstracts*. p. G8.009
- Klamer I. J., Ekers R. D., Bryant J. J., Hunstead R. W., Sadler E. M., De Breuck C., 2006, *MNRAS*, 371, 852
- Klein U., Emerson D. T., 1981, *A&A*, 94, 29
- Konno A., Ouchi M., Nakajima K., Duval F., Kusakabe H., Ono Y., Shimasaku K., 2016, *ApJ*, 823, 20
- Kormendy J., 1993, in Beckman J., Colina L., Netzer H., eds, *The Nearest Active Galaxies*. pp 197–218
- Kormendy J., Ho L. C., 2013, *Annual Review of Astron and Astrophys*, 51, 511
- Krishna G., Sirothia S. K., Mhaskey M., Ranadive P., Wiita P. J., Goyal A., Kantharia N. G., Ishwara-Chandra C. H., 2014, *MNRAS*, 443, 2824
- Kubo M., et al., 2013, *ApJ*, 778, 170
- Lacki B. C., Thompson T. A., Quataert E., 2010, *ApJ*, 717, 1
- Larson R. B., 1999, in Nakamoto T., ed., *Star Formation 1999*. pp 336–340 ([arXiv:astro-ph/9908189](https://arxiv.org/abs/astro-ph/9908189))
- Lawrence A., Elvis M., 1982, *ApJ*, 256, 410
- Lehmer B. D., et al., 2007, *ApJ*, 657, 681
- Lehmer B. D., et al., 2013, *ApJ*, 765, 87
- Lehmer B. D., et al., 2016, *ApJ*, 825, 7

-
- Lilly S. J., Le Fevre O., Hammer F., Crampton D., 1996, *ApJL*, 460, L1
- Loeb A., Rasio F. A., 1994, *ApJ*, 432, 52
- Luo B., et al., 2011, *ApJ*, 740, 37
- Lusso E., et al., 2013, *ApJ*, 777, 86
- Lutz D., et al., 2010, *ApJ*, 712, 1287
- Lutz D., et al., 2011, *A&A*, 532, A90
- Madau P., Dickinson M., 2014, *ARA&A*, 52, 415
- Madau P., Rees M. J., 2001, *ApJL*, 551, L27
- Magorrian J., et al., 1998, *AJ*, 115, 2285
- Marchesi S., et al., 2016a, *ApJ*, 817, 34
- Marchesi S., et al., 2016b, *ApJ*, 827, 150
- Marconi A., Risaliti G., Gilli R., Hunt L. K., Maiolino R., Salvati M., 2004, *MNRAS*, 351, 169
- Markevitch M., et al., 2003, *The Astrophysical Journal*, 583, 70
- Matsuda Y., et al., 2004, *AJ*, 128, 569
- Matthee J. J. A., et al., 2014, *Monthly Notices of the Royal Astronomical Society*, 440, 2375
- Matthee J., Sobral D., Oteo I., Best P., Smail I., Röttgering H., Paulino-Afonso A., 2016, *MNRAS*, 458, 449
- Matthee J., Sobral D., Best P., Smail I., Bian F., Darvish B., Röttgering H., Fan X., 2017a, *MNRAS*, 471, 629
- Matthee J., Sobral D., Darvish B., Santos S., Mobasher B., Paulino-Afonso A., Röttgering H., Alegre L., 2017b, *MNRAS*, 472, 772

-
- Matthee J., et al., 2017c, *ApJ*, 851, 145
- Matthee J., et al., 2019, *ApJ*, 881, 124
- McAlpine S., Bower R. G., Harrison C. M., Crain R. A., Schaller M., Schaye J., Theuns T., 2017, *MNRAS*, 468, 3395
- McNamara B. R., Nulsen P. E. J., 2007, *Annual Review of Astron and Astrophys*, 45, 117
- McNamara B. R., Kazemzadeh F., Rafferty D. A., Birzan L., Nulsen P. E. J., Kirkpatrick C. C., Wise M. W., 2009, *ApJ*, 698, 594
- McNamara B. R., Rohanizadegan M., Nulsen P. E. J., 2011, *ApJ*, 727, 39
- Merloni A., et al., 2014, *MNRAS*, 437, 3550
- Merritt D., Milosavljević M., 2005, *Living Reviews in Relativity*, 8
- Meurs E. J. A., Wilson A. S., 1984, *A&A*, 136, 206
- Mezcua M., 2017, *International Journal of Modern Physics D*, 26, 1730021
- Mezcua M., Civano F., Marchesi S., Suh H., Fabbiano G., Volonteri M., 2018, *MNRAS*, 478, 2576
- Miley G., De Breuck C., 2008, *A&AR*, 15, 67
- Morganti R., Tadhunter C. N., Oosterloo T. A., 2005, *A&A*, 444, L9
- Mortlock D. J., Patel M., Warren S. J., Hewett P. C., Venemans B. P., McMahon R. G., Simpson C., 2012, *MNRAS*, 419, 390
- Mullaney J. R., et al., 2012a, *MNRAS*, 419, 95
- Mullaney J. R., et al., 2012b, *ApJL*, 753, L30
- Nakajima K., Ellis R. S., Iwata I., Inoue A. K., Kusakabe H., Ouchi M., Robertson B. E., 2016, *ApJL*, 831, L9

-
- Nakamura F., Umemura M., 2000, in Weiss A., Abel T. G., Hill V., eds, *The First Stars*. p. 263, doi:10.1007/10719504_48
- Nesvadba N. P. H., Lehnert M. D., Eisenhauer F., Gilbert A., Tecza M., Abuter R., 2006, *ApJ*, 650, 693
- Nesvadba N. P. H., Lehnert M. D., De Breuck C., Gilbert A., van Breugel W., 2007, *A&A*, 475, 145
- Nesvadba N. P. H., Lehnert M. D., De Breuck C., Gilbert A. M., van Breugel W., 2008, *A&A*, 491, 407
- Netzer H., et al., 2007, *ApJ*, 666, 806
- Oliver S. J., Bock J., Altieri B., et al., 2012, *MNRAS*, 424, 1614
- Ono Y., et al., 2012, *ApJ*, 744, 83
- Ostriker J. P., Gnedin N. Y., 1996, *ApJL*, 472, L63
- Oteo I., et al., 2012a, *A&A*, 541, A65
- Oteo I., et al., 2012b, *ApJ*, 751, 139
- Oteo I., Sobral D., Ivison R. J., Smail I., Best P. N., Cepa J., Pérez-García A. M., 2015, *MNRAS*, 452, 2018
- Ouchi M., et al., 2008, *ApJS*, 176, 301
- Overzier R. A., 2016, *A&AR*, 24, 14
- Page M. J., et al., 2012, *Nature*, 485, 213
- Park T., Kashyap V. L., Siemiginowska A., van Dyk D. A., Zezas A., Heinke C., Wargelin B. J., 2006, *ApJ*, 652, 610
- Paulino-Afonso A., et al., 2018, *MNRAS*, 476, 5479
- Pirzkal N., Malhotra S., Rhoads J. E., Xu C., 2007, *ApJ*, 667, 49
- Planck Collaboration et al., 2018, arXiv e-prints, p. arXiv:1807.06209

-
- Pritchett C. J., 1994, *Public. of the Astron. Soc. Pac.*, 106, 1052
- Puccetti S., Vignali C., Cappelluti N., et al., 2009, *ApJS*, 185, 586
- Rafferty D. A., Brandt W. N., Alexander D. M., et al., 2011, *ApJ*, 742, 3
- Ranalli P., Comastri A., Setti G., 2003, *A&A*, 399, 39
- Rees M. J., 1967, *MNRAS*, 136, 279
- Rodighiero G., et al., 2015, *ApJL*, 800, L10
- Rosas-Guevara Y., Bower R. G., Schaye J., McAlpine S., Dalla Vecchia C., Frenk C. S., Schaller M., Theuns T., 2016, *MNRAS*, 462, 190
- Rowan-Robinson M., 1995, *MNRAS*, 272, 737
- Sadler E. M., et al., 2002, *MNRAS*, 329, 227
- Salim S., et al., 2009, *ApJ*, 700, 161
- Salpeter E. E., 1964, *ApJ*, 140, 796
- Sandberg A., Guaita L., Östlin G., Hayes M., Kiaeerad F., 2015, *A&A*, 580, A91
- Santos S., et al., 2020, *MNRAS*, 493, 141
- Schawinski K., Thomas D., Sarzi M., Maraston C., Kaviraj S., Joo S.-J., Yi S. K., Silk J., 2007, *MNRAS*, 382, 1415
- Schaye J., Crain R. A., Bower R. G., et al., 2015, *MNRAS*, 446, 521
- Schinnerer E., et al., 2004, *AJ*, 128, 1974
- Schinnerer E., et al., 2007, *ApJS*, 172, 46
- Schinnerer E., et al., 2010, *ApJS*, 188, 384
- Schmitt H. R., Calzetti D., Armus L., Giavalisco M., Heckman T. M., Kennicutt Jr. R. C., Leitherer C., Meurer G. R., 2006, *ApJ*, 643, 173

-
- Schnorr Müller A., Storch-Bergmann T., Riffel R. A., Ferrari F., Steiner J. E., Axon D. J., Robinson A., 2011, MNRAS, 413, 149
- Schweitzer M., et al., 2006, ApJ, 649, 79
- Schweizer F., 2009, Globular Cluster Formation in Mergers. p. 331, doi:10.1007/978-3-540-76961-3_78
- Scoville N., Aussel H., Brusa M., et al., 2007, ApJS, 172, 1
- Seyfert C. K., 1943, ApJ, 97, 28
- Seymour N., et al., 2008, MNRAS, 386, 1695
- Shankar F., Weinberg D. H., Miralda-Escudé J., 2009, ApJ, 690, 20
- Shibuya T., Ouchi M., Harikane Y., Nakajima K., 2019, ApJ, 871, 164
- Shields G. A., 1999, Public. of the Astron. Soc. Pac., 111, 661
- Shim H., Chary R.-R., Dickinson M., Lin L., Spinrad H., Stern D., Yan C.-H., 2011, ApJ, 738, 69
- Silk J., Rees M. J., 1998, A&A, 331, L1
- Silverman J. D., Green P. J., et al., 2008, The Astrophysical Journal, 679, 118
- Smolčić V., et al., 2017, A&A, 602, A1
- Smolčić V., et al., 2009, ApJ, 690, 610
- Sobral D., Matthee J., 2019, A&A, 623, A157
- Sobral D., et al., 2009a, MNRAS, 398, 75
- Sobral D., et al., 2009b, MNRAS, 398, L68
- Sobral D., Best P. N., Matsuda Y., Smail I., Geach J. E., Cirasuolo M., 2012, MNRAS, 420, 1926

- Sobral D., Smail I., Best P. N., Geach J. E., Matsuda Y., Stott J. P., Cirasuolo M., Kurk J., 2013, MNRAS, 428, 1128
- Sobral D., Best P. N., Smail I., Mobasher B., Stott J., Nisbet D., 2014, MNRAS, 437, 3516
- Sobral D., Matthee J., Darvish B., Schaerer D., Mobasher B., Röttgering H. J. A., Santos S., Hemmati S., 2015, ApJ, 808, 139
- Sobral D., Kohn S. A., Best P. N., Smail I., Harrison C. M., Stott J., Calhau J., Matthee J., 2016, MNRAS, 457, 1739
- Sobral D., et al., 2017, MNRAS, 466, 1242
- Sobral D., Santos S., Matthee J., Paulino-Afonso A., Ribeiro B., Calhau J., Khostovan A. A., 2018a, MNRAS, 476, 4725
- Sobral D., et al., 2018b, MNRAS, 477, 2817
- Sobral D., et al., 2019, MNRAS, 482, 2422
- Soltan A., 1982, MNRAS, 200, 115
- Somerville R. S., Davé R., 2015, Annual Review of Astron and Astrophys, 53, 51
- Stanley F., Harrison C. M., Alexander D. M., Swinbank A. M., Aird J. A., Del Moro A., Hickox R. C., Mullaney J. R., 2015, MNRAS, 453, 591
- Stark C. W., Font-Ribera A., White M., Lee K.-G., 2015, MNRAS, 453, 4311
- Storchi-Bergmann T., Lopes R. D. S., McGregor P. J., Riffel R. A., Beck T., Martini P., 2010, MNRAS, 402, 819
- Stroe A., van Weeren R. J., Intema H. T., Röttgering H. J. A., Brüggem M., Hoeft M., 2013, A&A, 555, A110
- Stroe A., Sobral D., Matthee J., Calhau J., Oteo I., 2017, MNRAS, 471, 2558
- Swinbank A. M., Sobral D., Smail I., Geach J. E., Best P. N., McCarthy I. G., Crain R. A., Theuns T., 2012, MNRAS, 426, 935

-
- Targett T. A., Dunlop J. S., McLure R. J., 2012, *MNRAS*, 420, 3621
- Thomson A. P., et al., 2014, *MNRAS*, 442, 577
- Thomson A., et al., 2016, *ApJ*, submitted,
- Trainor R. F., Strom A. L., Steidel C. C., Rudie G. C., 2016, *ApJ*, 832, 171
- Tremonti C. A., Moustakas J., Diamond-Stanic A. M., 2007, *ApJL*, 663, L77
- Urry C. M., Padovani P., 1995, *Public. of the Astron. Soc. Pac.*, 107, 803
- Vasudevan R. V., Fabian A. C., 2007, *MNRAS*, 381, 1235
- Veilleux S., Cecil G., Bland-Hawthorn J., 2005, *Annual Review of Astron and Astrophys*, 43, 769
- Venemans B. P., et al., 2007, *A&A*, 461, 823
- Villar-Martín M., Vernet J., di Serego Alighieri S., Fosbury R., Pentericci L., Cohen M., Goodrich R., Humphrey A., 2002, *MNRAS*, 336, 436
- Vito F., Gilli R., Vignali C., Comastri A., Brusa M., Cappelluti N., Iwasawa K., 2014, *MNRAS*, 445, 3557
- Vito F., et al., 2016, *MNRAS*, 463, 348
- Volonteri M., 2012, *Science*, 337, 544
- Wang J. X., et al., 2004a, *ApJL*, 608, L21
- Wang J. X., Malhotra S., Rhoads J. E., Norman C. A., 2004b, *ApJL*, 612, L109
- Weidinger M., Møller P., Fynbo J. P. U., 2004, *Nature*, 430, 999
- Weinberger R., et al., 2018, *MNRAS*, 479, 4056
- White S. D. M., Frenk C. S., 1991, *ApJ*, 379, 52
- White S. D. M., Rees M. J., 1978, *MNRAS*, 183, 341
- Wilman R. J., Johnstone R. M., Crawford C. S., 2000, *MNRAS*, 317, 9

- Wold I. G. B., Barger A. J., Cowie L. L., 2014, *ApJ*, 783, 119
- Wold I. G. B., Finkelstein S. L., Barger A. J., Cowie L. L., Rosenwasser B., 2017, *ApJ*, 848, 108
- Yamada T., Nakamura Y., Matsuda Y., Hayashino T., Yamauchi R., Morimoto N., Kousai K., Umemura M., 2012, *AJ*, 143, 79
- Young S., Axon D. J., Robinson A., Hough J. H., Smith J. E., 2007, *Nature*, 450, 74
- Yun M. S., Reddy N. A., Condon J. J., 2001, *ApJ*, 554, 803
- da Cunha E., Charlot S., Elbaz D., 2008, *MNRAS*, 388, 1595